

Copyright © 1991, by the author(s).
All rights reserved.

Permission to make digital or hard copies of all or part of this work for personal or classroom use is granted without fee provided that copies are not made or distributed for profit or commercial advantage and that copies bear this notice and the full citation on the first page. To copy otherwise, to republish, to post on servers or to redistribute to lists, requires prior specific permission.

**MONOLITHIC MICROWAVE OSCILLATORS
AND AMPLIFIERS**

by

Nhat Minh Nguyen

Memorandum No. UCB/ERL M91/36

22 April 1991

**MONOLITHIC MICROWAVE OSCILLATORS
AND AMPLIFIERS**

Copyright © 1991

by

Nhat Minh Nguyen

Memorandum No. UCB/ERL M91/36

22 April 1991

ELECTRONICS RESEARCH LABORATORY

College of Engineering
University of California, Berkeley
94720

TITLE PAGE

Acknowledgements

I wish to express my sincere gratitude to my research advisor, Professor Robert Meyer, for his guidance, enthusiasm, and encouragement throughout this Ph.D. dissertation work. I am also grateful to Professor Donald Pederson for his invaluable advice on research matters. I would like to thank the members of my Ph.D. qualifying committee, Professors Donald Pederson, Robert Meyer, Paul Gray, and Charles Stone for their time.

The design, implementation, and testing of the circuits would not have been possible without the generous contributions of a number of corporations and the dedication of their staff members. I am very grateful to William Mack and Signetics Corporation for circuit fabrications and for much assistance in the layout and characterization of the prototype inductors, amplifiers, and oscillators; to Issy Kipnis and the Advanced Bipolar Products division of AvanteK for the use of their microwave laboratory; to Tektronix Inc. for the *TekSpice* circuit simulator; and to MicroSim Corporation for the *PSpice* circuit simulator. This research was also supported in part by the U.S. Army Research Office under grant DAAL03-87-K0079 and by a grant from IBM Corporation.

I like to thank Chris Hull for fruitful discussions and Cynthia Keys for proofreading parts of this dissertation. Fellow graduate students, Greg Uehara, Peter Kennedy, Cormac Conroy, and Paul Krueger have provided me with their warm and “non-oscillating” friendship for which I will always cherish.

I appreciate the support and spiritual direction given by Fr. Joe, Fr. Salvatore, Mark Gibson, Alonso Mencos, and Emilio Chuvieco. I would like to thank my dear friends, Nguyễn Minh Tâm, Trần Thanh Lịch, and Trần Giao Uyên for many fun-filled evenings in Oakland and Concord. I am especially grateful to Hoàng Quỳnh Anh for her unfailing concern and encouragement, and to Nguyễn Xuân Đào for her caring support and all the memories.

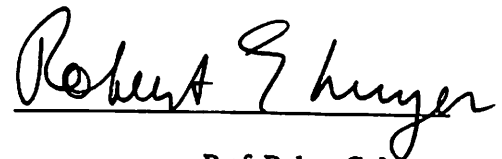
And finally, to my beloved parents, brothers, sisters, and nieces: *this dissertation is dedicated to you!* Your love and encouragement have given me the courage to persevere in difficult times. Your caring support through the years has brought me much happiness. For these and many more, I am forever grateful.

Monolithic Microwave Oscillators and Amplifiers

Ph.D.

Nhat Minh Nguyen

Department of EECS



Prof. Robert G. Meyer

Thesis Chairman

Abstract

This dissertation explores a systematic design methodology for microwave LC sinusoidal oscillators. The objective is to realize oscillators that achieve reliable oscillation build-up and have a single predictable frequency of oscillation in the steady state. This dissertation also explores novel sinusoidal VCO (voltage-controlled oscillator) configurations, and investigates the application of inductors in the design of silicon bipolar monolithic RF amplifiers.

A key problem in the implementation of monolithic microwave LC oscillators is the realization of integrated inductors. Through use of a silicon bipolar IC process featuring oxide isolation and multilayer metal options, practical inductors at microwave frequencies have been fabricated and fully characterized. Inductor Q factors from 3 to 10 and inductors up to 10 nH in the GHz range were achieved.

Presently available sinusoidal VCOs often require external varactors (voltage-controlled capacitors) and inductors for frequency tuning and are not suitable for monolithic integration. A novel sinusoidal VCO circuit has been realized that achieves a simulated tuning range of 300 MHz, extending from 1.5 GHz to 1.8 GHz. This circuit does not require a varactor for frequency tuning but, instead, relies on characteristics inherent in the circuit configuration. Simulation results also indicate that this circuit is insensitive to process tolerances and temperature variations.

Inductors are used to boost circuit gain and to improve matching and noise performance in RF amplifiers. A bipolar monolithic bandpass amplifier has been fabricated and characterized. It achieves a peak S_{21} gain of 8 dB, a simulated noise figure of 6.4 dB, and a matched input impedance of 50 Ω in the frequency range 1 to 2 GHz.

Table of Contents

Abstract	i
Acknowledgements	ii
Table of Contents	iii
CHAPTER 1 - INTRODUCTION	
1.1 Motivation	1
1.2 Thesis Organization	3
CHAPTER 2 - OSCILLATOR CHARACTERISTICS AND MODELS	
2.1 Oscillator Characteristics	4
2.2 Oscillator Models	4
2.3 Natural Frequencies	7
2.4 Summary	10
CHAPTER 3 - OSCILLATOR ANALYSES	
3.1 Introduction	11
3.2 Small-Signal Analysis	11
3.2.1 Feedback Oscillators	11
3.2.2 Negative-Resistance Oscillators	14
3.2.3 Multi-Oscillation	17
3.2.4 Predicting Oscillation Frequency from the Start-Up Conditions	21
3.3 Large-Signal Analysis	27
3.4 Stability Analyses	28
3.4.1 Frequency-Stability Analysis	29
3.4.2 Amplitude-Stability Analysis	30
3.5 Summary	31
CHAPTER 4 - OSCILLATOR DESIGN METHODOLOGY	
4.1 Introduction	32
4.2 Systematic Design Methodology	32
4.2.1 Voltage/Current-Controlled Negative Resistors	33
4.2.2 LC-Dependent Negative Resistors	41
4.3 Implementation	48
4.4 Summary	50
CHAPTER 5 - SILICON INTEGRATED INDUCTORS	
5.1 Introduction	52
5.2 Inductor Structure and Characterization	52
5.3 Implementations	59
5.4 Conclusion	64

CHAPTER 6 - MONOLITHIC LC VCOs	
6.1 Introduction	66
6.2 Circuit Configuration	67
6.2.1 Oscillation Frequency	68
6.2.2 Frequency Variation	72
6.3 Loop-Gain Derivation and Root Loci	74
6.4 Circuit Implementation and Performance	80
6.5 Conclusion	83
CHAPTER 7 - Si BIPOLAR MONOLITHIC RF BANDPASS AMPLIFIERS	
7.1 Introduction	85
7.2 Design Approach	85
7.3 Circuit Configuration and Implementation	89
7.4 Noise-Figure Derivation	94
7.5 Conclusion	99
CHAPTER 8 - CONCLUSIONS AND FUTURE DIRECTIONS	100
APPENDICES	
A. Indefinite Admittance Matrix	102
B. Lossless Transmission Line Modeling	105
C. Software Characterization of the Spiral Inductor and Microstrip Line	108
References	120

Chapter 1 - Introduction

1.1. Motivation

Recent advances in silicon bipolar IC technology have sparked interest in developing multifunction silicon MMICs (monolithic microwave integrated circuits) for communication systems. In particular, various research and advanced developments are presently directed toward demonstrating silicon integration of the RF receiver system shown Fig. 1.1. This system finds wide application from mobile radio to microwave satellite reception such as the global positioning satellite (GPS) and the direct broadcast satellite (DBS). Due to the system complexity and the high-frequency requirement, it is necessary to obtain firm knowledge on the performance and limitations of the circuit components of which the system is composed. Also, the optimized performance of silicon technology is to be exploited because it provides the lowest-cost solution, and thus will have the widest impact on practical systems. This dissertation is concerned with the design and fabrication of the voltage-controlled oscillator (VCO) circuits and the RF amplifiers which are to be used in monolithic microwave (> 1 GHz) RF receivers.

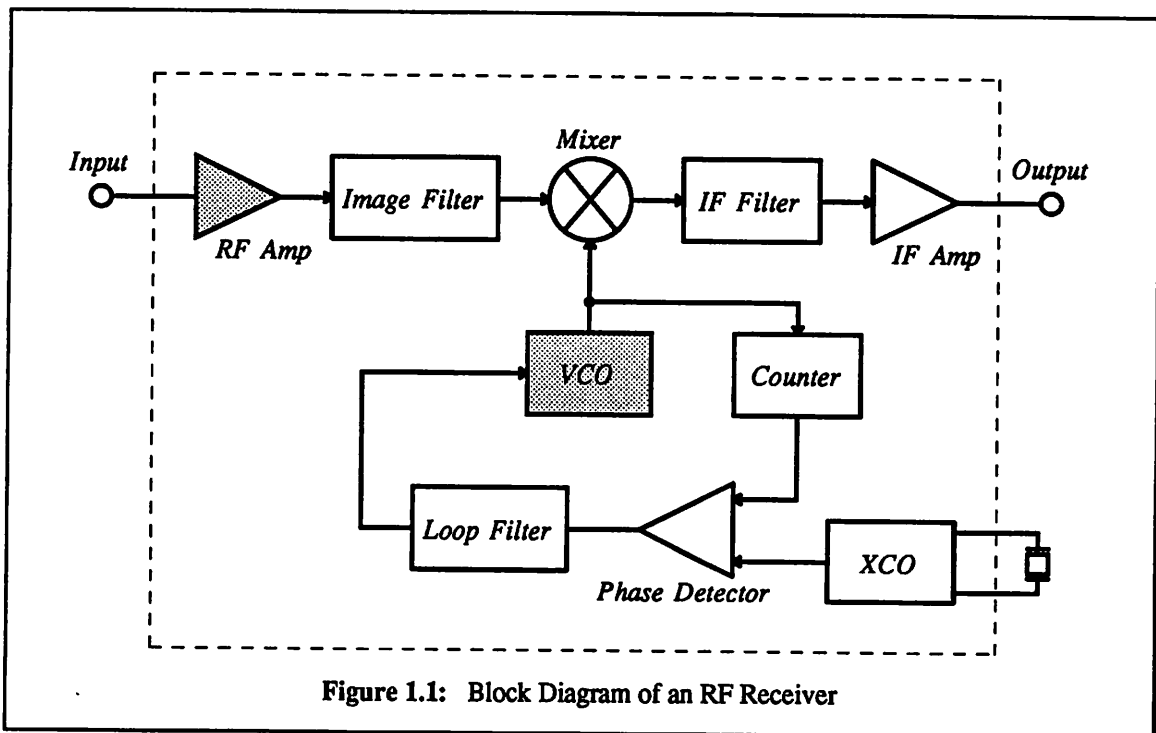


Figure 1.1: Block Diagram of an RF Receiver

As frequencies of interest enter the microwave region, parasitic device elements in an oscillator circuit introduce significant excess phase shift and hence modify the oscillation frequency. It is shown in Chapter 3 that conventional oscillator design techniques may not be applicable in the design of microwave oscillator circuits. With regard to the initial (linear) response of an oscillator, the so-called start-up conditions have been widely used for predicting the existence of an oscillatory behavior in the circuit. However, these conditions are not always valid and can provide misleading results. It is, therefore, important to understand the limitations of these conditions and to introduce additional analysis techniques. Conventional design techniques are also insufficient for analyzing the *multi-oscillation* phenomenon in which two or more oscillations are simultaneously present in the steady state. This dissertation explores a systematic design methodology for microwave LC sinusoidal oscillators that achieve reliable oscillation build-up and have a single predictable frequency of oscillation in the steady state. While silicon bipolar technology is of primary interest in this dissertation, the design methodology is equally applicable in other technologies.

Depending on the shape of the oscillator output waveform, we can classify oscillator circuits in two groups: *relaxation* oscillators and *sinusoidal* oscillators. Most presently available voltage-controlled oscillators in monolithic IC technology are relaxation based since only capacitors are required as the frequency-selective elements. Sinusoidal VCOs on the other hand often require external varactors and inductors for defining oscillation frequency and hence are not suitable for monolithic integration. This dissertation also explores new sinusoidal VCO configurations that do not depend on varactor elements for frequency tuning.

A sinusoidal oscillator normally relies on an LC tuned circuit for defining the oscillation frequency and for reducing noise and distortion in the output signal. Current oscillator circuits often utilize external microstrip inductors. This hybrid approach is, however, undesirable because of the additional assembly cost, and a more serious drawback is due to parasitic packaging elements associated with the external inductors. In the early development of silicon integrated circuits, planar inductors were investigated, but the prevailing lithographic limitations and relatively large inductance requirements resulted in excessive

silicon area and poor performance. Through use of a silicon bipolar IC process featuring oxide isolation and multilayer metal options, practical inductors at microwave frequencies have been fabricated and fully characterized.

This dissertation also investigates the application of monolithic inductors in the design and fabrication of Si bipolar RF bandpass amplifiers. Inductors are used to boost circuit gain and to improve matching and noise performance.

1.2. Thesis Organization

Chapter 2 presents the oscillator models and defines the concept of circuit instability. Methods for predicting the frequency and amplitude of oscillation are studied in Chapter 3. We investigate the limitations in the traditional start-up conditions and propose circuit techniques for fully analyzing the linear behavior of oscillator circuits. The *multi-oscillation* phenomenon is analyzed in detail. Conditions for achieving *frequency stability* and *amplitude stability* are derived for use in the design of well-behaved, frequency-stable, and amplitude-stable sinusoidal oscillator circuits. In Chapter 4 we study the interaction between circuit components in negative-resistance oscillators, and then explore a design methodology for microwave oscillators based on the negative-resistance model. The results obtained from this study are applied to the design and analysis of a widely-used but poorly-characterized microwave oscillator configuration. In Chapter 5, passive inductors and LC filters fabricated in standard silicon IC technology are demonstrated. Chapter 6 presents a novel sinusoidal VCO circuit configuration and a monolithic implementation of this circuit. The application of monolithic inductors to the realization of Si bipolar monolithic RF amplifiers is investigated in Chapter 7. Chapter 8 concludes with a research summary and indicates potential future research topics.

Chapter 2 - Oscillator Characteristics and Models

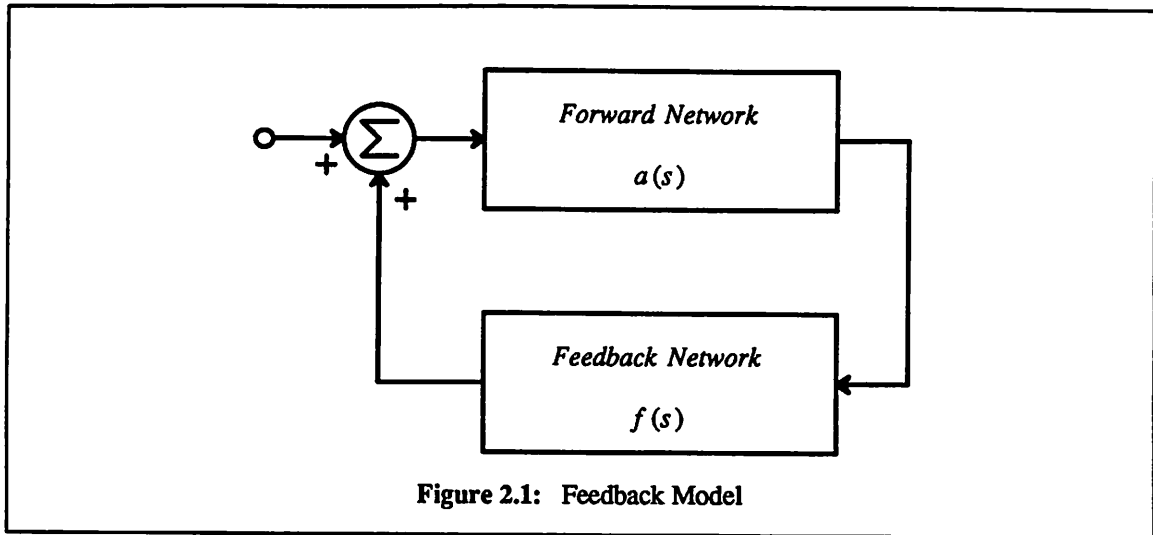
2.1. Oscillator Characteristics

An oscillator is an autonomous analog circuit whose function is to generate a stable and periodic waveform. Oscillator circuits can be classified in two groups: relaxation oscillators and sinusoidal oscillators. A *relaxation* oscillator produces a non-sinusoidal output signal as the circuit switches back and forth between two astable (unstable equilibrium) states. Such an output signal has relatively high harmonic content and is suitable for applications where high spectral purity is not important. A thorough discussion of relaxation oscillators can be found in [Liu88, Ped89]. A *sinusoidal* oscillator, as the name implies, is capable of producing a near-sinusoidal signal and has broad application in communication systems. Sinusoidal oscillators usually use LC tuned circuits, crystals [Fre78], or dielectric resonators [Bah88] for defining the oscillation frequency. Henceforth, unless otherwise stated, the term *oscillator* is used to mean a sinusoidal oscillator. An oscillator circuit is typically characterized by

- The oscillation frequency, f_o .
- The oscillation amplitude, A_o , which indicates the available output power.
- The degree to which the oscillation frequency can remain constant given variations in nonlinear circuit elements (*frequency stability*).
- The stability of the output signal due to random excitation (*amplitude stability*).
- The spectral purity of the output signal which is affected by frequency-modulated (FM) and amplitude-modulated (AM) noise, and by harmonic distortion.

2.2. Oscillator Models

The analysis of oscillators can be based on two fundamental models: the *feedback* model and the *negative-resistance* model. Figure 2.1 shows the feedback model in which an oscillator is decomposed into a forward network and a feedback network. If the circuit is *unstable* about its operating point (natural frequencies in the right half plane of the complex-frequency plane), then given an initial excita-

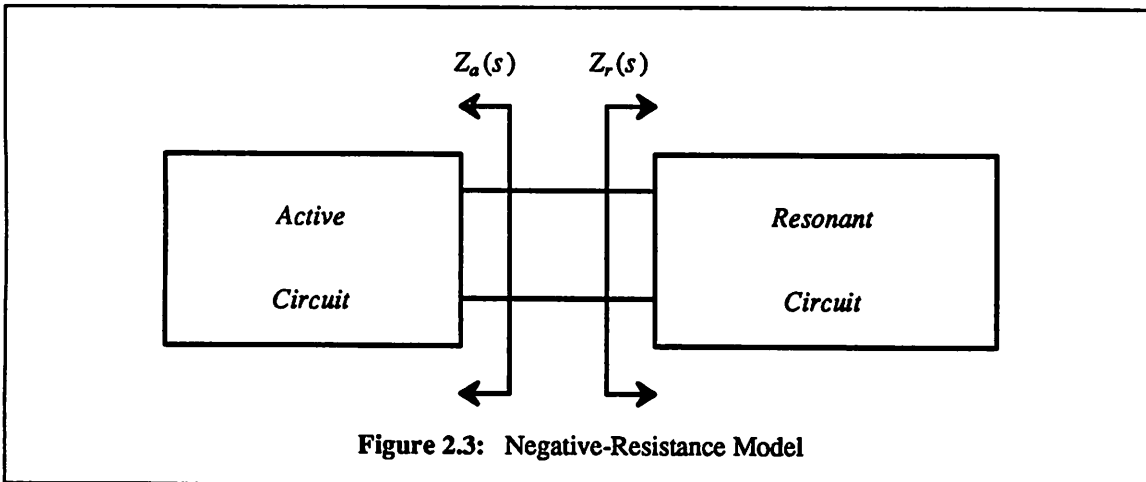
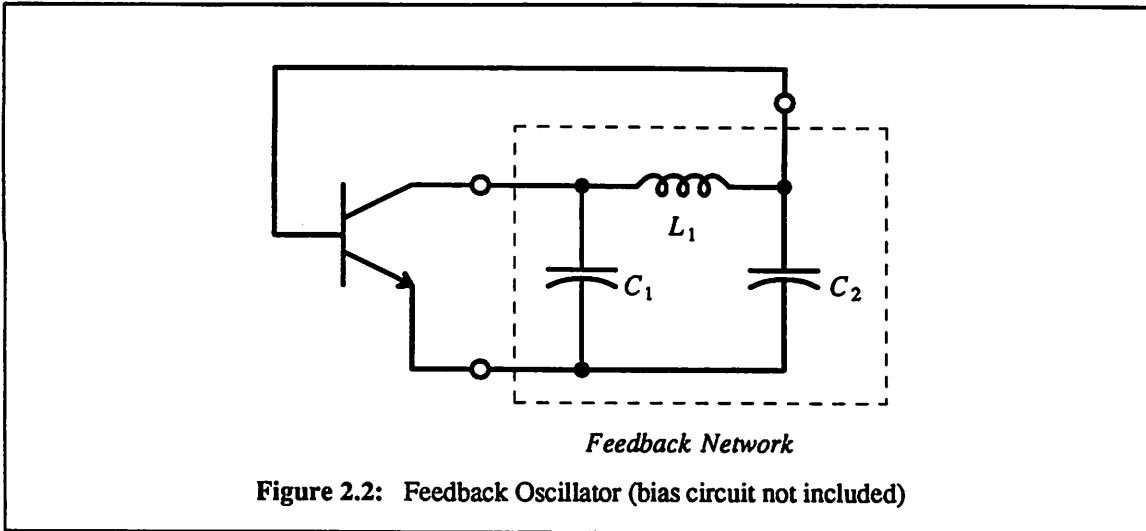


tion, it produces a growing transient. As the signal becomes large, the active devices in the circuit become nonlinear and eventually limit the growth of the signal. Since an oscillator is an autonomous circuit, electronic noise in the circuit or power supply turn-on transient can provide the initial excitation that initiates the oscillation build-up. Figure 2.2 shows how the Colpitts oscillator can be viewed as a feedback circuit. We note that both the forward and feedback networks are multi-port circuits. For ease of reference, henceforth, the term *feedback oscillator* is used to denote an oscillator circuit that can be analyzed using the feedback model. The linear behavior of a feedback circuit is typically studied with the loop gain quantity, defined as the product of the forward and feedback transfer functions $a(s)$ and $f(s)$,

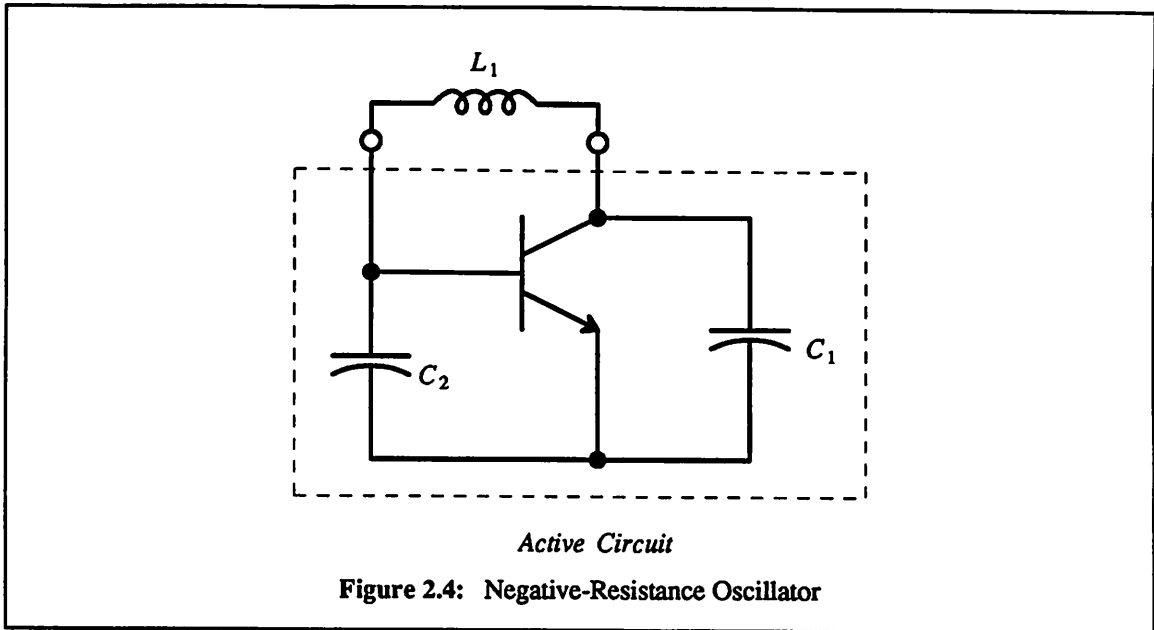
$$T(s) = a(s)f(s). \quad (2.1)$$

It is shown in Section 2.3 that the expression $1 - T(s) = 0$ gives the *characteristic equation* of the circuit from which the natural frequencies are found.

Figure 2.3 show the negative-resistance model in which an oscillator is separated into a one-port *active* circuit and a one-port *resonant* circuit. The function of the active circuit is to produce a small-signal negative resistance about the operating point of the oscillator circuit and to couple with the resonant circuit for defining the frequency of oscillation. The resonant circuit is usually a linear time-invariant circuit and is signal independent. Figure 2.4 shows how the Colpitts oscillator can be separated



into an active circuit and a resonant circuit. We use the term *negative-resistance oscillator* to denote an oscillator circuit that can be analyzed using the negative-resistance model. In Fig. 2.3, the active and resonant circuits are characterized by impedance quantities $Z_a(s)$ and $Z_r(s)$, respectively. They can also be characterized in terms of active admittance $Y_a(s)$ and resonant admittance $Y_r(s)$. It is shown in the next section that the characteristic equation of a negative-resistance oscillator can be derived from either the expression $Z_a(s) + Z_r(s) = 0$ or $Y_a(s) + Y_r(s) = 0$. The negative-resistance model has been widely used in the design of microwave oscillators due to its simplicity. Many negative-resistance oscillators use the one-port tunnel diodes and avalanche diodes as the active circuits.



2.3. Natural Frequencies

As a basic requirement for producing a self-sustained near-sinusoidal oscillation, an oscillator must have a pair of complex-conjugate natural frequencies in the right-half plane (RHP)

$$P_{1,2} = \alpha + j\beta . \quad (2.2)$$

While this requirement does not always guarantee an oscillation in the steady state, it is nevertheless a necessary requirement for any well-behaved oscillator. When excited by electronic impulses, the RHP natural frequencies in (2.2) give rise to a sinusoidal signal with an exponential growing envelope

$$x(t) = K e^{\alpha t} \cos(\beta t) . \quad (2.3)$$

The growth of this signal is eventually limited by the nonlinearities of the active devices. As mentioned above, the application of either the feedback model or the negative-resistance model is sufficient for analyzing the linear behavior of an oscillator. The analysis is essentially a study of the natural frequencies from the *characteristic equation* of the circuit. One common procedure to obtain the characteristic equation is to equate the determinant of the circuit's *homogeneous system of algebraic equations* to zero [Chu87].

In the following paragraphs we study other methods for deriving the characteristic equations in feedback and negative-resistance oscillators. In Fig. 2.5, we assume that a feedback oscillator can be represented by the two-port Y networks. The current source I_s models electronic impulses in the circuit.

The system of algebraic equations for this circuit is

$$I_s = (Y_{11a} + Y_{11f}) V_i + (Y_{12a} + Y_{12f}) V_o \quad (2.4)$$

$$0 = (Y_{21a} + Y_{21f}) V_i + (Y_{22a} + Y_{22f}) V_o . \quad (2.5)$$

The determinant of the above system is simply

$$D(s) = (Y_{11a} + Y_{11f})(Y_{22a} + Y_{22f}) - (Y_{21a} + Y_{21f})(Y_{12a} + Y_{12f}) . \quad (2.6)$$

We now derive the transfer function V_o / I_s . It can be shown that

$$\frac{V_o(s)}{I_s(s)} = \frac{-(Y_{21a} + Y_{21f})}{(Y_{11a} + Y_{11f})(Y_{22a} + Y_{22f}) - (Y_{21a} + Y_{21f})(Y_{12a} + Y_{12f})} . \quad (2.7)$$

It is useful to define

$$a(s) = \frac{(Y_{21a} + Y_{21f})}{(Y_{11a} + Y_{11f})(Y_{22a} + Y_{22f})} \quad (2.8)$$

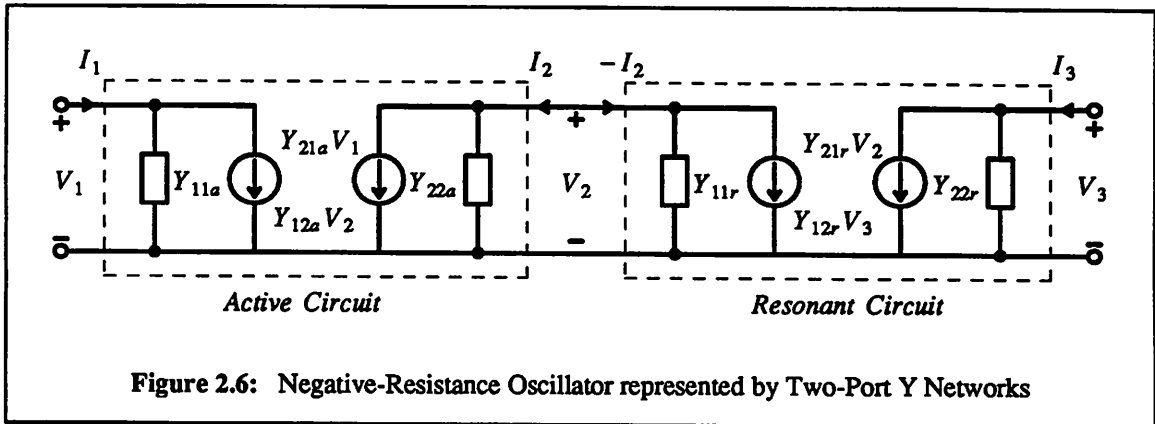
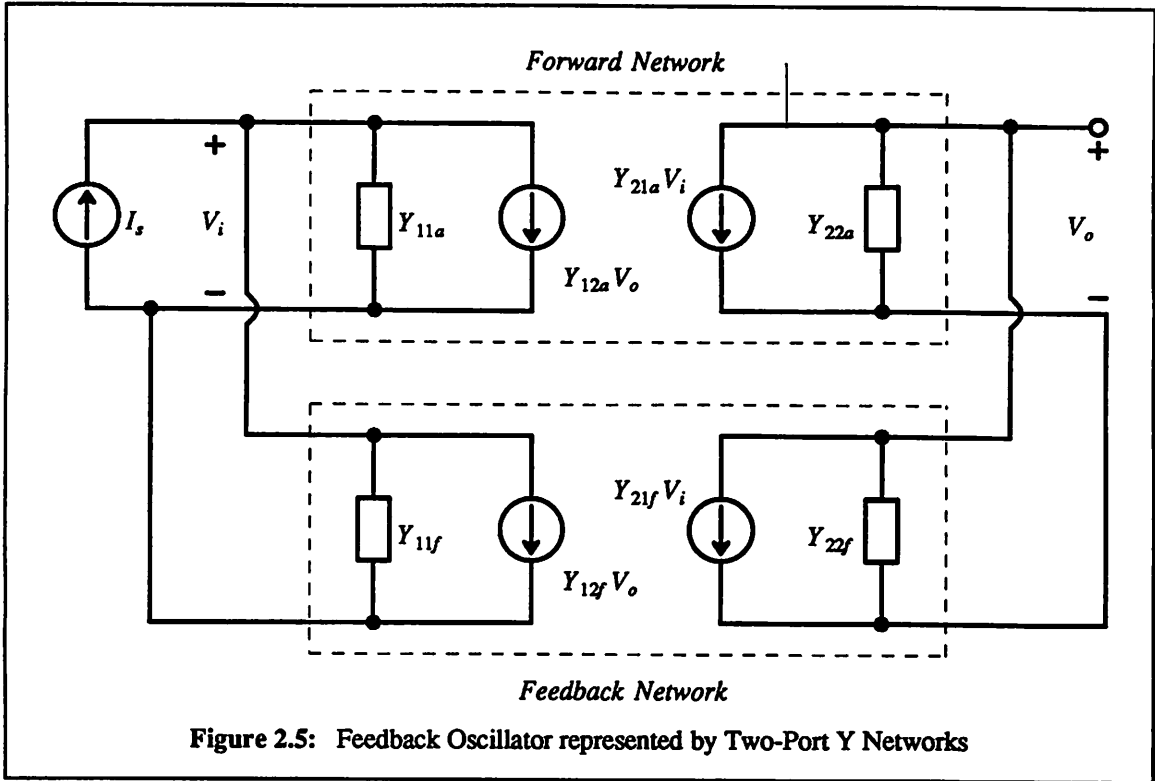
$$f(s) = (Y_{12a} + Y_{12f}) . \quad (2.9)$$

Using the definitions (2.8) and (2.9) in (2.7) yields the ideal feedback equation

$$\frac{V_o(s)}{I_s(s)} = \frac{-a(s)}{1 - a(s)f(s)} = \frac{-a(s)}{1 - T(s)} . \quad (2.10)$$

We note from (2.6), (2.7), and (2.10) that the characteristic equation of a feedback oscillator can also be determined from the expression $1 - T(s) = 0$. This provides us with another method for analyzing the linear behavior of feedback oscillators.

Figure 2.6 shows one general representation of a negative-resistance oscillator. We assume that the active and resonant circuits can be modeled by the two-port Y networks. The system of algebraic equations is



$$\begin{aligned}
 I_1 &= Y_{11a} V_1 + Y_{12a} V_2 \\
 I_2 &= Y_{21a} V_1 + Y_{22a} V_2 \\
 -I_2 &= Y_{11r} V_2 + Y_{12r} V_3 \\
 I_3 &= Y_{21r} V_2 + Y_{22r} V_3 \\
 I_2 &= 0 \\
 I_3 &= 0
 \end{aligned}
 \tag{2.11}$$

The determinant of the system (2.11) is

$$D(s) = Y_{11a} (Y_{11r} Y_{22r} - Y_{21r} Y_{12r}) + Y_{22r} (Y_{11a} Y_{22a} - Y_{21a} Y_{12a}). \quad (2.12)$$

If we characterize the active and resonant circuits by equivalent admittances $Y_a(s)$ and $Y_r(s)$, respectively, we can show that

$$Y_a(s) = Y_{22a} - \frac{Y_{21a} Y_{12a}}{Y_{11a}} \quad (2.13)$$

$$Y_r(s) = Y_{11r} - \frac{Y_{21r} Y_{12r}}{Y_{22r}}. \quad (2.14)$$

Now by equating the sum of (2.13) and (2.14) to zero, we obtain

$$Y_a(s) + Y_r(s) = 0 = Y_{11a} (Y_{11r} Y_{22r} - Y_{21r} Y_{12r}) + Y_{22r} (Y_{11a} Y_{22a} - Y_{21a} Y_{12a}). \quad (2.15)$$

We note from (2.15) that the expression $Y_a(s) + Y_r(s) = 0$ gives the same characteristic equation (2.12), and thus provides us with another method for studying the linear behavior of negative-resistance oscillators. By similar analysis, we can show that if the active and resonant circuits are characterized by equivalent impedances $Z_a(s)$ and $Z_r(s)$, respectively, the expression $Z_a(s) + Z_r(s) = 0$ also gives the same characteristic equation.

2.4. Summary

Both feedback and negative-resistance models for analyzing oscillator circuits have been discussed in this chapter. The concept of circuit instability has also been defined. An oscillator circuit must be unstable about its bias point or, equivalently, have natural frequencies in the right half plane of the complex-frequency domain if an oscillation build-up is to take place. The natural frequencies can be found from the characteristic equation of the circuit. For a feedback oscillator, the characteristic equation is given by the expression $1 - T(s) = 0$. For a negative-resistance oscillator, the characteristic equation is given by either the expression $Z_a(s) + Z_r(s) = 0$ or $Y_a(s) + Y_r(s) = 0$.

Chapter 3 - Oscillator Analyses

3.1. Introduction

Analytical expressions governing the initial and steady-state responses of feedback and negative-resistance oscillator circuits are discussed in this chapter. The conventional start-up conditions that have been used for predicting whether an oscillation build-up can take place in an oscillator are reexamined. It is shown that these conditions are not always valid and can provide misleading results. This conclusion helps provide explanations to many examples of unpredictable oscillation behavior observed in practice. Methods for predicting the frequency and amplitude of oscillation are also explored in this chapter. Conditions for achieving frequency stability and amplitude stability are derived for use in the design of well-behaved, frequency-stable, and amplitude-stable sinusoidal oscillator circuits.

3.2. Small-Signal Analysis

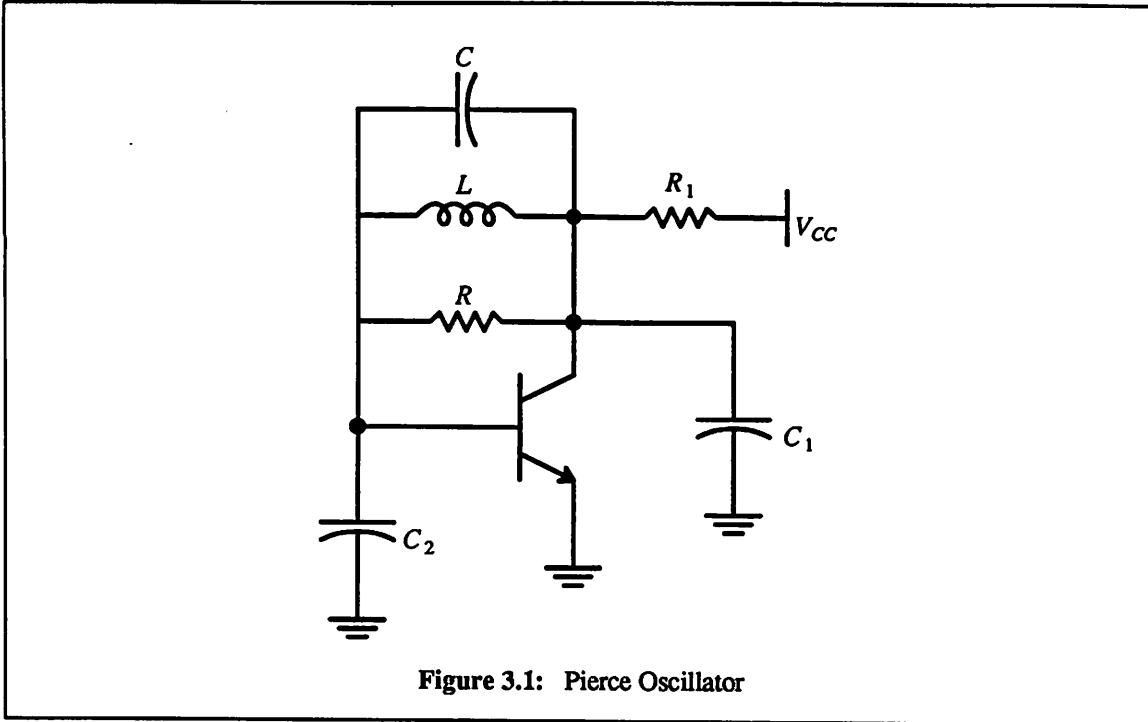
Electronic noise can produce growing transients in an oscillator provided that the circuit has natural frequencies in the RHP. As long as the transients are small, the initial response of the oscillator can be analyzed using linear analyses such as the Nyquist, Bode, and root locus [Lin61]. As mentioned in Chapter 2, the small-signal analysis of an oscillator is essentially a study of the circuit's natural frequencies.

3.2.1. Feedback Oscillators

For a feedback oscillator circuit, the fulfillment of the following well-known condition has been used as an indication that the circuit is unstable (it can produce an expanding transient when subject to an initial excitation)

$$\text{Ph} \{ T(\omega_z) \} = 0 \quad \text{Mag} \{ T(\omega_z) \} > 1. \quad (3.1)$$

In (3.1), T denotes the loop gain expression and ω_z denotes the *zero-phase* frequency at which the total phase shift through both the forward and feedback networks is zero. It is important, however, to keep in mind that there are oscillator circuits that meet the start-up condition (3.1) but are, nevertheless, stable



circuits and hence cannot produce an oscillation. Equivalently stated, the fulfillment of condition (3.1) does not necessarily imply that a circuit is unstable.

The above remark is now illustrated through use of the Pierce oscillator shown in Fig. 3.1. For simplicity, circuit elements r_b , r_o , and C_μ of the bipolar transistor are neglected. After lumping the remaining parasitic elements of the transistor to the appropriate passive elements, we can show that the loop gain of the circuit is

$$T(s) = -T_o \frac{s^2 LC + s \frac{L}{R} + 1}{a_3 s^3 + a_2 s^2 + a_1 s + a_0} \quad (3.2)$$

where

$$T_o = g_m R_1$$

$$a_3 = LC_2 R_1 C_1 \left(1 + \frac{C}{C_1} + \frac{C}{C_2}\right)$$

$$a_2 = L(C + C_2) + \frac{L}{R} R_1 (C_1 + C_2)$$

$$a_1 = \frac{L}{R} + R_1 (C_1 + C_2)$$

$$a_0 = 1.$$

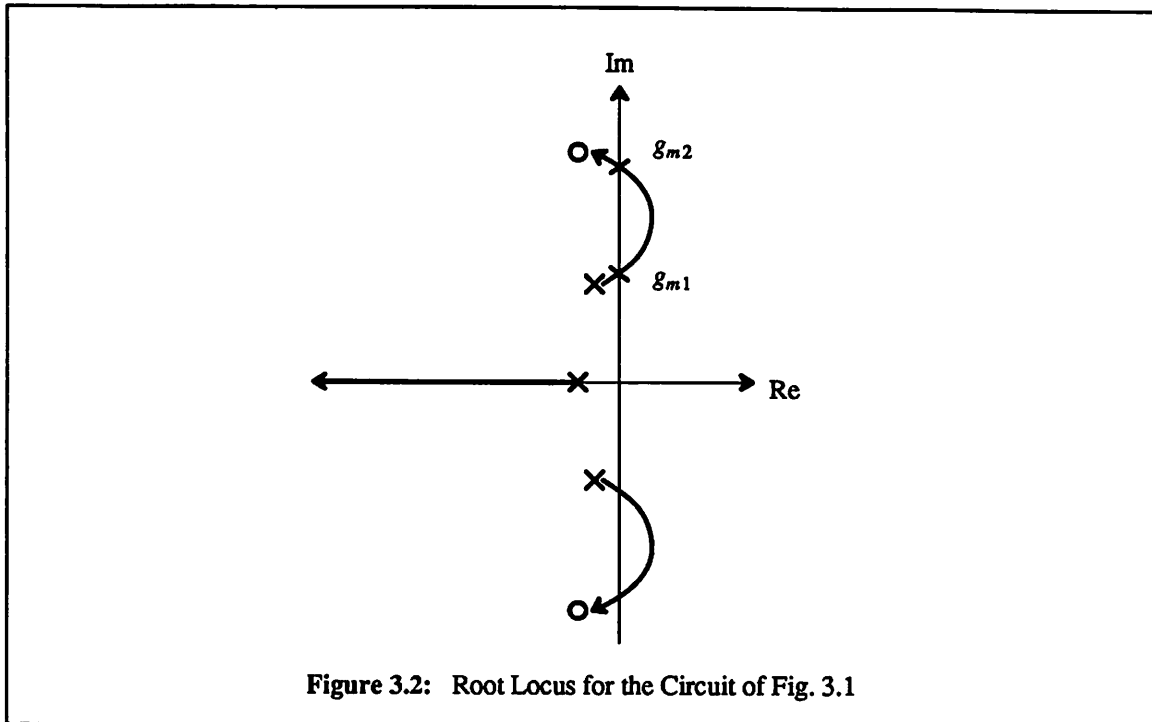
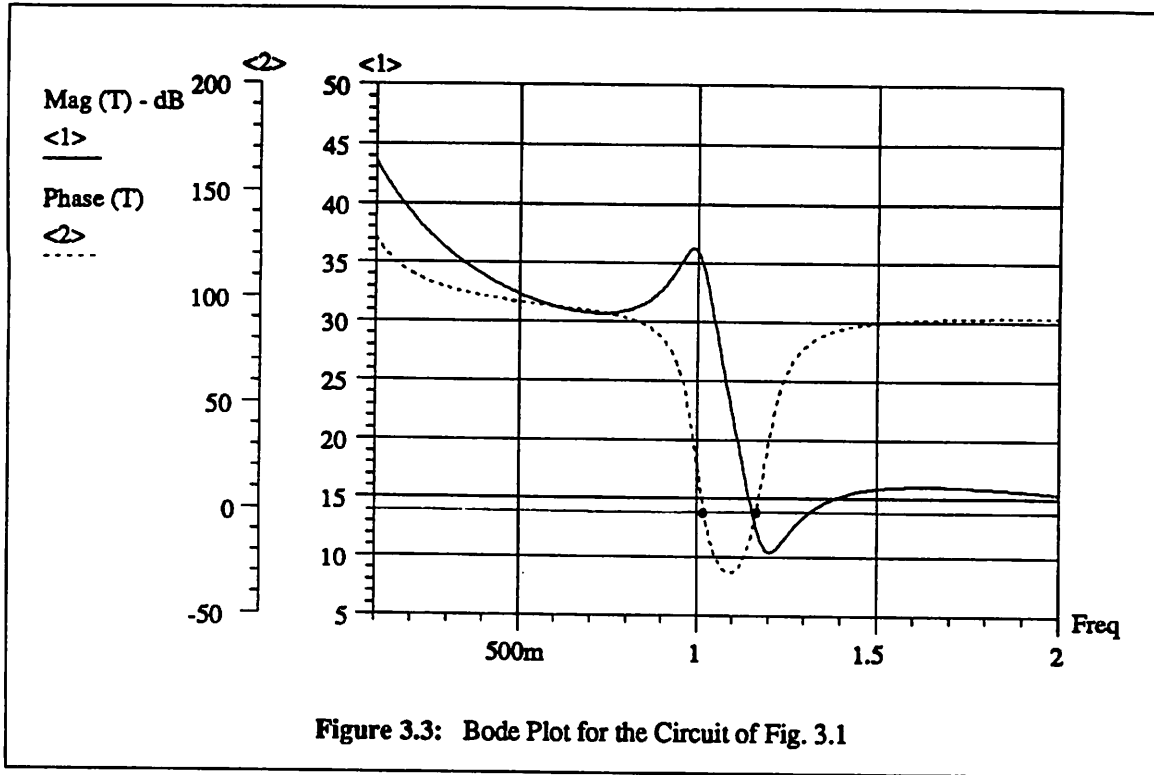


Figure 3.2: Root Locus for the Circuit of Fig. 3.1

The natural frequencies can be determined from the roots of the expression $1 - T(s) = 0$. Figure 3.2 shows the root locus as a function of quantity $g_m (= I_C / V_T)$. Quantities g_{m1} and g_{m2} denote the bias current range for which the circuit has a pair of RHP natural frequencies. From this plot we observe that with adequate dc loop gain ($g_{m1}R_1 \leq T_o \leq g_{m2}R_1$), the complex-conjugate natural frequencies enter the RHP from the left-half plane (LHP) of the complex-frequency plane. Under this situation the circuit is unstable and would produce a growing sinusoidal signal in response to electronic impulses. If the loop gain is too large ($g_m > g_{m2}$), however, it is interesting to note that the complex natural frequencies reenter the LHP. Under this situation the circuit is stable and would produce a decaying sinusoidal signal in response to electronic impulses. The Bode plot for the case $g_m > g_{m2}$ is shown in Fig. 3.3. We note that there are two frequencies, ω_{z1} and ω_{z2} , where (3.1) is clearly satisfied but the circuit is yet stable according to the root locus of Fig. 3.2. To further confirm this observation, we generate the Nyquist plots of (3.2) in Fig. 3.4(a) and Fig. 3.4(b) for $g_{m1} < g_m < g_{m2}$ and $g_m > g_{m2}$, respectively. It is helpful to recall the Nyquist criterion:



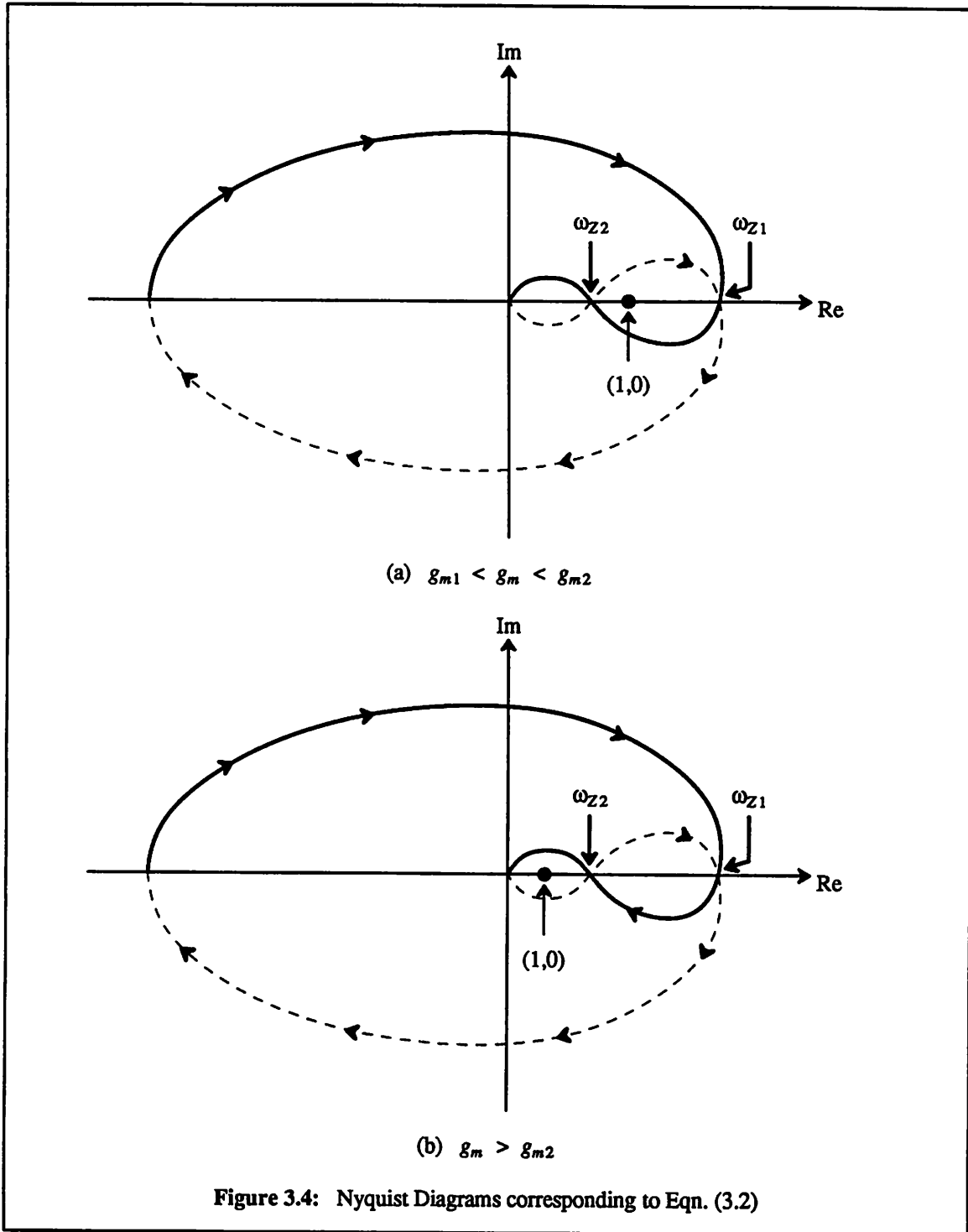
If the polar plot of $T(\omega)$ plus its mirror image encircles the point $(1,0)$ in a clockwise direction as ω varies from zero to infinity, the circuit is unstable [Che68].

In Fig. 3.4(a), there are two clockwise encirclements of the point $(1,0)$ which indicates the existence of two RHP natural frequencies. In Fig. 3.4(b), the net clockwise encirclement of the point $(1,0)$ is zero which confirms that for $g_m > g_{m2}$, the circuit is indeed stable.

The above analysis affirms that the start-up condition (3.1) is not always sufficient for predicting the circuit instability and should be used with the full knowledge of its limitation. As a rule of thumb, the condition (3.1) is valid if it holds at only one frequency ω_s .

3.2.2. Negative-Resistance Oscillators

The negative-resistance model of Fig. 2.3 is often used in the design of microwave oscillators due to its simplicity. Assume that the active and resonant circuits are modeled by impedances $Z_a = R_a + jX_a$ and $Z_r = R_r + jX_r$, respectively, where R and X denote the resistance and reactance. The following start-up condition has been widely used as an indication of circuit instability [Gon84, Elk86, Maa86]



$$R_a(\omega_x) + R_r(\omega_x) < 0 \quad 3.3(a)$$

$$X_a(\omega_x) + X_r(\omega_x) = 0. \quad 3.3(b)$$

In the above equations, frequency ω_x denotes a frequency at which the total reactive component

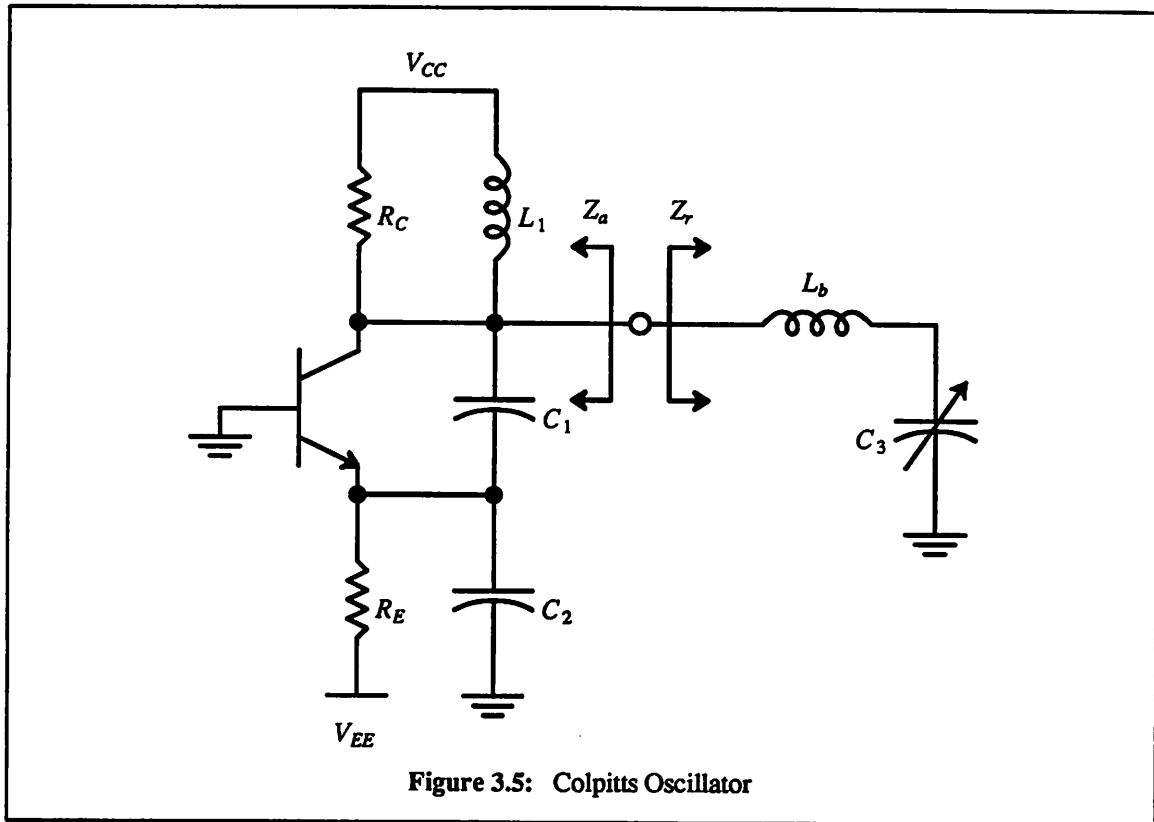
$X_a + X_r$ equals zero. It is important to distinguish the frequency ω_x from the frequency ω_z of the start-up condition (3.1) since even though an oscillator circuit can be analyzed using either the negative-resistance model or feedback model, a frequency ω_x that fulfills the condition (3.3) is not necessarily the same frequency that fulfills the condition (3.1). This point is further illustrated in Section 3.2.4. It is also important to emphasize that an underlying assumption in (3.3) is that the current entering the active circuit in the steady state must be near-sinusoidal. If, instead, the voltage across the active circuit is near-sinusoidal, the active and resonant circuits should be modeled in terms of parallel admittances $Y_a = G_a + jB_a$ and $Y_r = G_r + jB_r$, respectively, where G and B denote the conductance and susceptance. The dual start-up condition is then

$$G_a(\omega_x) + G_r(\omega_x) < 0 \quad 3.4(a)$$

$$B_a(\omega_x) + B_r(\omega_x) = 0. \quad 3.4(b)$$

In the following paragraphs we show that the conditions (3.3) and (3.4) are not always valid for predicting circuit instability, especially in oscillator circuits operating in the microwave region where the effect of parasitic elements becomes more significant.

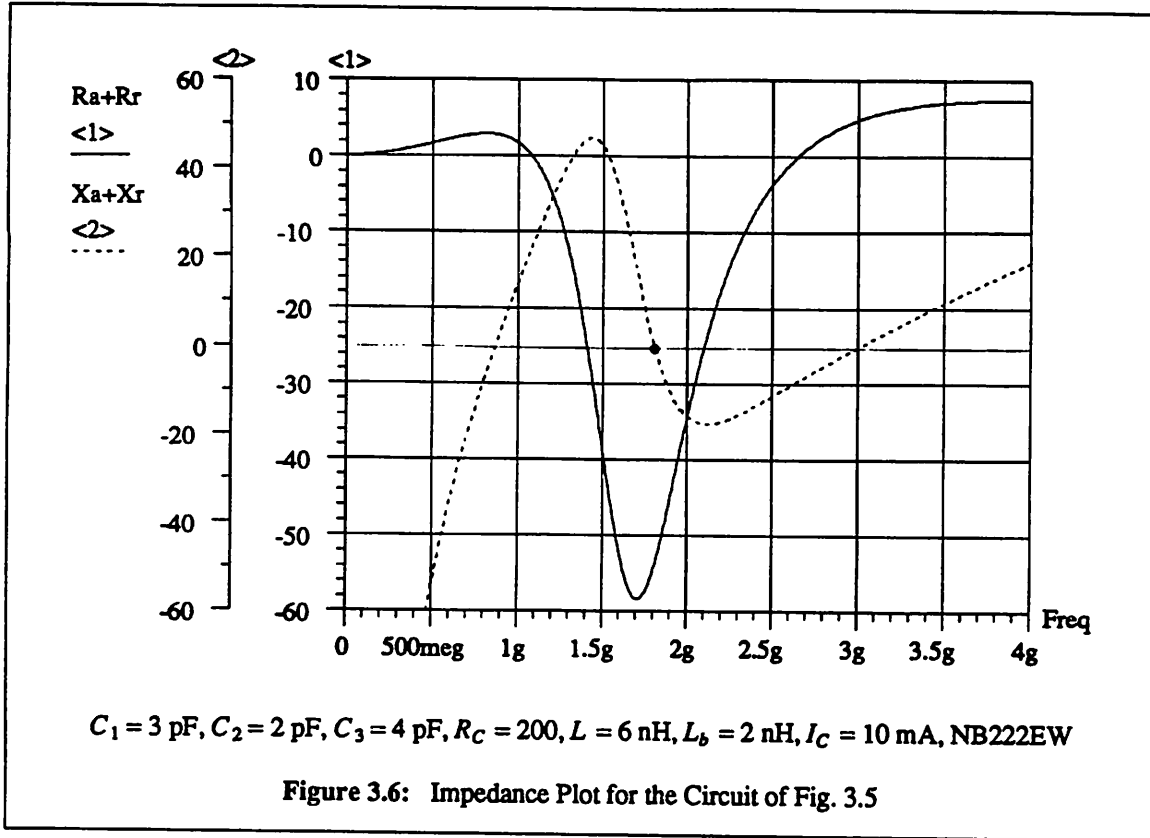
To illustrate the above point, we consider a high-frequency Colpitts oscillator shown in Fig. 3.5. In this circuit, C_3 is an off-chip varactor used for tuning the oscillation frequency and L_b models the bond-wire inductance. With the active and resonant circuits defined as shown in Fig. 3.5, the total resistance $R_a + R_r$ and reactance $X_a + X_r$ are plotted in Fig. 3.6 for the given set of circuit parameters. At the frequency 1.8 GHz, (3.3) is satisfied. Without understanding the limitations of this start-up condition, we would be inclined to assert that the circuit is unstable under this condition and is capable of producing an expanding transient. The transient plot in Fig. 3.7 shows, however, a decaying sinusoidal waveform instead of a growing waveform, indicating that the circuit is stable. As a check we generate the Nyquist plot for the circuit in Fig. 3.8. Since there is no clockwise encirclement of the point (1,0), the circuit is indeed stable. One characteristic that may attribute the misleading indication of the condition (3.3) in this circuit is that the reactive plot as shown in Fig. 3.6 crosses the zero point at multiple frequencies.



Since the start-up conditions (3.1), (3.3), and (3.4) are not always sufficient for studying the circuit instability, the root-locus and Nyquist analyses should be used when in doubt. Throughout this dissertation, unless specifically stated, the start-up conditions for both oscillator models are assumed valid.

3.2.3. Multi-Oscillation

In the microwave region, the effect of parasitic elements in an oscillator circuit becomes more significant and can give rise to a *multi-oscillation* phenomenon. It is a phenomenon in which two or more oscillations exist simultaneously in the steady state. In other words, there are parasitic or unwanted oscillations existing together with a main oscillation. Due to the multiple oscillations, the resultant steady-state signal is severely distorted and hence has limited application in communication systems. It is worth mentioned that the multi-oscillation phenomenon is quite different from that of a multi-mode oscillator [Eds55]. A multi-mode oscillator uses an arbitrary number of tuned circuits for defining a well-defined set of oscillation frequencies, and when subject to an injected instruction signal, the circuit oscillates at



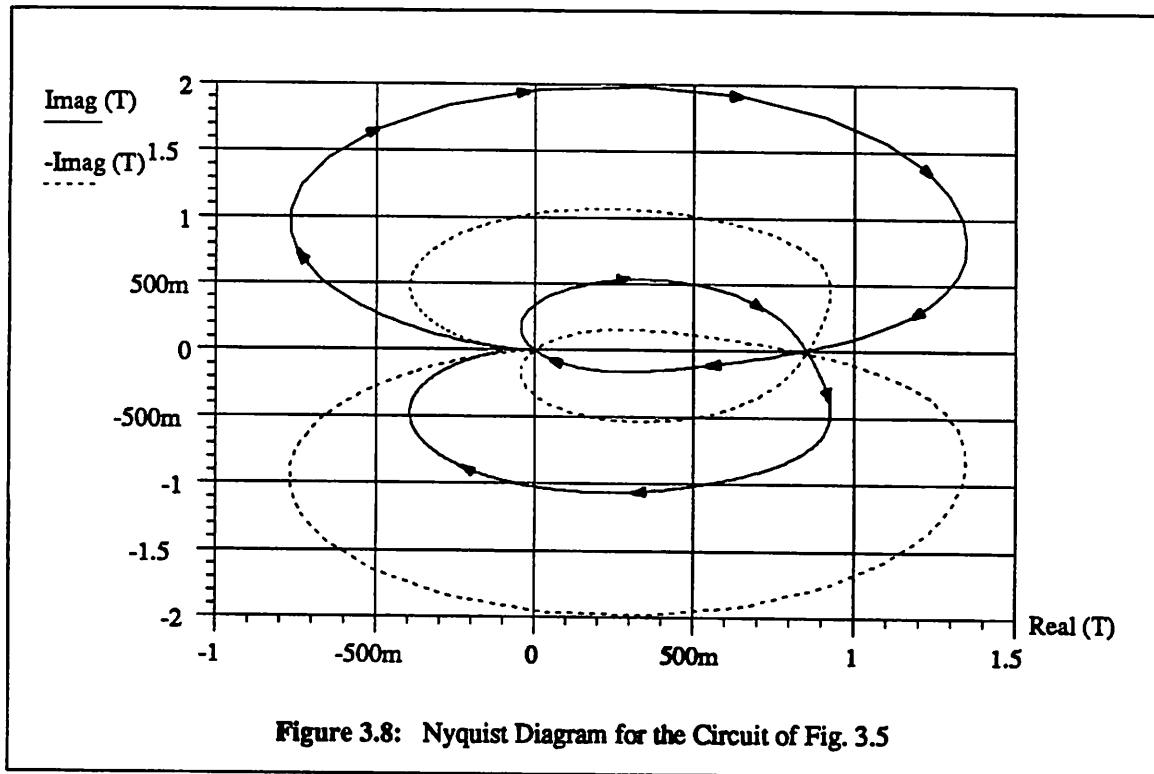
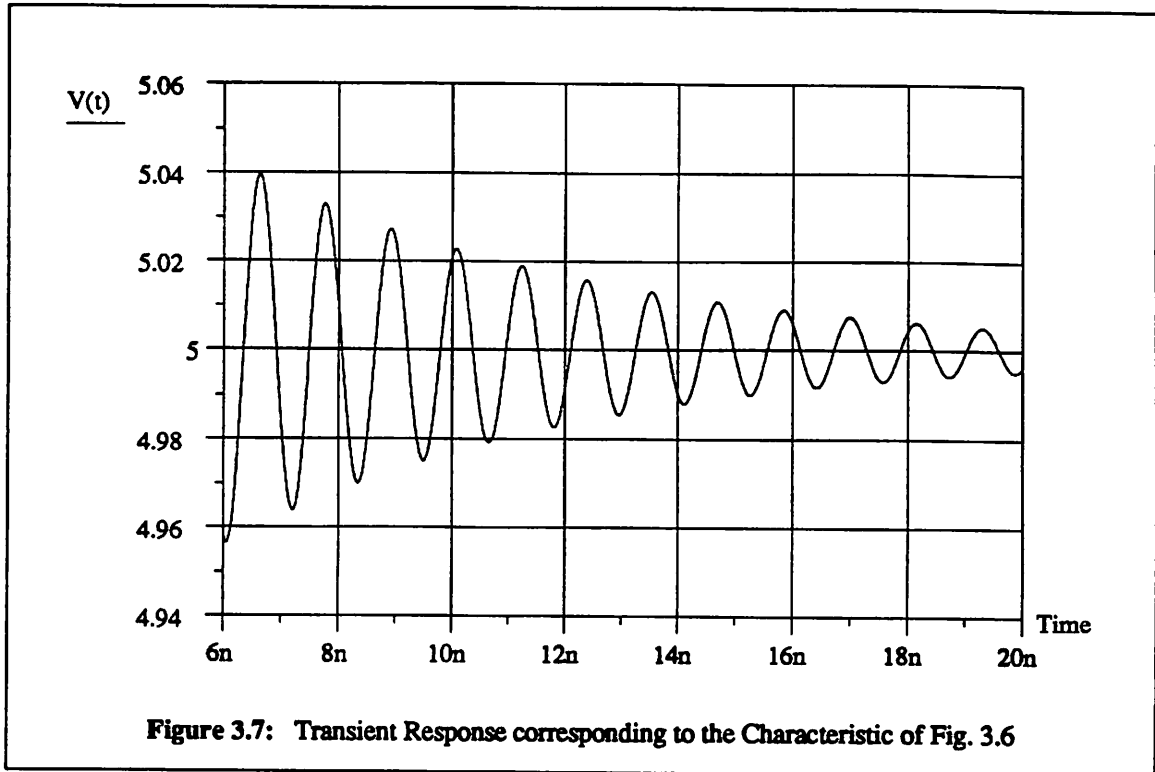
only one of these well-defined frequencies.

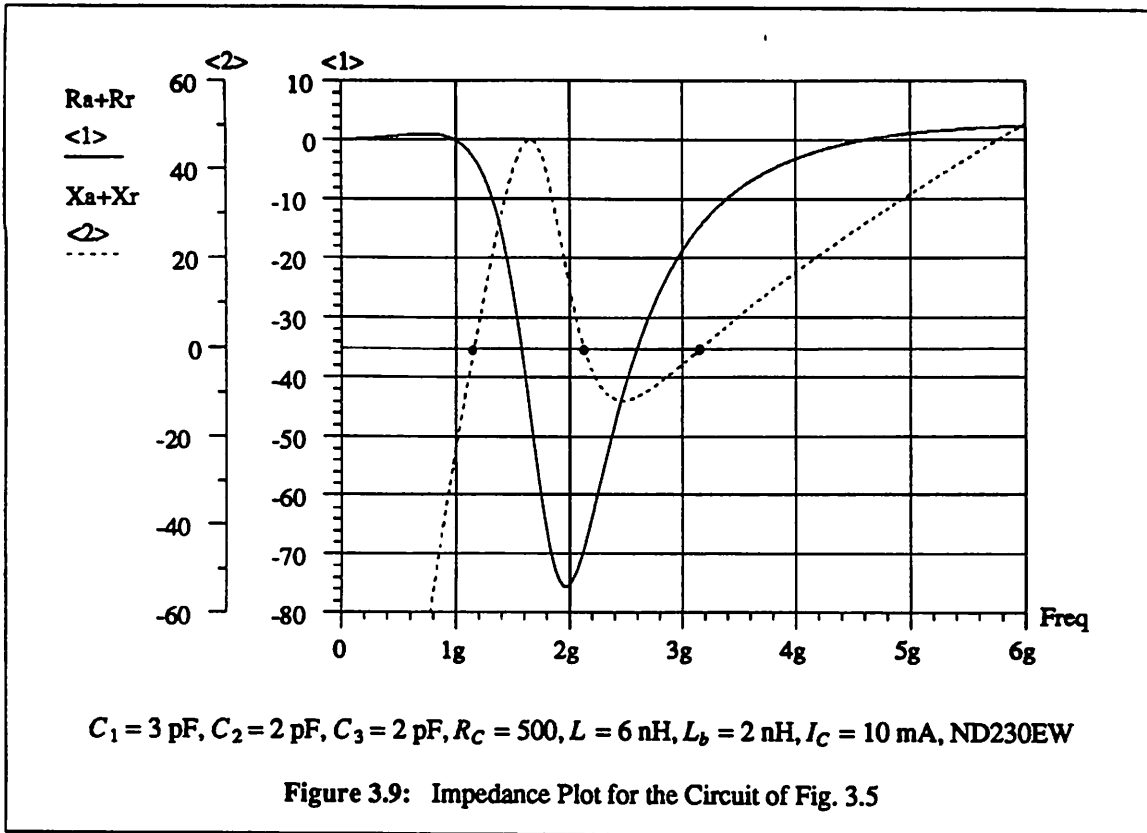
The circuit configuration shown in Fig. 3.5 can also be used for studying the multi-oscillation behavior. In Fig. 3.9 the impedance as a function of frequency is generated for the new set of circuit parameters. We note that the start-up condition (3.3) is now satisfied at three frequencies. It is not clear from Fig. 3.9 how the transient response would behave and whether there is a well-defined oscillation frequency in the steady state. In order to obtain further insight into the circuit operation, we construct the root locus based on the characteristic equation from $Z_a(s) + Z_r(s) = 0$. The root locus as a function of bias current is shown in Fig. 3.10. Due to the bond-wire inductance L_b , we observe that the circuit can possess two pairs of RHP complex-conjugate natural frequencies

$$P_{1,2} = \alpha_1 + j\beta_1 \quad \text{and} \quad P_{3,4} = \alpha_2 + j\beta_2. \quad (3.5)$$

Given an initial impulse, the circuit can produce a signal of the form

$$x(t) = K_1 e^{\alpha_1 t} \cos(\beta_1 t) + K_2 e^{\alpha_2 t} \cos(\beta_2 t) \quad (3.6)$$

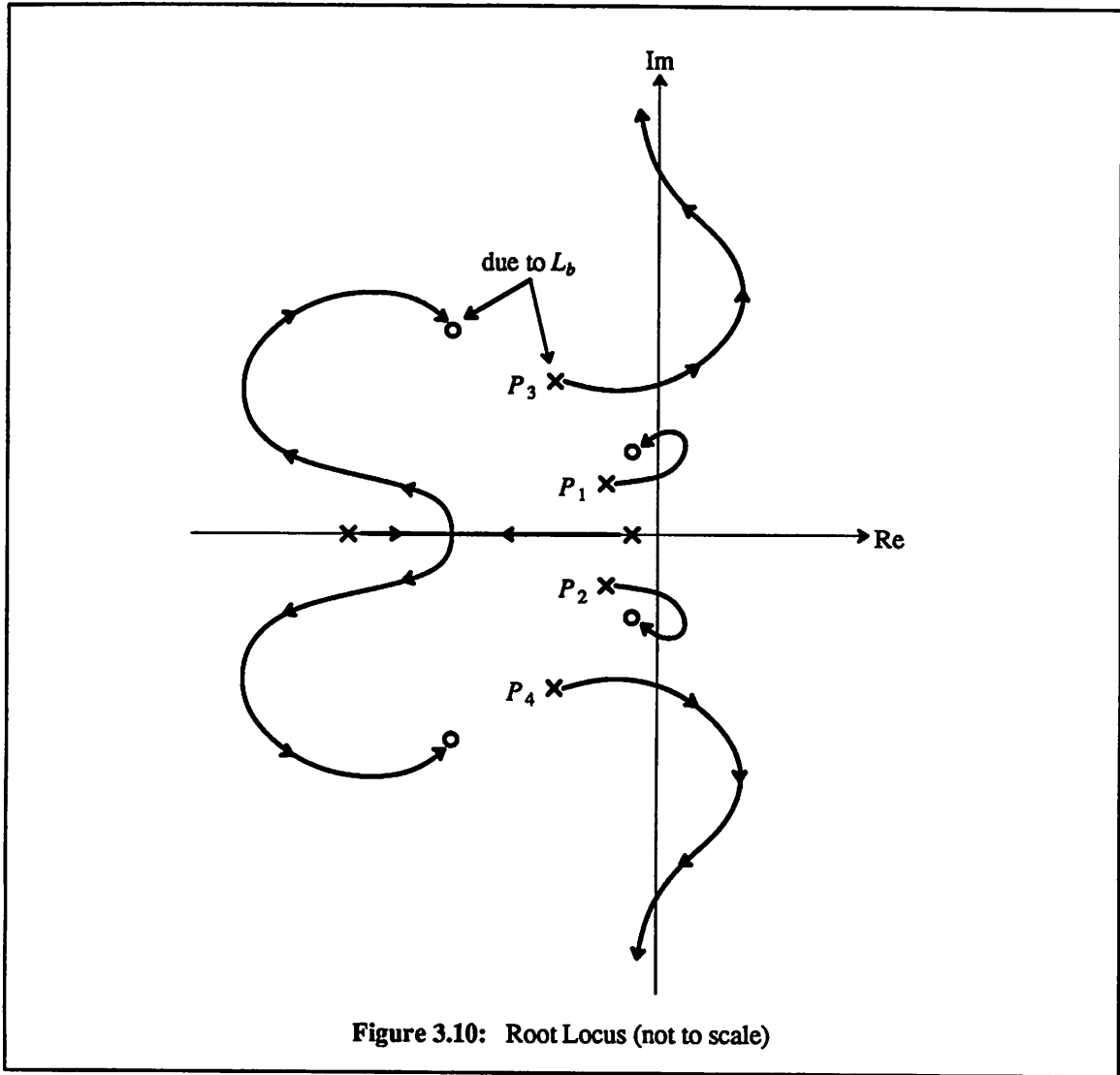




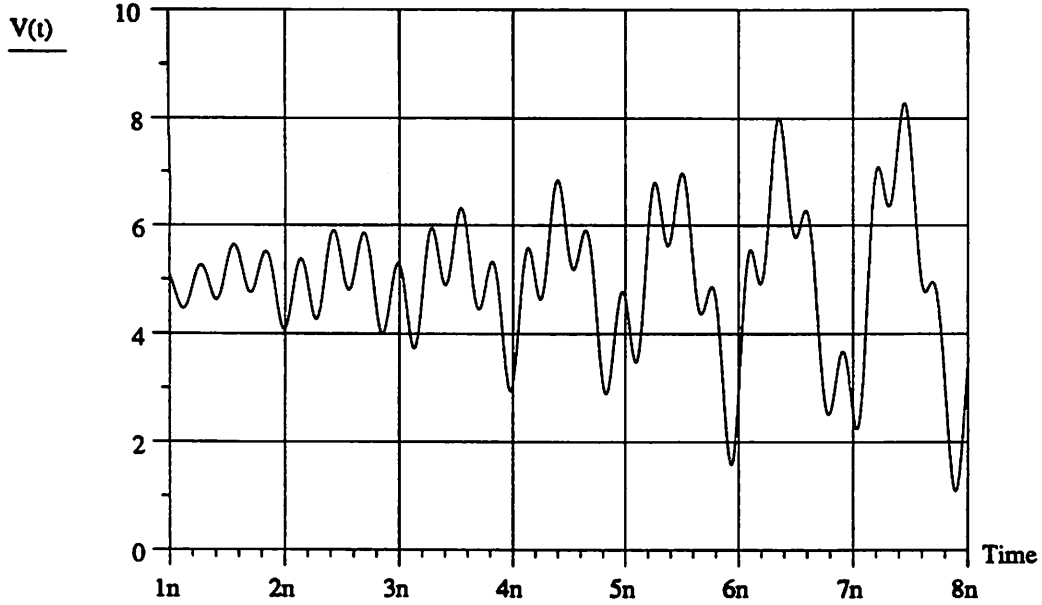
which is a sum of two concurrently growing sinusoids. Simulated time-domain waveforms during transient build-up and at steady state are shown in Fig. 3.11. Figure 3.11(a) agrees with the predicted linear behavior (3.6). Figure 3.11(b) displays the steady-state waveform which is quite distorted having two distinct frequency components. This plot suggests the simultaneous presence of two sinusoidal oscillations.

The advantages of using the root-locus analysis in oscillator design is apparent from the above analysis. This technique allows us to determine the exact location of all the natural frequencies in the circuit, and from which to identify the circuit elements that cause problems. For the circuit under consideration, one way to eliminate the multi-oscillation phenomenon is to minimize the effect of bond-wire inductance. This could be done with multiple bond-wire connections.

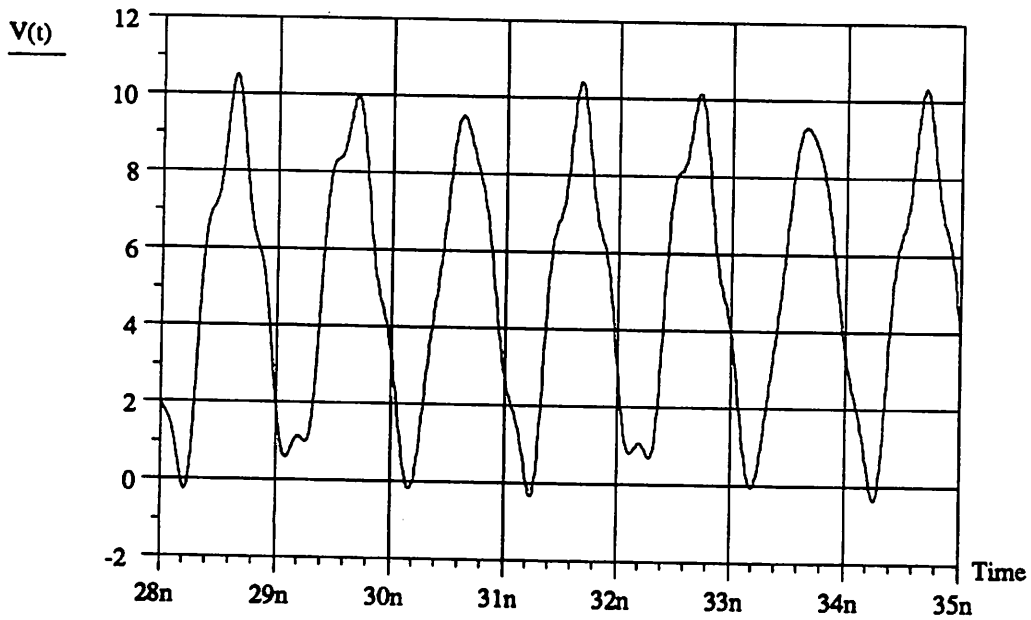
3.2.4. Predicting Oscillation Frequency from the Start-Up Conditions



The zero-phase frequency as defined in the start-up condition (3.1) is often used as an estimate for the oscillation frequency. Because of the nonlinearities in the active devices, the zero-phase frequency is not exactly equal to the frequency of oscillation. Nevertheless, it is a good approximation in oscillator circuits that have a pair of RHP complex-conjugate natural frequencies lying close to the $j\omega$ axis. Such natural frequencies are referred to as “high-Q” natural frequencies. In this section, we study whether the frequency ω_x as defined in the start-up condition of negative-resistance oscillators can also be utilized for predicting the oscillation frequency. Through use of circuit examples, we derive the frequency ω_x and frequency ω_z and make a comparison between them.

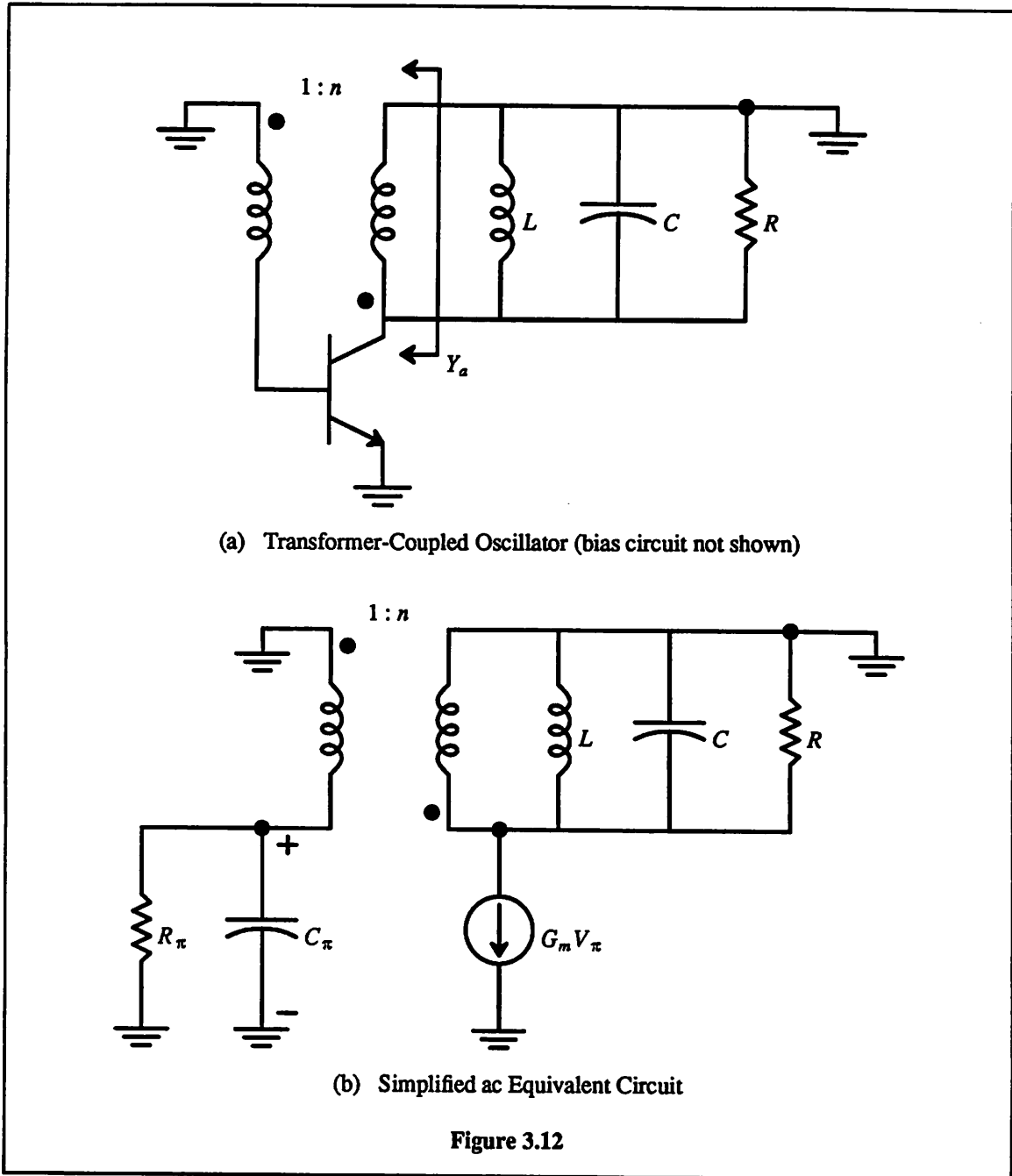


(a) Start-Up Response



(b) Steady-State Response

Figure 3.11: Transient Response corresponding to the Characteristic of Fig. 3.9



The first circuit to be investigated is the transformer-coupled oscillator shown in Fig. 3.12(a). Figure 3.12(b) shows the simplified ac equivalent circuit. We can show that the loop gain of the circuit is

$$T(s) = \frac{1}{n} \left[g_m - \frac{1}{nZ_\pi} \right] \frac{sL}{s^2LC + s\frac{L}{R} + 1} \quad (3.7)$$

where

$$Z_{\pi} = \frac{r_{\pi}}{1 + s r_{\pi} C_{\pi}} \quad (3.8)$$

$$r_{\pi} = \frac{\beta_o}{g_m} \quad (3.9)$$

$$C_{\pi} \approx g_m \tau_F . \quad (3.10)$$

Substituting (3.9) and (3.10) into (3.8) yields

$$Z_{\pi} = \frac{\beta_o}{g_m} \frac{1}{1 + s \beta_o \tau_F} . \quad (3.11)$$

Using (3.11) in (3.7) and solving for the zero-phase frequency gives

$$\omega_x = \left[L \left[C + \frac{\tau_F}{nR\eta} \right] \right]^{-\frac{1}{2}} \quad (3.12)$$

where $\eta \equiv 1 - \frac{1}{n\beta_o}$. The admittances $Y_a(s)$ and $Y_r(s)$ as defined in Fig. 3.12(a) are

$$Y_a(s) = -\frac{1}{n} \left[g_m - \frac{1}{nZ_{\pi}} \right] \quad (3.13)$$

$$Y_r(s) = \frac{1}{R} + \frac{1}{sL} + sC . \quad (3.14)$$

Substituting $s = j\omega$ into (3.13) and (3.14) yields

$$Y_a(\omega) = -\frac{g_m \eta}{n} + j\omega \frac{g_m \tau_F}{n^2} \quad (3.15)$$

$$Y_r(\omega) = \frac{1}{R} + \frac{1}{j\omega L} + j\omega C . \quad (3.16)$$

We assume that the start-up condition (3.4) is valid. From (3.15) and (3.16) the circuit is unstable if

$$\text{Real: } -\frac{g_m \eta}{n} + \frac{1}{R} \leq 0 \Leftrightarrow g_m \geq \frac{n}{R} \frac{1}{\eta} \quad (3.17)$$

$$\text{Imag: } -\frac{1}{\omega_x L} + \omega_x C + \omega_x \frac{g_m \tau_F}{n^2} = 0 \Leftrightarrow \omega_x = \left[L \left[C + \frac{g_m \tau_F}{n^2} \right] \right]^{-\frac{1}{2}} . \quad (3.18)$$

Using (3.17) in (3.18) gives

$$\omega_x \leq \left[L \left[C + \frac{\tau_F}{nR\eta} \right] \right]^{-\frac{1}{2}} . \quad (3.19)$$

By comparing (3.19) to (3.12), we note that $\omega_x \leq \omega_z$ for this circuit.

We now determine the natural frequencies of the circuit. From either the expression $1 - T(s) = 0$ or $Y_a(s) + Y_r(s) = 0$, we obtain the following characteristic equation

$$s^2 L \left[C + \frac{g_m \tau_F}{n^2} \right] + sL \left[\frac{1}{R} - \frac{g_m \eta}{n} \right] + 1 = 0. \quad (3.20)$$

Assume that the natural frequencies are complex conjugate, i.e., $P_{1,2} = \alpha \pm j\beta$. We can show that

$$\alpha = \frac{1}{2} \left[\frac{g_m \eta}{n} - \frac{1}{R} \right] \left[C + \frac{g_m \tau_F}{n^2} \right]^{-1}$$

$$\beta = \left\{ \left[L \left[C + \frac{g_m \tau_F}{n^2} \right] \right]^{-1} - \left[\frac{1}{2} \left[\frac{g_m \eta}{n} - \frac{1}{R} \right] \left[C + \frac{g_m \tau_F}{n^2} \right]^{-1} \right]^2 \right\}^{\frac{1}{2}}.$$

The natural frequencies are in the RHP if

$$\alpha \geq 0 \Leftrightarrow g_m \geq \frac{n}{R} \frac{1}{\eta}. \quad (3.21)$$

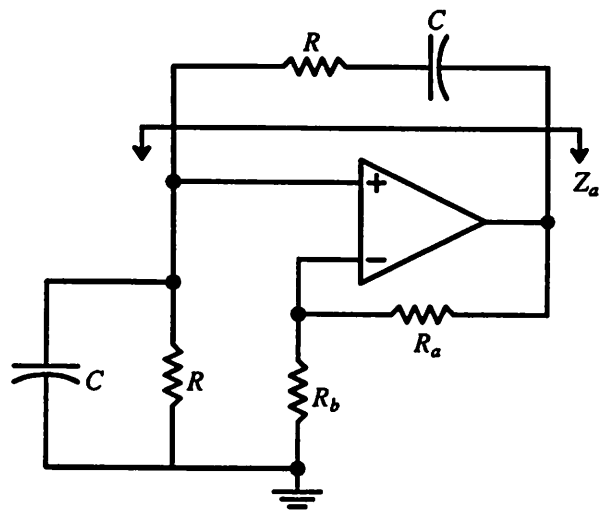
Note that (3.17) and (3.21) give the same requirement for quantity g_m , and thus confirm the validity of the start-up condition (3.4) in this circuit. If $g_m \approx \frac{n}{R} \frac{1}{\eta}$, the quantity α is approximately equal to zero.

Under this condition the natural frequencies lie close to the $j\omega$ axis and are referred to as high-Q natural frequencies. It is interesting to note that

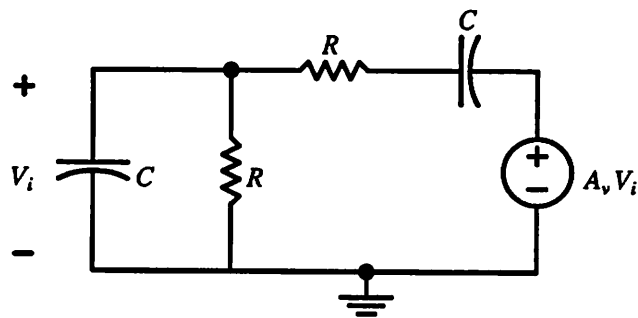
$$\omega_x \approx \left[L \left[C + \frac{\tau_F}{nR\eta} \right] \right]^{-\frac{1}{2}} = \omega_z.$$

The above analysis on the transformer-coupled oscillator suggests the following.

- (a) The frequency ω_z that fulfills the feedback condition (3.1) is, in general, not equal to the frequency ω_x that fulfills the negative-resistance condition (3.3) or (3.4).
- (b) If the RHP natural frequencies in the oscillator are high-Q natural frequencies, the frequency ω_x is almost the same as the frequency ω_z . Under this condition, frequency ω_x can be used for estimating the oscillation frequency.



(a) Wien-Type Oscillator



(b) Simplified ac Equivalent Circuit

Figure 3.13

Another circuit from which we can draw the same conclusions as above is the Wien-type oscillator shown in Fig. 3.13(a). Figure 3.13(b) shows the simplified ac equivalent circuit where $A_v \approx 1 + \frac{R_a}{R_b}$. It

can be shown that

$$T(s) = A_v \frac{sRC}{(sRC)^2 + s(3RC) + 1}$$

$$Z_a(s) = (1 - A_v) \frac{R}{1 + sRC}$$

$$Z_r(s) = R + \frac{1}{sC}$$

$$\omega_z = \frac{1}{RC}$$

$$\omega_x = \frac{1}{RC\sqrt{A_v - 2}}.$$

Assuming that the natural frequencies are complex conjugates, we can show that

$$P_{1,2} = \frac{A_v - 3}{2RC} \pm j \left[\left(\frac{1}{RC} \right)^2 - \left(\frac{A_v - 3}{2RC} \right)^2 \right]^{\frac{1}{2}}.$$

If $A_v \approx 3$, the natural frequencies lie close to the $j\omega$ axis. Again, we observe that

$$\omega_x \approx \frac{1}{RC} = \omega_z.$$

3.3. Large-Signal Analysis

When growing transients are large enough that the nonlinearities in the active devices become important, linear analysis is no longer valid. An oscillator must then be analyzed using nonlinear analysis. While linear analysis is used for studying the instability of the circuit and for predicting the oscillation frequency, nonlinear analysis is used for predicting the amplitude of oscillation and the output power level of the oscillator. Furthermore, nonlinear analysis is also used to predict the harmonic distortion in the output signal and the spectral purity of the output signal.

Nonlinear oscillator analysis is complex even when the effects of parasitic nonlinear charge-storage elements in the active devices can be neglected. Usually a nonlinear oscillator analysis starts with the assumption that the steady-state signal is near-sinusoidal and then proceeds to predict the amplitude of oscillation. One such analysis is based on the modified Bessel function for analyzing the Si bipolar Colpitts oscillator [Fre78, Mey89, Ped89]. Another analysis relies on computer simulation to generate a set of curves versus normalized design parameters for analyzing the MOS crystal Pierce oscillator [Mey80]. This dissertation studies the steady-state oscillator behavior through use of a general near-sinusoidal analysis by Kurokawa [Kur69].

The Kurokawa method is based on the negative-resistance model. It implicitly uses the concept of the *describing function* [Azz66] to represent the nonlinearity of the active circuit by an approximate linear transfer function. For a multi-port nonlinear circuit, the describing function is usually defined as

the ratio of the phasor representing the fundamental component of the output to the phasor representing the sinusoidal input. For a one-port nonlinear circuit, the describing function is similarly defined with the input and the output being either the port current or port voltage. Note that even though the input is sinusoidal, the output may not be because of the nonlinearity. For the Kurokawa analysis to be valid in a negative-resistance oscillator, either the current through or the voltage across the active circuit must be sinusoidal or near-sinusoidal in the steady state. If there is a well-defined near-sinusoidal oscillation in the steady state and furthermore, the current is near-sinusoidal, Kurokawa showed that the following *oscillation condition* holds

$$R_a^{(1)}(\omega_o, A_o) + R_r(\omega_o) = 0 \quad 3.22(a)$$

$$X_a^{(1)}(\omega_o, A_o) + X_r(\omega_o) = 0. \quad 3.22(b)$$

In 3.22(a) and 3.22(b), the resonant impedance is assumed independent of signal amplitude while the active impedance is dependent on both the signal amplitude and frequency. Quantities ω_o and A_o are the frequency and amplitude of oscillation, respectively. The superscript (1) is used to emphasize that the active impedance is evaluated at the oscillation frequency (fundamental frequency). It can be shown that 3.22(a) and 3.22(b) correspond to the conservation of real and complex energy, respectively [Hac65]. If, instead, the voltage is near-sinusoidal, the dual oscillation condition is

$$G_a^{(1)}(\omega_o, A_o) + G_r(\omega_o) = 0 \quad 3.23(a)$$

$$B_a^{(1)}(\omega_o, A_o) + B_r(\omega_o) = 0. \quad 3.23(b)$$

In Chapter 4 we use the Kurokawa analysis to predict the steady-state responses of a Van der Pol's oscillator and a microwave oscillator.

3.4. Stability Analyses

Conditions for frequency and amplitude stability in negative-resistance oscillators are derived in this section.

3.4.1. Frequency-Stability Analysis

In most oscillator applications, it is important that the oscillation frequency remains constant when subject to variations in nonlinear circuit elements. In a high-frequency oscillator, this requirement is more critical because multiple signal-dependent nonlinear capacitors in the active circuits can cause the oscillation frequency to drift significantly. The degree to which an oscillator can maintain a constant frequency is referred to as the *frequency stability*. We now derive a general expression for frequency stability in negative-resistance oscillators. The expression is based on the oscillation condition (3.22) and can be similarly derived using the oscillation condition (3.23).

Recall that if the active and resonant circuits are represented by impedances $Z_a^{(1)}$ and Z_r , respectively, the following oscillation condition holds

$$X_a^{(1)}(\omega_o, A_o) + X_r(\omega_o) = 0. \quad (3.24)$$

Now suppose the active reactance is changed by some δX . The oscillation frequency ω_o must consequently be adjusted by a $\delta\omega$ in order to maintain equality in the above equation. That is,

$$X_a^{(1)}(\omega_o + \delta\omega, A_o) + X_r(\omega_o + \delta\omega) + \delta X(\omega_o + \delta\omega, A_o) = 0. \quad (3.25)$$

The oscillator is frequency stable if $\delta\omega$ is small with respect to the frequency ω_o . An expression for $\delta\omega$ can be derived by using the Taylor expansion about ω_o in (3.25). Keeping the first two terms of the expansion yields

$$X_a^{(1)}(\omega_o, A_o) + X_r(\omega_o) + \delta X(\omega_o, A_o) + \left[\frac{\partial X_a^{(1)}}{\partial \omega} + \frac{\partial X_r}{\partial \omega} + \frac{\partial \delta X}{\partial \omega} \right]_{\omega = \omega_o, A = A_o} \delta\omega \approx 0. \quad (3.26)$$

Combining (3.24) and (3.26) yields

$$\delta\omega = -\delta X(\omega_o, A_o) \left[\frac{\partial X_a^{(1)}}{\partial \omega} + \frac{\partial X_r}{\partial \omega} + \frac{\partial \delta X}{\partial \omega} \right]_{\omega = \omega_o, A = A_o}^{-1}. \quad (3.27)$$

From (3.27), $\delta\omega$ is small if $\delta X(\omega_o, A_o)$ is small or the total reactance change with respect to frequency about ω_o is large. Evaluating (3.27) can be tedious since all the calculations must be done using large-signal quantities. If the oscillation frequency can be accurately predicted by the linear quantity ω_x , (3.27)

can be approximated by

$$\delta\omega = -\delta X(\omega_x) \left[\frac{\partial X_a}{\partial \omega} + \frac{\partial X_r}{\partial \omega} + \frac{\partial \delta X}{\partial \omega} \right]_{\omega=\omega_x}^{-1} \quad (3.28)$$

3.4.2. Amplitude-Stability Analysis

Assume that an oscillator has reached its steady-state oscillation. Fluctuations in power supply or electronic noise can perturb the oscillating signal, possibly resulting in permanent amplitude instability. An oscillator is *amplitude stable* if any transient perturbation in the oscillation signal decays with time. We now derive a condition that guarantees amplitude stability in negative-resistance oscillators.

Early works by Ford and Edson applied the concept of the complex-frequency plane to analyze the perturbed behavior of the oscillating signal [For46, Eds53]. A more general approach is the *perturbation method* [Kur69] which assumes that the phase and amplitude change due to disturbances vary slowly with time. With further assumptions that the active circuit is independent of frequency and the current through it is near-sinusoidal in the steady state, Kurokawa showed that the following condition must be satisfied in order to ensure amplitude stability in a negative-resistance oscillator

$$\frac{\partial R_a^{(1)}}{\partial A} \frac{\partial X_r}{\partial \omega} - \frac{\partial X_a^{(1)}}{\partial A} \frac{\partial R_r}{\partial \omega} > 0. \quad (3.29)$$

In the above expression, all the partial derivatives are evaluated at the steady-state values ω_0 and A_0 . Condition (3.29) is valid only if the active circuit is frequency independent. For oscillators operating over a wide frequency range and for microwave oscillator circuits, however, the dependency of the active circuit on frequency must be considered. An extension of the work of Kurokawa yields the following general condition for amplitude stability

$$\frac{\partial R_a^{(1)}}{\partial A} \left\{ \frac{\partial X_a^{(1)}}{\partial \omega} + \frac{\partial X_r}{\partial \omega} \right\} - \frac{\partial X_a^{(1)}}{\partial A} \left\{ \frac{\partial R_a^{(1)}}{\partial \omega} + \frac{\partial R_r}{\partial \omega} \right\} > 0. \quad (3.30)$$

If the voltage instead of the current is near-sinusoidal in the steady state, the dual condition is

$$\frac{\partial G_a^{(1)}}{\partial A} \left\{ \frac{\partial B_a^{(1)}}{\partial \omega} + \frac{\partial B_r}{\partial \omega} \right\} - \frac{\partial B_a^{(1)}}{\partial A} \left\{ \frac{\partial G_a^{(1)}}{\partial \omega} + \frac{\partial G_r}{\partial \omega} \right\} > 0. \quad (3.31)$$

Equations (3.30) and (3.31) are used in the design and analysis of a microwave oscillator circuit in Chapter 4.

3.5. Summary

Investigation on the conventional start-up conditions has revealed that they are not always valid and can provide misleading results. Special attention should be given when the start-up condition

$$\text{Ph} \{ T(\omega_x) \} = 0 \quad \text{Mag} \{ T(\omega_x) \} > 1$$

holds at multiple frequencies ω_x , or when the reactive/susceptive function of the start-up conditions

$$R_a(\omega_x) + R_r(\omega_x) < 0 \quad X_a(\omega_x) + X_r(\omega_x) = 0$$

and

$$G_a(\omega_x) + G_r(\omega_x) < 0 \quad B_a(\omega_x) + B_r(\omega_x) = 0$$

crosses the zero point at multiples frequencies ω_x . The Nyquist and root-locus analyses are powerful techniques for studying the linear behavior of oscillator circuits. The root-locus analysis is also useful for analyzing the multi-oscillation phenomenon. Regarding the frequency of oscillation, the frequency ω_x is a good estimation given that the circuit has high-Q natural frequencies.

Chapter 4 - Oscillator Design Methodology

4.1. Introduction

It has been shown in Chapter 3 that conventional oscillator design techniques may not be applicable in the design of microwave oscillator circuits. In particular, the conventional start-up conditions are not always sufficient for predicting the existence of an oscillatory behavior in the circuit. The multi-oscillation phenomenon has been studied, and the conditions for frequency and amplitude stability in negative-resistance oscillators have been derived. In this chapter we study the interaction between oscillator circuit components, and then explore a design methodology for microwave oscillators. The negative-resistance model is utilized in the design since it is simpler than the feedback model. The design methodology should achieve the following objective: given an active circuit, an LC tuned circuit is systematically chosen such that the resultant oscillator circuit achieves a reliable oscillation build-up and has a single predictable frequency of oscillation in the steady state. The results obtained from this study are then applied to the design and analysis of a widely-used but poorly-characterized microwave oscillator configuration. To confirm the theoretical analysis and to demonstrate the feasibility of silicon integration, a monolithic implementation of this circuit is described.

4.2. Systematic Design Methodology

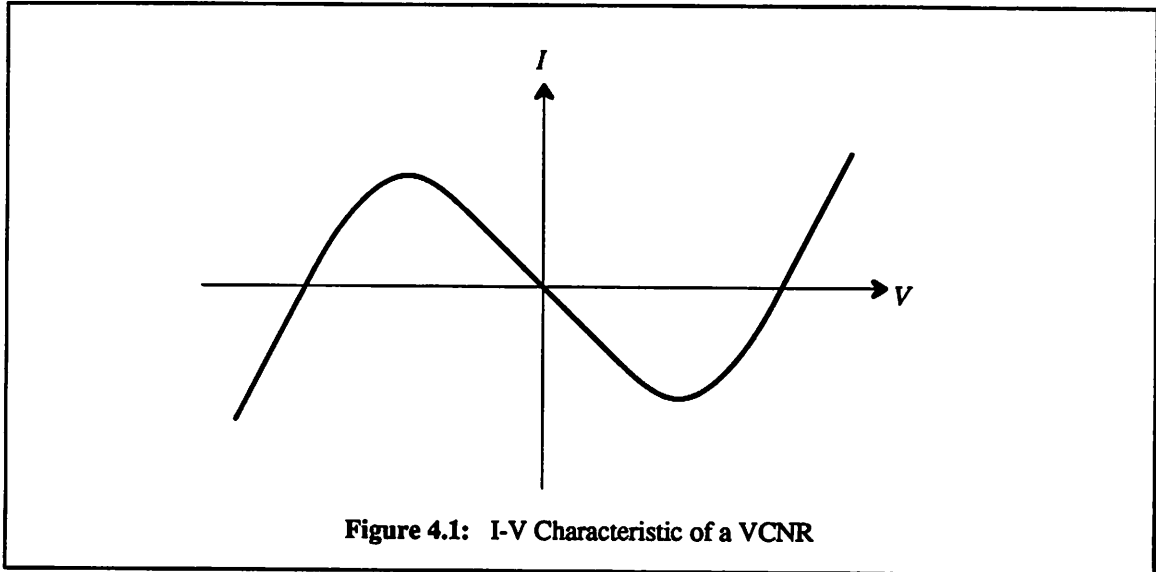
It is useful to distinguish two types of active circuits since as is shown subsequently, the design methodology for one is quite different from the other.

The first group of active circuits consists of one-port devices or circuits whose I-V characteristics contain a negative-resistance region. Examples of such active circuits are the tunnel diodes, avalanche diodes [Gib73], loop-coupled bistable circuits, negative resistors constructed from op-amp circuits [Chu87], and inductive transformer-coupled configurations [Mey89, Ped89]. Henceforth, we use the abbreviation VCNR to denote a voltage-controlled negative resistor and ICNR to denote a current-controlled negative resistor. An active circuit is a VCNR if the port current of the circuit is a single-valued function of the port voltage.

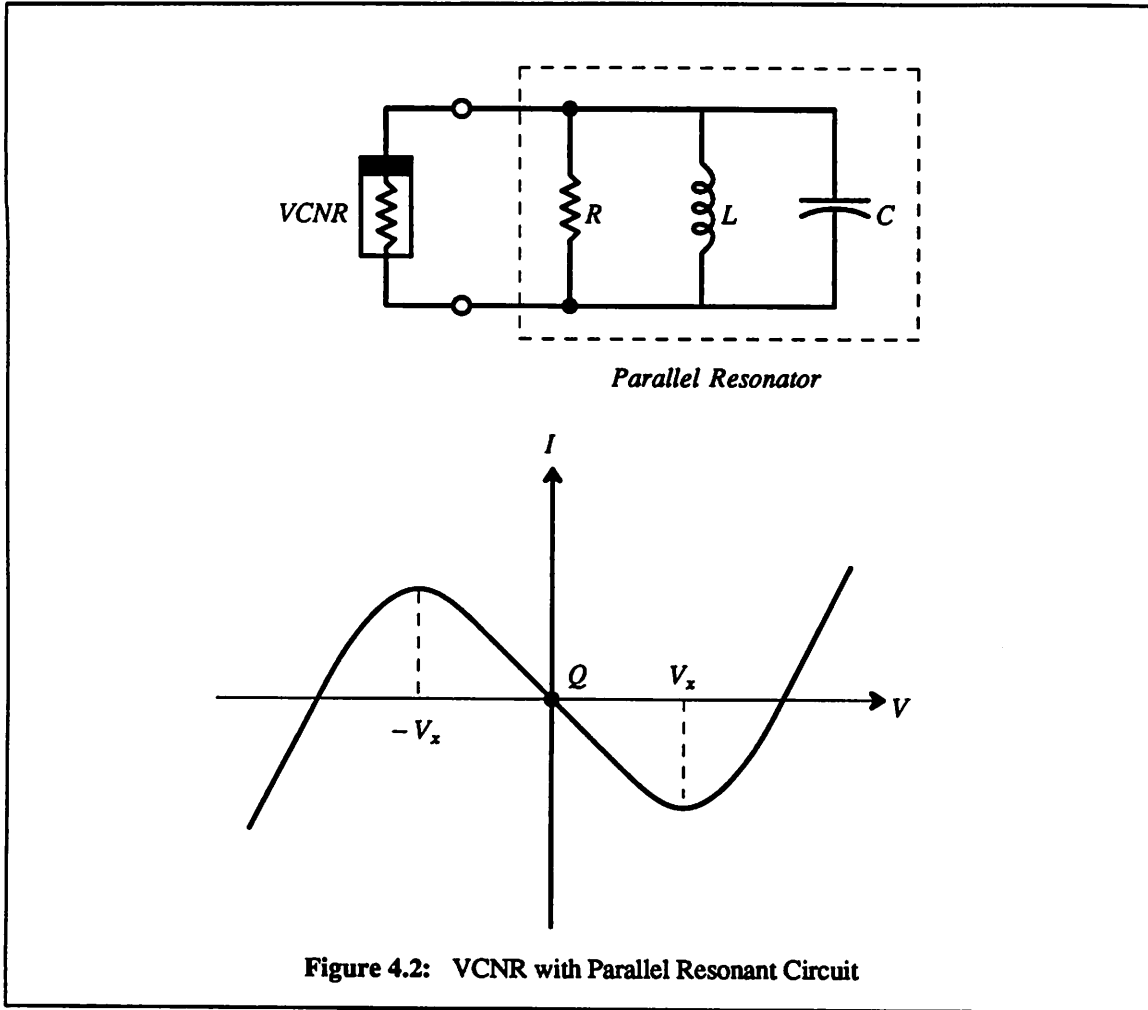
The second group of active circuits do not possess a negative-resistance region in their I-V characteristics but, instead, depend on LC elements (often connected in feedback configurations) in order to produce a small-signal negative resistance about the operating point of the circuit. Examples of such circuits are the Colpitts, Pierce, and Hartley oscillators [Fre78].

4.2.1. Voltage/Current-Controlled Negative Resistors

In this section we present a detailed approach on the selection of a proper LC tuned circuit for a VCNR or an ICNR active circuit. For clarity in the analysis, we consider only VCNR active circuits. Appropriate conclusions can then be drawn for ICNR active circuits through use of the *principle of duality* [Chu87].



The I-V characteristic of a VCNR is shown in Fig. 4.1. Note that the current is a single-valued function of the voltage. When a VCNR is used in conjunction with a parallel RLC tank circuit, we obtain the well-known Van der Pol oscillator shown in Fig. 4.2 [Pol34]. Upon superimposing the I-V characteristic of the resonant circuit (a short circuit) with the characteristic of the VCNR, we observe that the circuit has a unique operating point Q inside the negative-resistance region of the VCNR. Denote the negative conductance of the VCNR by G_a (about the operating point Q) and define $G = \frac{1}{R}$. We can show that the circuit has the following characteristic equation



$$s^2 + s \frac{G_a + G}{C} + \frac{1}{LC} = 0. \quad (4.1)$$

The natural frequencies derived from (4.1) are

$$P_{1,2} = -\frac{G_a + G}{2C} + \left[\left(\frac{G_a + G}{2C} \right)^2 - \left(\frac{1}{LC} \right) \right]^{\frac{1}{2}}. \quad (4.2)$$

If $\left(\frac{G_a + G}{2C} \right)^2 < \left(\frac{1}{LC} \right)$ or equivalently $Q_p \equiv \left| \frac{1}{G_a + G} \right| \sqrt{\frac{C}{L}} > \frac{1}{2}$, the natural frequencies are complex conjugate. Furthermore, they are in the RHP if

$$G_a + G < 0.$$

We can also derive the above instability condition from the start-up condition (3.4) which states

$$G_a(\omega_x) + G_r(\omega_x) < 0 \quad \text{and} \quad B_a(\omega_x) + B_r(\omega_x) = 0.$$

For the circuit of Fig. 4.2, $G_a(\omega_x) = G_a$, $G_r(\omega_x) = G$, $B_a(\omega_x) = 0$, and $B_r(\omega_x) = \frac{-1}{\omega_x L} + \omega_x C$. If the VCNR is purely conductive as assumed (valid at low frequencies), the frequency ω_x at which the total susceptance equals zero is simply the resonant frequency of the parallel LC tank

$$\omega_x = \left[\frac{1}{LC} \right]^{\frac{1}{2}}. \quad (4.3)$$

Due to the distortion in the VCNR, we expect the steady-state oscillation frequency to be slightly less than the frequency ω_x given in (4.3) [Gro33].

The above analysis is concerned with the linear behavior for the circuit of Fig. 4.2. We now investigate its steady-state behavior by using the Kurokawa analysis presented in Chapter 3. To this end, we assume that the VCNR can be modeled by the following simple cubic equation which is also referred to as the Van der Pol's approximation

$$I = aV + bV^3. \quad (4.4)$$

Quantity a ($= G_a$) is the negative conductance about the origin. Quantity b can be derived to be

$$b = -\frac{a}{3V_x^2} \quad (4.5)$$

where V_x is the voltage at which the current reaches the minimum value as shown in Fig. 4.2. We assume that the steady-state voltage across the VCNR is near-sinusoidal and can be represented by

$$V(t) \approx V_o \cos(\omega_o t) \quad (4.6)$$

where $\omega_o \approx \left[\frac{1}{LC} \right]^{\frac{1}{2}} = \omega_x$. Substituting (4.6) into (4.4) yields

$$I(t) = (aV_o + \frac{3}{4}bV_o^3) \cos(\omega_o t) + \frac{1}{4}bV_o^3 \cos(3\omega_o t).$$

The conductance evaluated at the fundamental frequency is

$$G_a^{(1)} = \frac{aV_o + \frac{3}{4}bV_o^3}{V_o} = a + \frac{3}{4}bV_o^2.$$

From the steady-state condition (3.23) in Chapter 3, the circuit is in steady state if

$$G_a^{(1)} + G = 0 \Rightarrow a + \frac{3}{4}bV_o^2 + G = 0$$

where $G (= \frac{1}{R})$ is the linear conductance of the resonant circuit. The amplitude of oscillation is

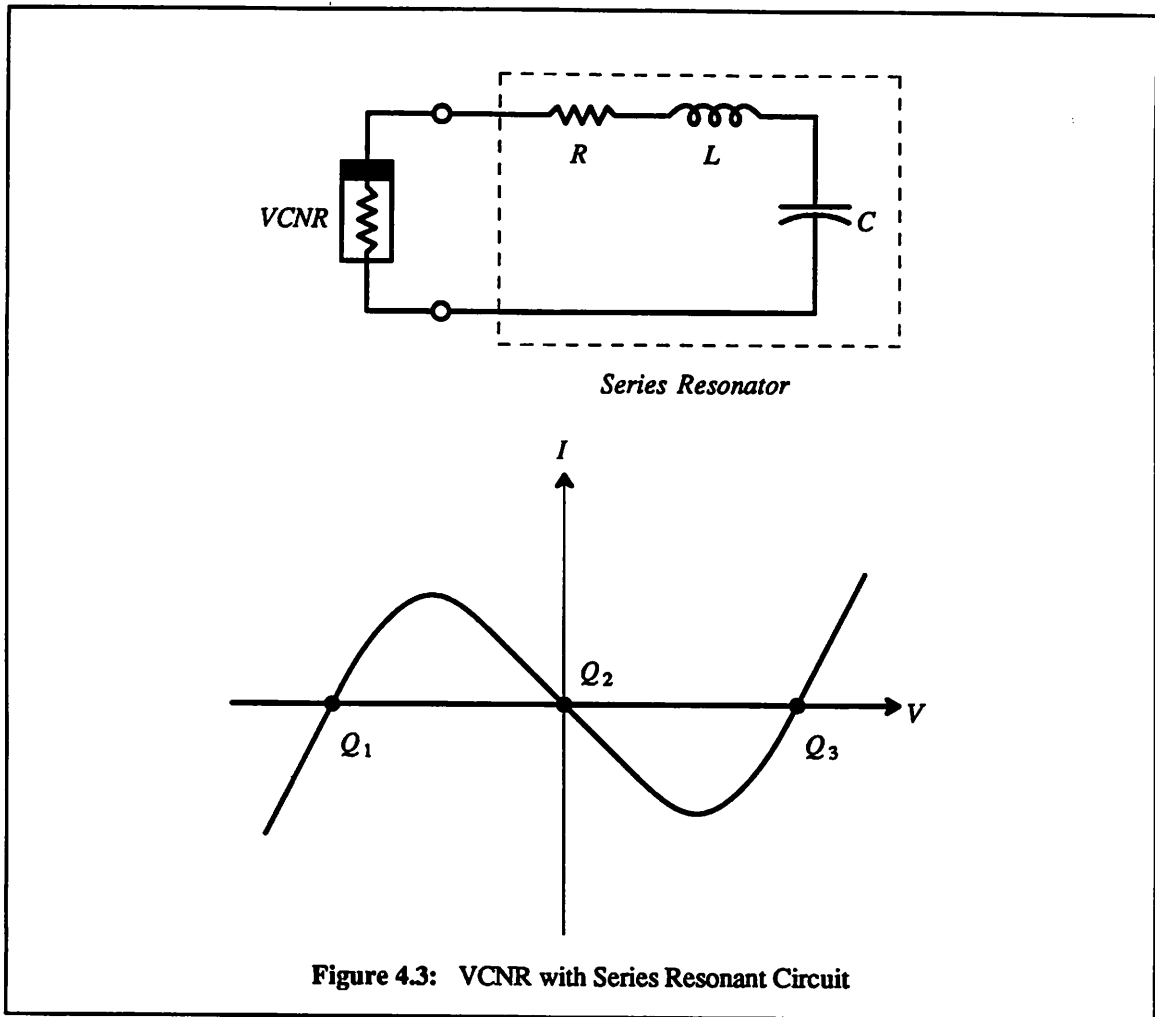
$$V_o = \sqrt{-\frac{4}{3} \frac{a+G}{b}}. \quad (4.7)$$

The result given by (4.7) agrees exactly with that obtained from more complicated methods by Van der Pol and Edson [Pol34, Eds53]. These methods determine the amplitude of oscillation by solving the second-order differential equation governing the behavior of this circuit.

The analysis so far assumes that the VCNR is purely conductive. At high frequencies, parasitic charge-storage elements associated with the VCNR become significant and cannot be neglected. As an approximation, the parasitic elements can be modeled by a shunt capacitor across the VCNR. By lumping this parasitic capacitor into the capacitor C of the resonant circuit in Fig. 4.2, the analysis presented above may still hold.

What if a VCNR is connected to a series RLC tank circuit as shown in Fig. 4.3? Upon superimposing the I-V characteristic of the series RLC circuit (an open circuit) with the characteristic of the VCNR, we observe that the circuit now has three possible operating points Q_1 , Q_2 , and Q_3 . Since there is no guarantee that the circuit will operate in the negative-resistance region, this circuit cannot produce a well-defined oscillation build-up. Fortunately, the VCNR may be forced into the negative-resistance region with a shunt inductor L_p as shown in Fig. 4.4. In order to study the transient response and to determine whether this circuit can produce a sinusoidal oscillation, we study the location of the natural frequencies from the root loci of the circuit.

Let R_p denote the small-signal negative resistance of the VCNR about the operating point Q . The root locus as a function of L_p can be constructed from the following characteristic equation



$$s^3 \frac{L_p}{R_p} LC + s^2 \left[\frac{L_p}{R_p} RC + (L_p + L) C \right] + s \left[\frac{L_p}{R_p} + RC \right] + 1 = 0. \quad (4.8)$$

For small values of L_p , it can be shown that (4.8) has a pair of LHP complex-conjugate natural frequencies due to the series resonant circuit, and one RHP real natural frequency due to L_p . As values of L_p get larger, (4.8) reduces to

$$s \left[s^2 LC + s(R_p + R) C + 1 \right] \approx 0. \quad (4.9)$$

Equation (4.9) has one natural frequency at the origin and two other natural frequencies from the expression inside the brackets. Define

$$Q_s = \frac{1}{|R_p + R|} \sqrt{\frac{L}{C}}. \quad (4.10)$$

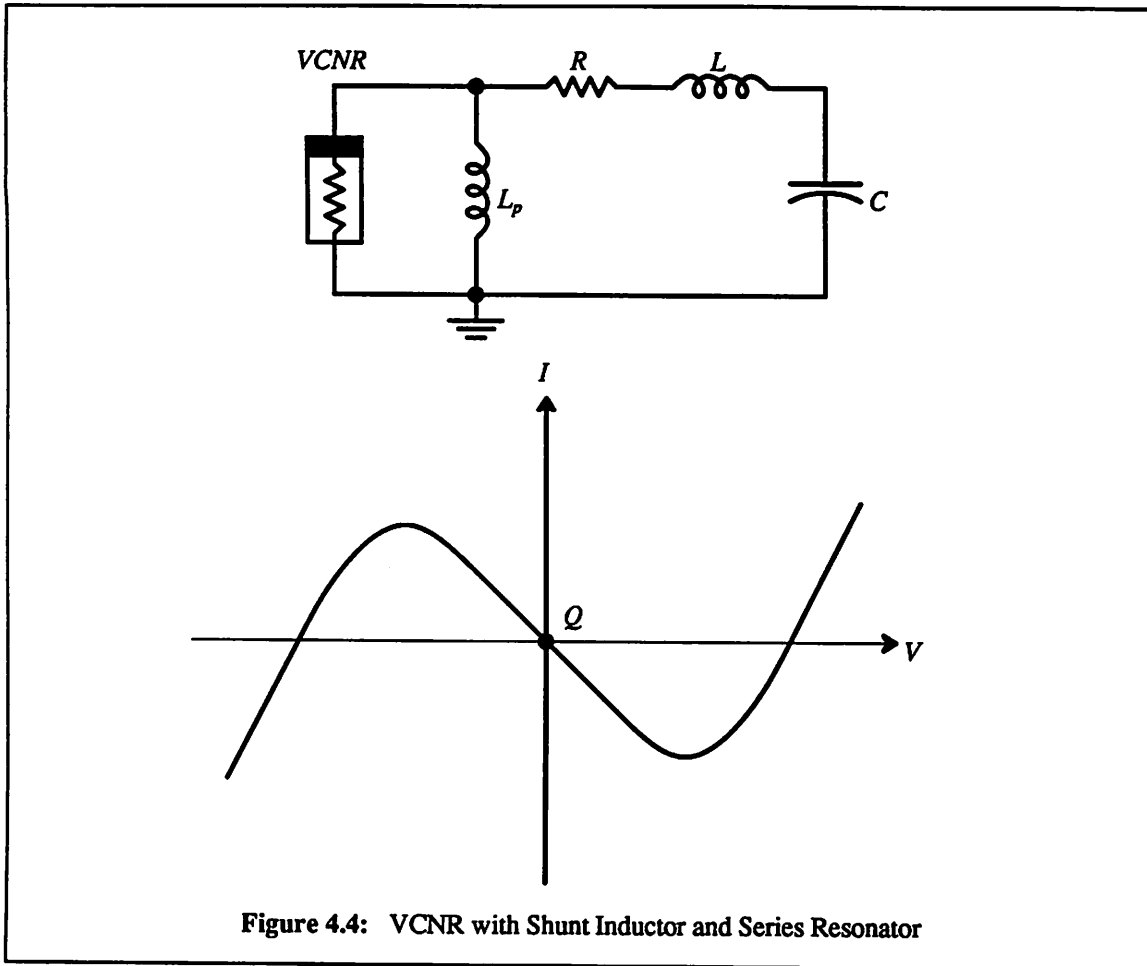
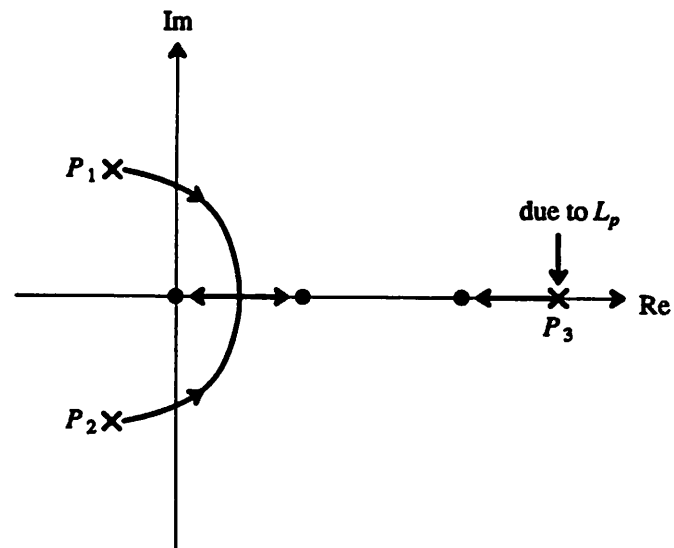
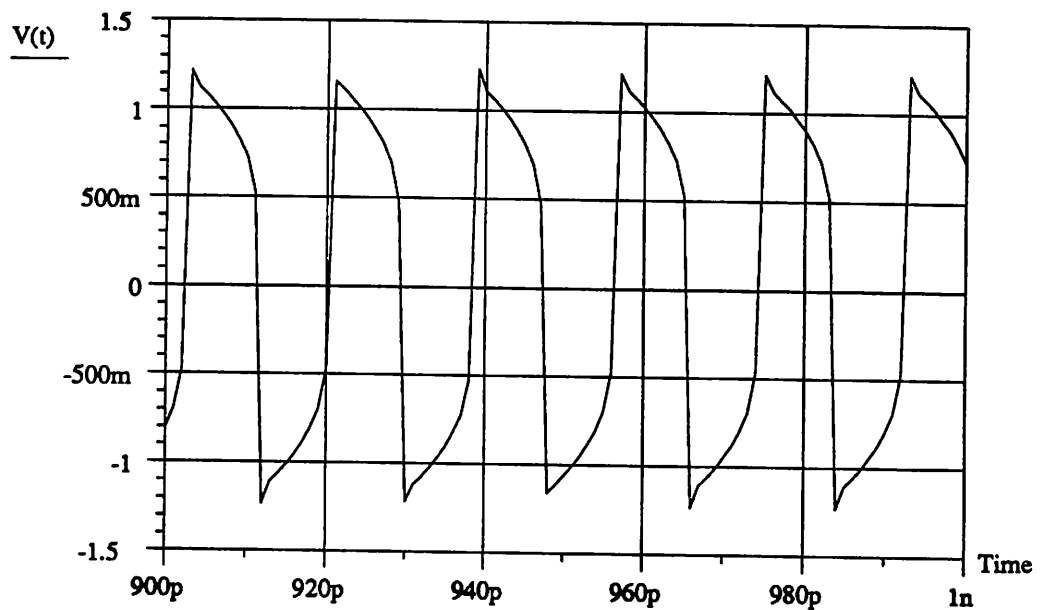


Figure 4.4: VCNR with Shunt Inductor and Series Resonator

If $Q_s < \frac{1}{2}$ (low-Q case), we expect the natural frequencies derived from (4.9) to lie on the real axis of the complex-frequency plane. The associated root locus is given in Fig. 4.5(a). It reveals that there exists 3 natural frequencies in the RHP, of which the one due to L_p appears *dominant* since it has the fastest build-up rate. In response to noise impulses, the circuit produces a growing exponential signal and results into a relaxation-type oscillation as shown in Fig. 4.5(b). On the other hand if $Q_s > \frac{1}{2}$ (high-Q case), we expect the two natural frequencies derived from the expression inside the bracket of (4.9) to be complex conjugate. The associated root locus is given in Fig. 4.6(a). This locus suggests that we can select a set of circuit parameters that yield a pair of RHP natural frequencies $P_{1,2} = \alpha_1 \pm j\beta_1$, and one non-dominant RHP real natural frequency $P_3 = \alpha_3$ where $\alpha_3 < \alpha_1$. With this selection, we hope to achieve a sinusoidal signal build-up of the form



(a) Root Locus for the Circuit of Fig. 4.4 (Low-Q Case)



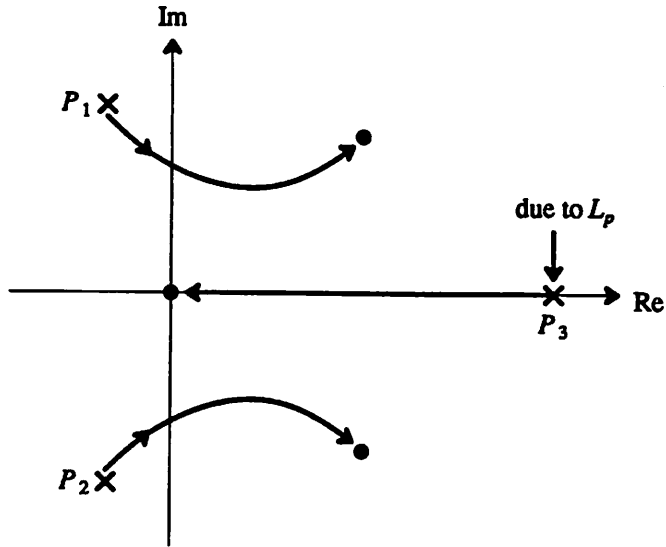
(b) Transient Response

Figure 4.5

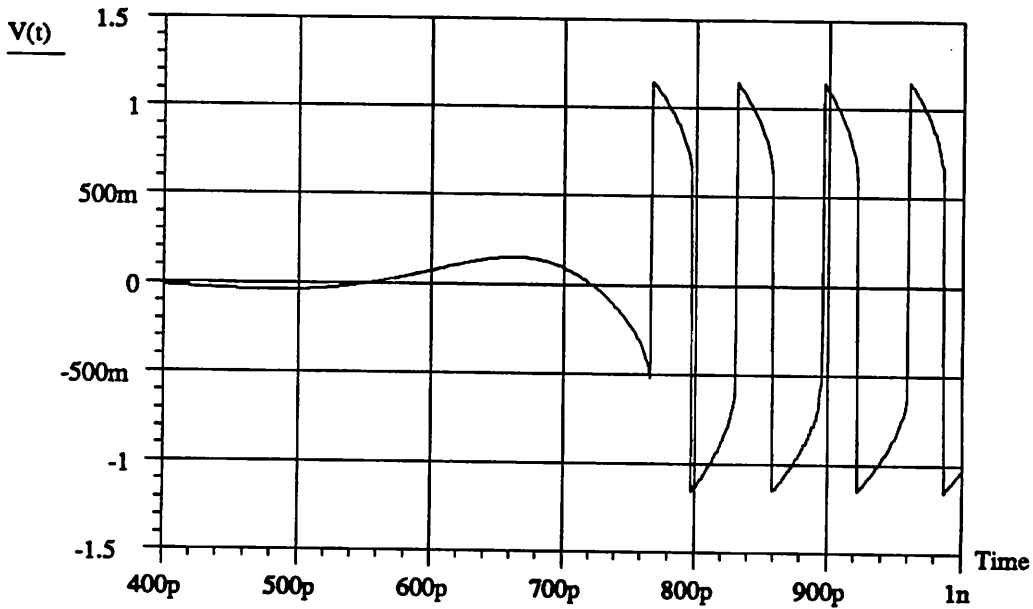
$$x(t) = K_1 e^{\alpha_1 t} \cos(\beta_1 t) + K_2 e^{\alpha_3 t}$$

and eventually a sinusoidal oscillation in the steady state. But as observed from the transient response of

one such circuit shown in Fig. 4.6(b), the signal starts out sinusoidally but then settles in a relaxation oscillation instead. This behavior is rather difficult to explain mathematically. At best the circuit of Fig. 4.4 can only function as a relaxation oscillator.



(a) Root Locus for the Circuit of Fig. 4.4 (High-Q Case)



(b) Transient Response

Figure 4.6

In conclusion, we have determined that the most appropriate LC resonant circuit for a VCNR that results in a well-behaved sinusoidal oscillator is the parallel RLC resonant circuit. From the *principle of duality*, we can conclude that a series RLC tuned circuit is most appropriate for an ICNR.

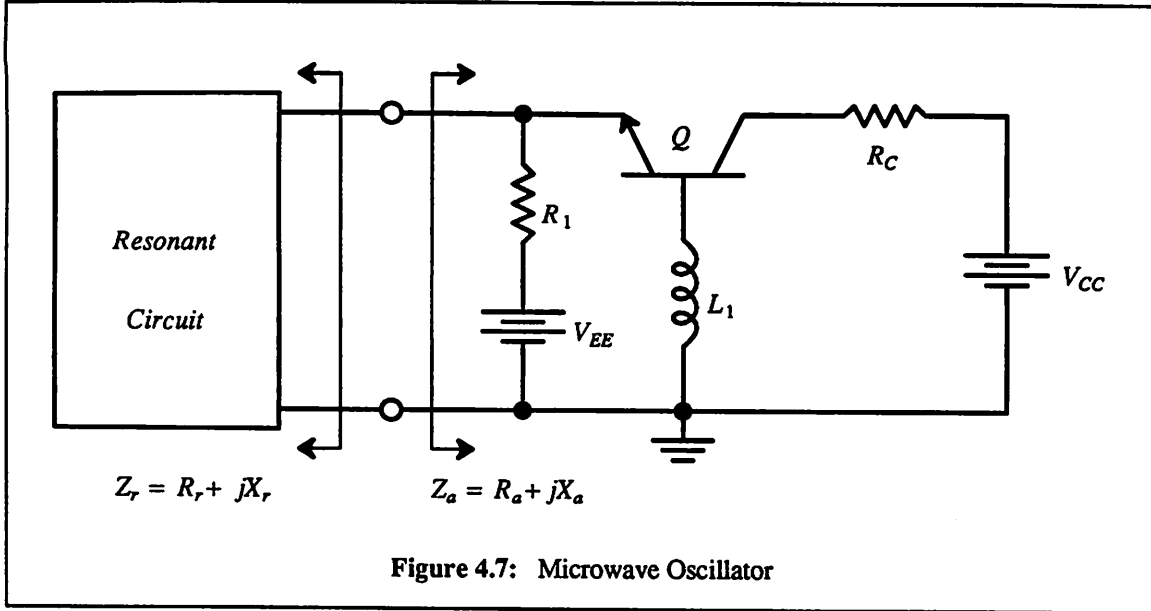
4.2.2. LC-Dependent Negative Resistors

In this section we derive a systematic design methodology for active circuits that do not possess a negative-resistance region in their I-V characteristics. As mentioned above, the Colpitts, Pierce, Hartley, and Clapp configurations among others belong to this group. Since an active circuit of this kind depends on energy-storage LC elements in order to produce a small-signal negative resistance, it is frequency dependent. That is, if the active circuit is represented by an equivalent impedance, the resistive component is negative only in a finite frequency band, referred to as the *negative-resistance band*. In addition to the negative resistive component, the active circuit also has a reactive component, either inductive or capacitive. The design methodology below is based on the negative-resistance model and involves the following three steps.

- (1) **Active-circuit characterization:** this step determines the negative-resistance band. Because no oscillation build-up is possible outside this band, the negative-resistance band must be designed to cover the frequency range of interest. Often this involves the selection of the appropriate LC elements and active devices.
- (2) **Resonant-circuit selection / verification:** this step selects a resonant circuit that together with the active circuit form a well-defined oscillator. The selection is based on the start-up condition (3.3) or (3.4), and should be confirmed with either the Nyquist or root-locus analysis for validity.
- (3) **Large-signal analysis:** this step is concerned with the amplitude and frequency of oscillation (steady-state behavior).

The above design methodology is now illustrated with a design example. The circuit under consideration, shown in Fig. 4.7, is a widely-used microwave oscillator configuration. One advantage of this configuration is that if the device capacitance C_{μ} of the transistor can be neglected (the only significant parasitic element across the base-collector junction), an output signal can be taken across the resistor R_C

without introducing a loading effect to the circuit. This is true since the collector-emitter terminal can be modeled by a current source. The function of the inductor L_1 is to produce a negative resistance.



For simplicity, we neglect the effects of R_1 , R_C , C_μ (internal base-collector capacitance), and C_{bx} (external base-collector capacitance). The active impedance can be shown to be

$$Z_a(s) = \frac{1 + sC_\pi r_b + s^2 L_1 C_\pi}{g_m \left(1 + s \frac{C_\pi}{g_m}\right)}. \quad (4.11)$$

By separating the active impedance into real and imaginary components, we obtain

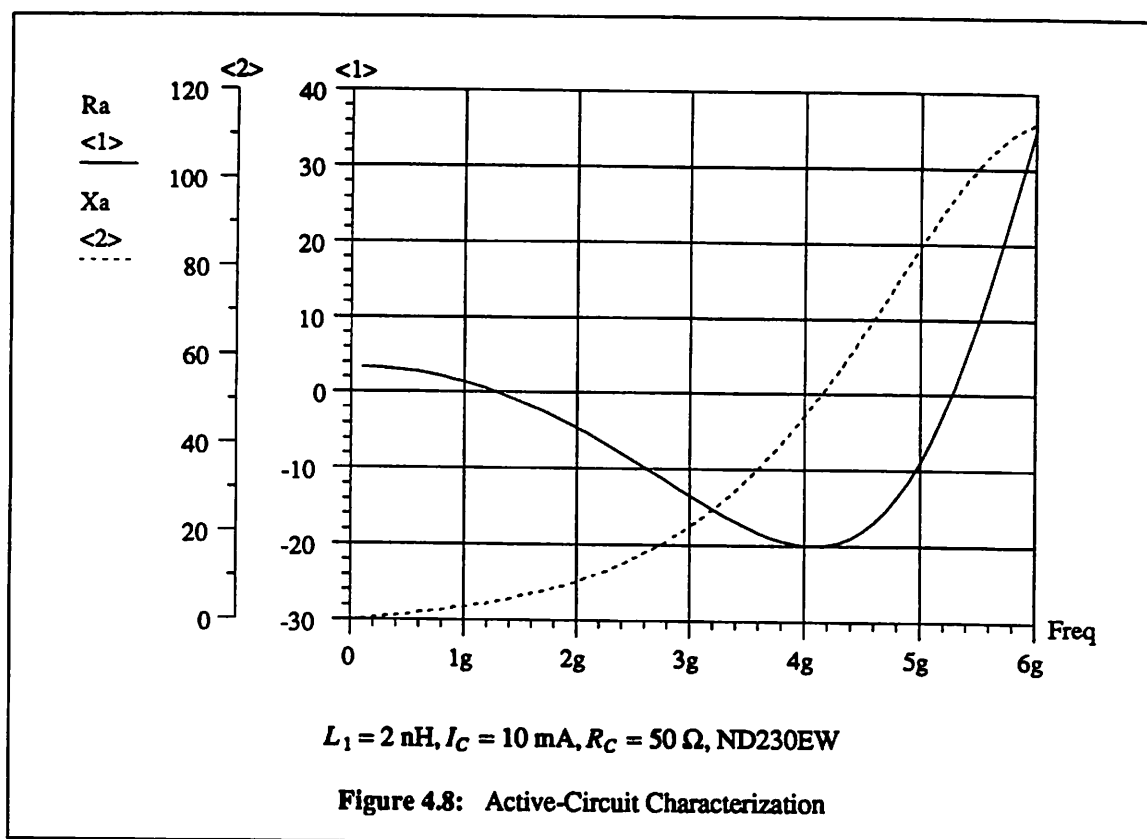
$$Z_a(\omega) \approx \frac{1}{g_m} \left[1 - \omega^2 L_1 C_\pi \right] + j\omega \frac{r_b C_\pi}{g_m}. \quad (4.12)$$

We note that the real component of (4.12) is frequency dependent and is negative if

$$\omega > \left[\frac{1}{L_1 C_\pi} \right]^{\frac{1}{2}}. \quad (4.13)$$

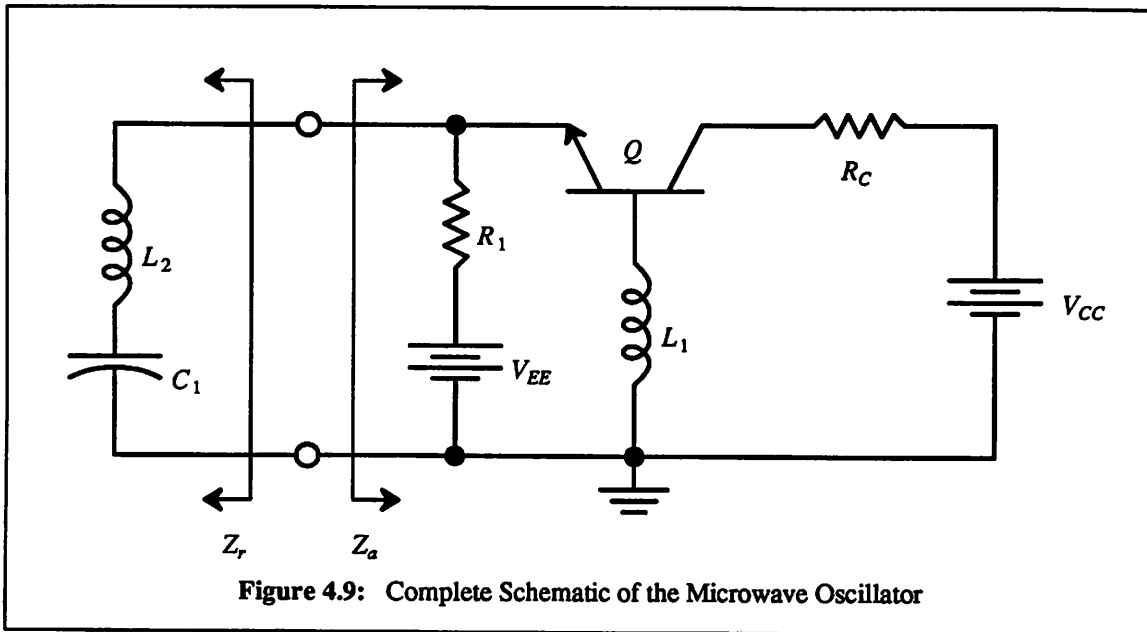
Since capacitor C_π is typically a few pico-Farads and inductor L_1 a few nano-Henries, (4.13) suggests that this circuit can perform well into the microwave range. As frequency increases, it is important to take into account the effects of C_μ and C_{bx} . The upper limit of this circuit's negative-resistance band

can be shown to be constrained by the smaller of the self-resonant frequency of the integrated inductor L_1 [Chapter 5] or the frequency $\left[L_1(C_{bx} + C_{\mu}) \right]^{-\frac{1}{2}}$. In Fig. 4.8, the simulated active impedance shows a negative-resistance band of about 4 GHz, extending from 1 GHz to 5 GHz. In addition to the negative resistance component, the active impedance also has an inductive reactance.



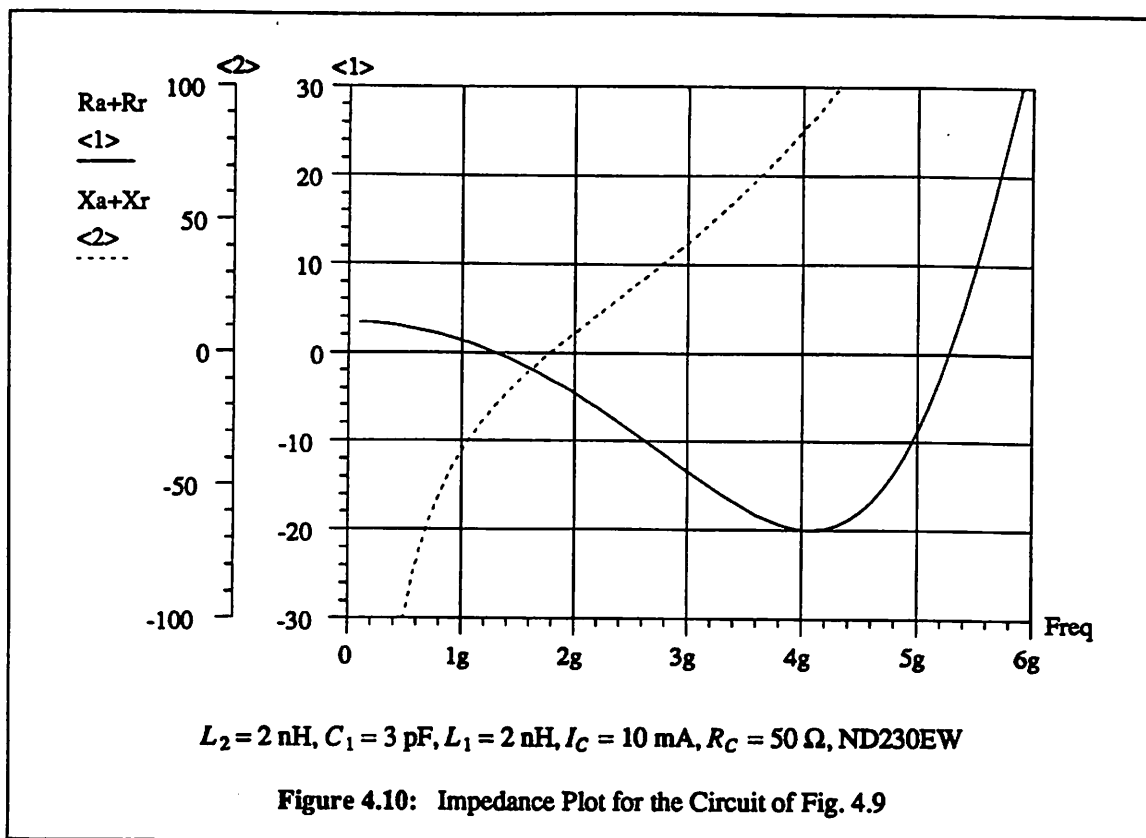
With the active circuit characterized, the second step is to determine a resonant circuit that together with the active circuit forms an oscillator. The objective is to select a resonant circuit such that the resultant circuit has only one pair of RHP complex-conjugate natural frequencies. The selection is based on the start-up condition for negative-resistance oscillators. Even though this condition may provide misleading results regarding the linear behavior of the circuit, it nevertheless provides us with a direction to go about selecting a resonant circuit. It is important to emphasize that this selection process should be confirmed with either Nyquist or root-locus analysis.

Since the reactance of the given active circuit is inductive, the resonant circuit must be capacitive so that we can tune out the reactive component at the frequency of interest. One resonant circuit could simply be a capacitor. If we want to minimize electronic noise and distortion content in the output signal, we can use either a high-Q parallel or series LC resonant circuit. The constraint here is that the resonant circuit must still be capacitive at the frequency of operation. In Fig. 4.9, a series LC resonant circuit is utilized since it does not affect the bias scheme of Fig. 4.7.



As multiple LC elements are used to form the resonant circuit, extreme care must be taken to ensure that the multi-oscillation phenomenon does not take place. There should be, therefore, only one frequency ω_x at which the start-up condition holds. This requirement can be satisfied if the total reactance plot is monotonic. Figure 4.10 shows the simulated impedance of the circuit. As a check for the above selection, the root-locus and Nyquist plots have been generated. The plots in Fig. 4.11 confirm the existence of a well-defined pair of RHP natural frequencies. Due to inductor L_2 , we observe that the circuit has a pair of high-Q natural frequencies. It has been observed in practice that any well-behaved sinusoidal oscillator possesses a pair of RHP complex-conjugate natural frequencies near the $j\omega$ axis.

Upon the completion of the first two steps, the linear behavior of the oscillator circuit is fully understood. While these steps are used for achieving a reliable oscillation build-up and for predicting the

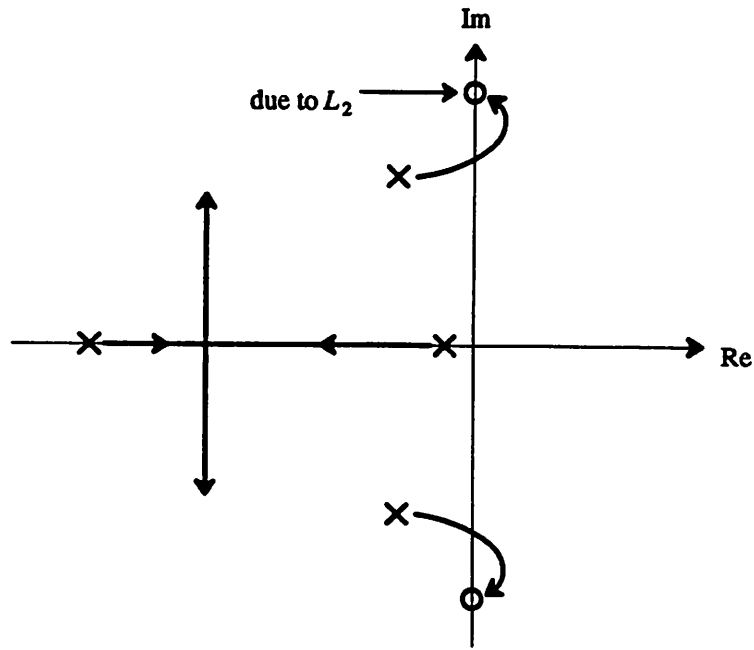


oscillation frequency, they are not valid for predicting the circuit's steady-state behavior. Nonlinear analysis must be used in order to predict the amplitude of oscillation and the output power level of the oscillator. Nonlinear analysis is usually very complicated due to various nonlinear elements in the circuit.

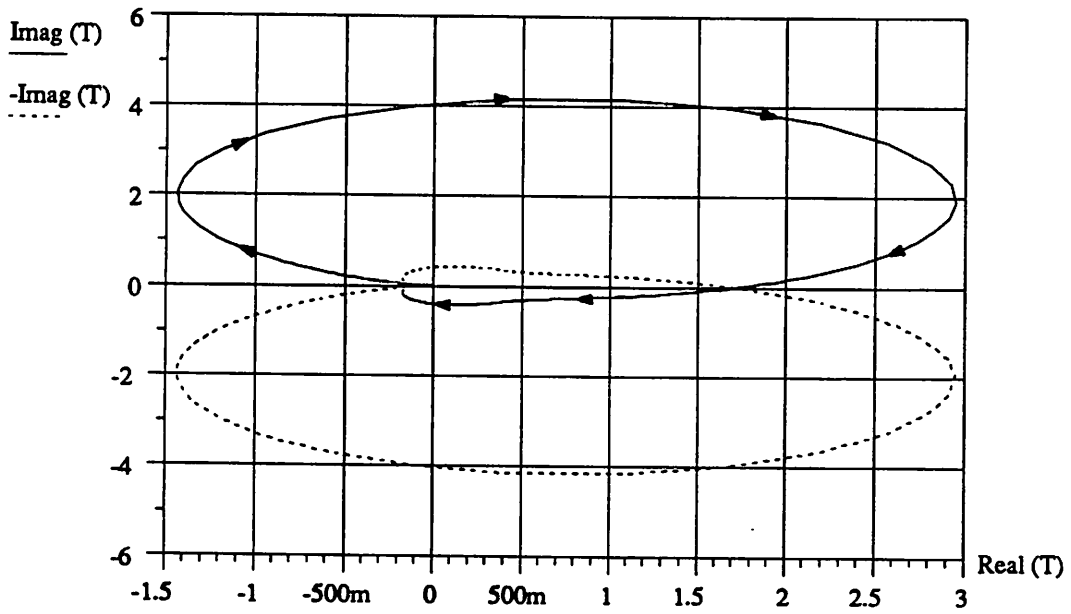
In the following paragraphs, the near-sinusoidal method proposed by Kurokawa is combined with the "normalized-parameters" method by Meyer [Mey80] for studying the steady-state behavior of this circuit. To this point, we assume that the steady-state current entering the active circuit is near-sinusoidal. From the large-signal equivalent circuit shown in Fig. 4.12 with the emitter of the bipolar transistor being defined as the datum node, the voltage across and the current entering the active circuit are respectively given by

$$V_a = L_1 \frac{dI_b}{dt} + r_b I_b + V_2 \quad (4.14)$$

$$I_a = I_c + I_b - I_Q. \quad (4.15)$$



(a) Root Locus



(b) Nyquist Diagram

Figure 4.11: Root Locus and Nyquist Diagram for the Circuit of Fig. 4.9

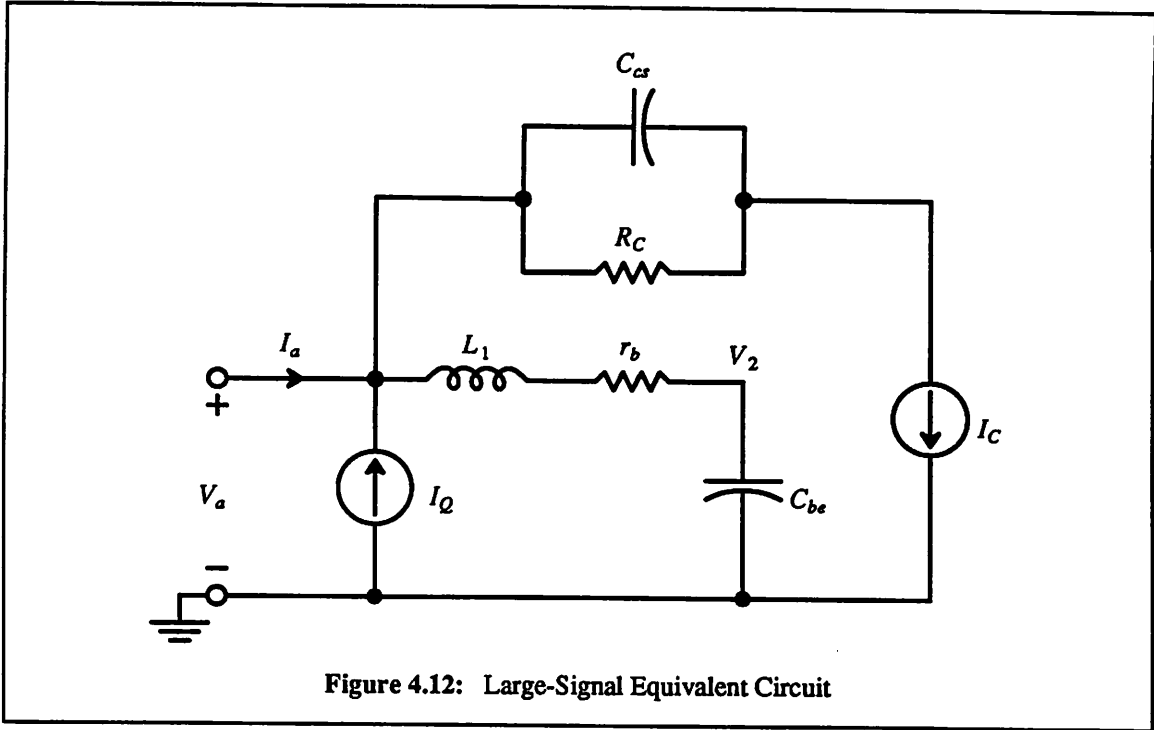


Figure 4.12: Large-Signal Equivalent Circuit

If the current across the base-collector junction is neglected, the base current I_b consists mainly of the diffusion and depletion current components through the base-emitter junction

$$I_b = \tau_{eff} \frac{dI_c}{dt} + C_{je} \frac{dV_2}{dt}.$$

The base-emitter junction voltage V_2 can be expressed in terms of I_c as

$$V_2 = \frac{kT}{q} \ln\left(\frac{I_c}{I_S}\right) = V_T \ln\left(\frac{I_c}{I_S}\right).$$

By the assumption that the current I_a is sinusoidal in the steady state, we can write $I_a = I_m \sin(\omega_o t)$. By normalizing time $t' = \omega_o t$ and the collector current $I_c' = I_c / I_Q$, (4.14) and (4.15) can be rewritten as

$$\begin{aligned} \frac{V_a}{V_T} &= \frac{d^2 I_c'}{dt'^2} \omega_o^2 \frac{I_Q}{V_T} L_1 \left[\tau_{eff} + C_{je} \frac{V_T}{I_Q} \frac{1}{I_c'} \right] \\ &+ \frac{dI_c'}{dt'} \omega_o \frac{I_Q}{V_T} r_b \left[\tau_{eff} + C_{je} \frac{V_T}{I_Q} \frac{1}{I_c'} \right] - \left[\frac{dI_c'}{dt'} \right]^2 \omega_o^2 \frac{1}{I_c'^2} L_1 C_{je} + \ln I_c' + \ln\left(\frac{I_Q}{I_S}\right). \end{aligned} \quad (4.16)$$

$$\frac{I_m}{I_Q} \sin t' = \frac{dI_c'}{dt'} \omega_o \left[\tau_{eff} + C_{je} \frac{V_T}{I_Q} \frac{1}{I_c'} \right] + I_c' - 1. \quad (4.17)$$

Equations (4.16) and (4.17) show that the normalized collector current I_c' depends on only a few normalized parameters, namely,

$$\frac{I_c}{I_Q} = f \left[\frac{I_m}{I_Q}, \frac{V_m}{V_T}, \omega_o^2 L_1 g_{mQ} \tau_{eff}, \omega_o r_b g_{mQ} \tau_{eff}, \omega_o \tau_{eff}, \omega_o^2 L_1 C_{je}, \omega_o r_b C_{je}, \omega_o \frac{C_{je}}{g_{mQ}} \right] \quad (4.18)$$

where V_m is the fundamental component of V_a and $g_{mQ} = I_Q / V_T$. The circuit operation can be examined by generating a numerical set of normalized curves versus the normalized parameters. For example, in Fig. 4.13 the normalized collector current at the fundamental frequency is plotted against the normalized resistance of the active circuit, defined as follows

$$\text{Real} \left\{ \frac{V_m}{V_T} \frac{I_Q}{I_m} \right\} = R_a^{(1)} g_{mQ} .$$

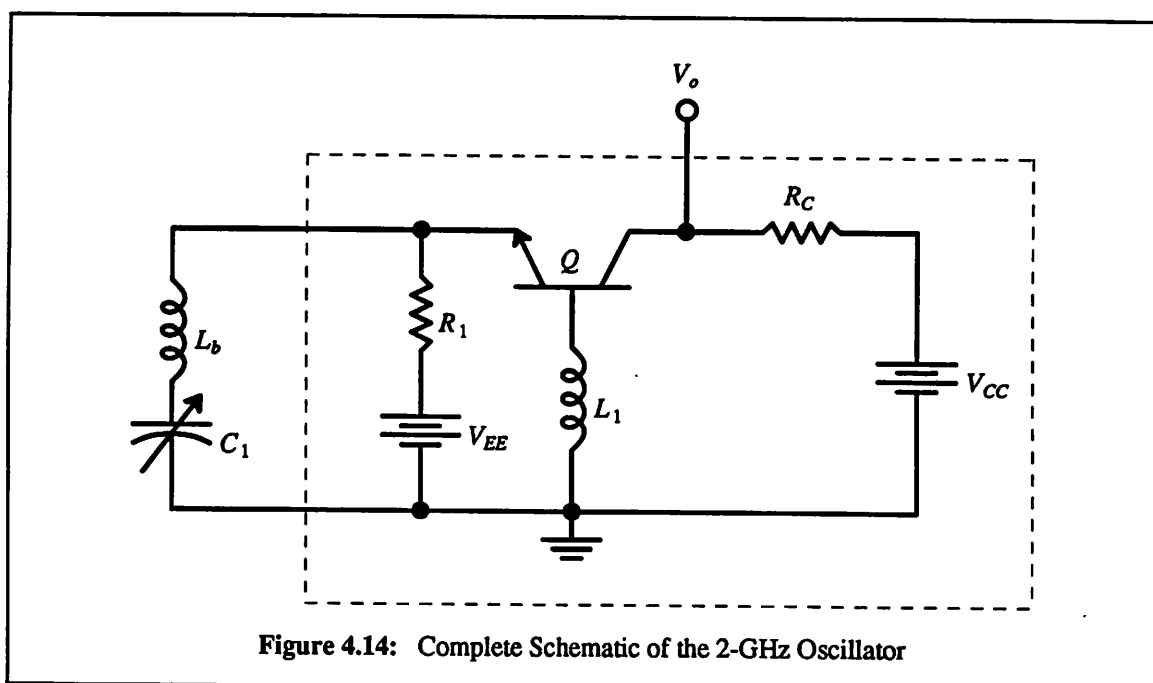
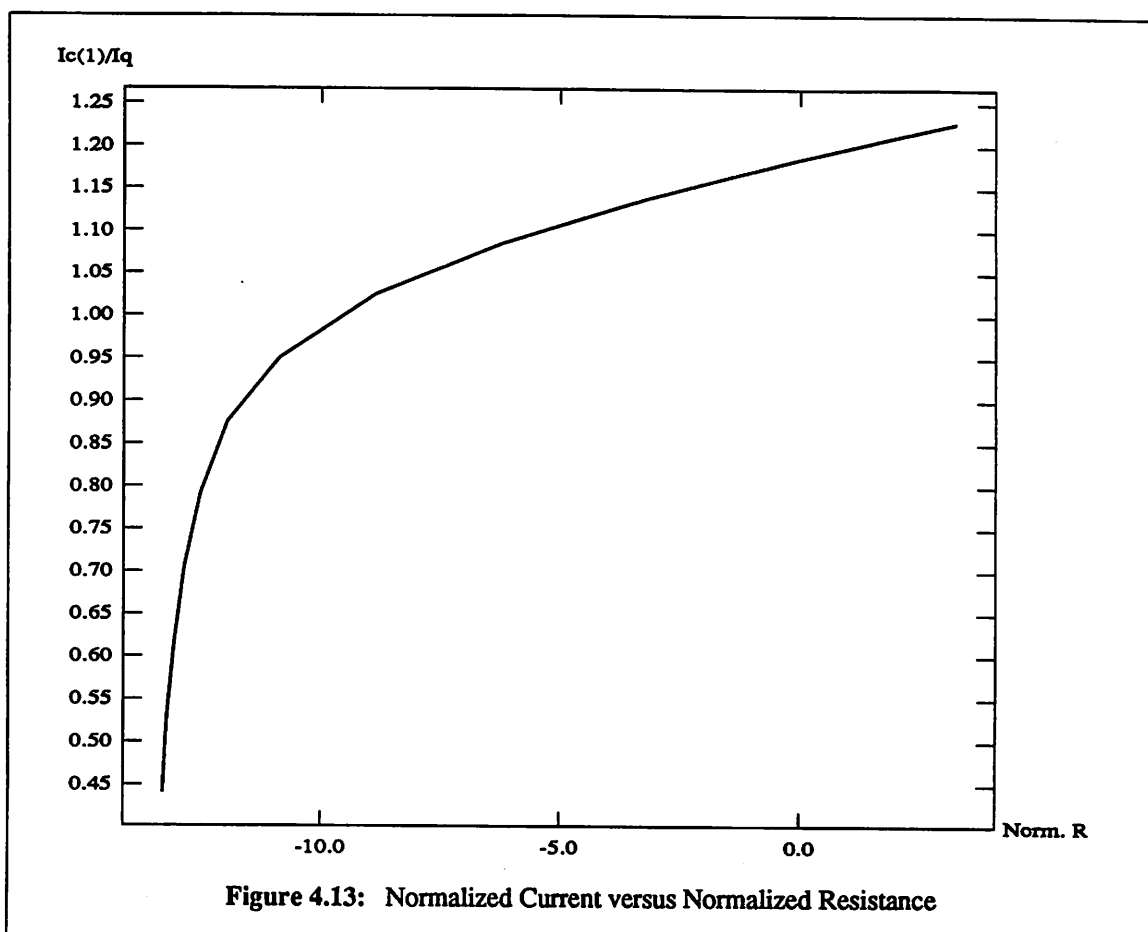
This plot predicts that the magnitude of the steady-state collector current is approximately equal to the bias current. With regard to the output signal stability against fluctuations in power supply and electronic noise, it can be shown that the circuit of Fig. 4.9 meets the amplitude-stability condition (3.30).

In conclusion, the systematic approach above provides us with the guidelines for designing well-behaved sinusoidal LC oscillators.

4.3. Implementation

To confirm the theoretical analysis and to demonstrate the feasibility of silicon integration, a monolithic implementation of the microwave oscillator shown in Fig. 4.14 has been fabricated and characterized. Capacitor C_1 is an off-chip varactor for frequency tuning. Bond-wire inductance L_b together with C_1 form a series LC resonant circuit. L_1 is a monolithic inductor of 1.5 nH [Chapter 5]. Resistor R_C is matched to the system impedance of 50 Ω . The bias current I_C is 10 mA. The circuit was fabricated in an oxide-isolated Si bipolar IC process with peak $f_T = 9$ GHz.

The die photograph of the oscillator is shown in Fig. 4.15. The circuit achieves a measured negative-resistance band of 2.5 GHz extending from 1.5 GHz to 4 GHz. With $C_1 = 3.9$ pF and $L_b = 0.7$ nH, the measured output waveform taken from the collector node is shown in Fig. 4.16. The measured



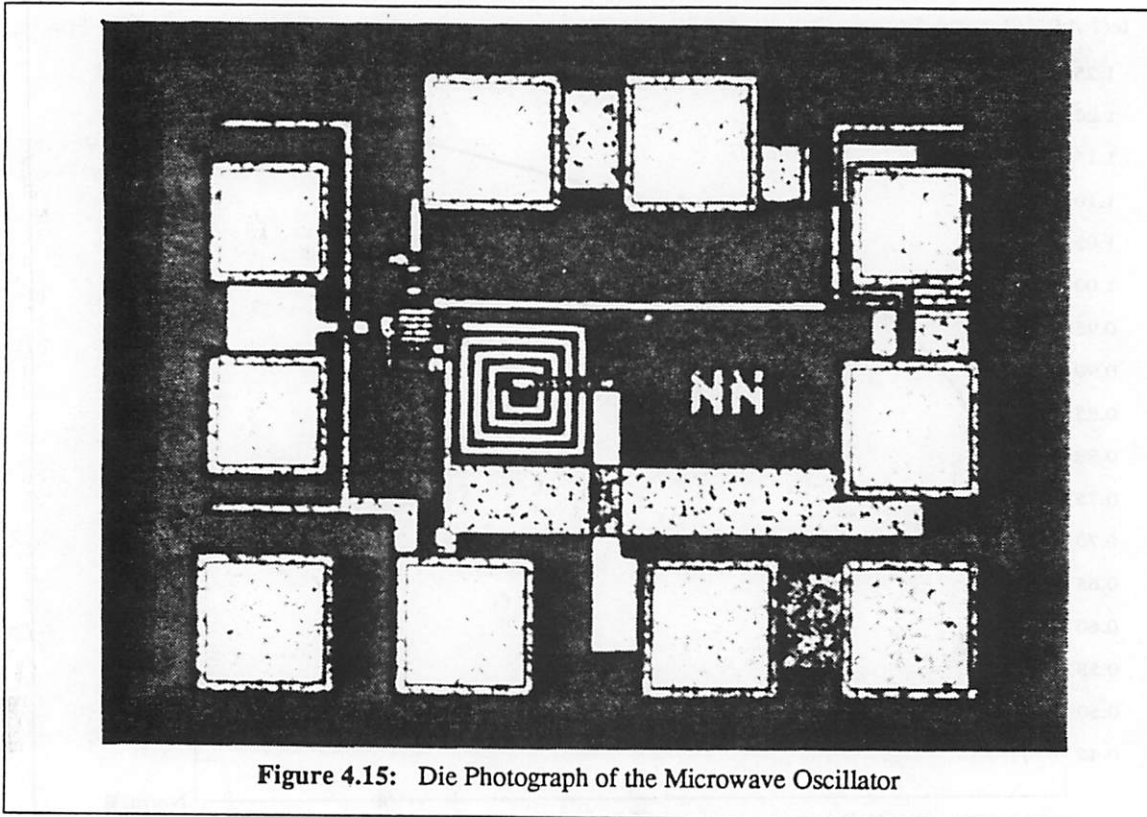


Figure 4.15: Die Photograph of the Microwave Oscillator

oscillation frequency is approximately 2 GHz compared to the simulated oscillation frequency of 2.1 GHz. The output power is -6.5 dBm and was measured across a $50\text{-}\Omega$ off-chip load. The simulated power is -4.0 dBm. The power loss is attributed to the package and the ac-bypass circuits that were used for the RF testing of this oscillator.

4.4. Summary

Systematic design approaches for VCNRs, ICNRs, and LC-dependent active circuits have been explored in this chapter. Combining the conventional start-up conditions with the Nyquist, root-locus, and Kurokawa analyses provide us with the guidelines for designing predictable sinusoidal LC oscillators. The conditions for frequency and amplitude stability provide the assurance that the oscillators are both frequency and amplitude stable.

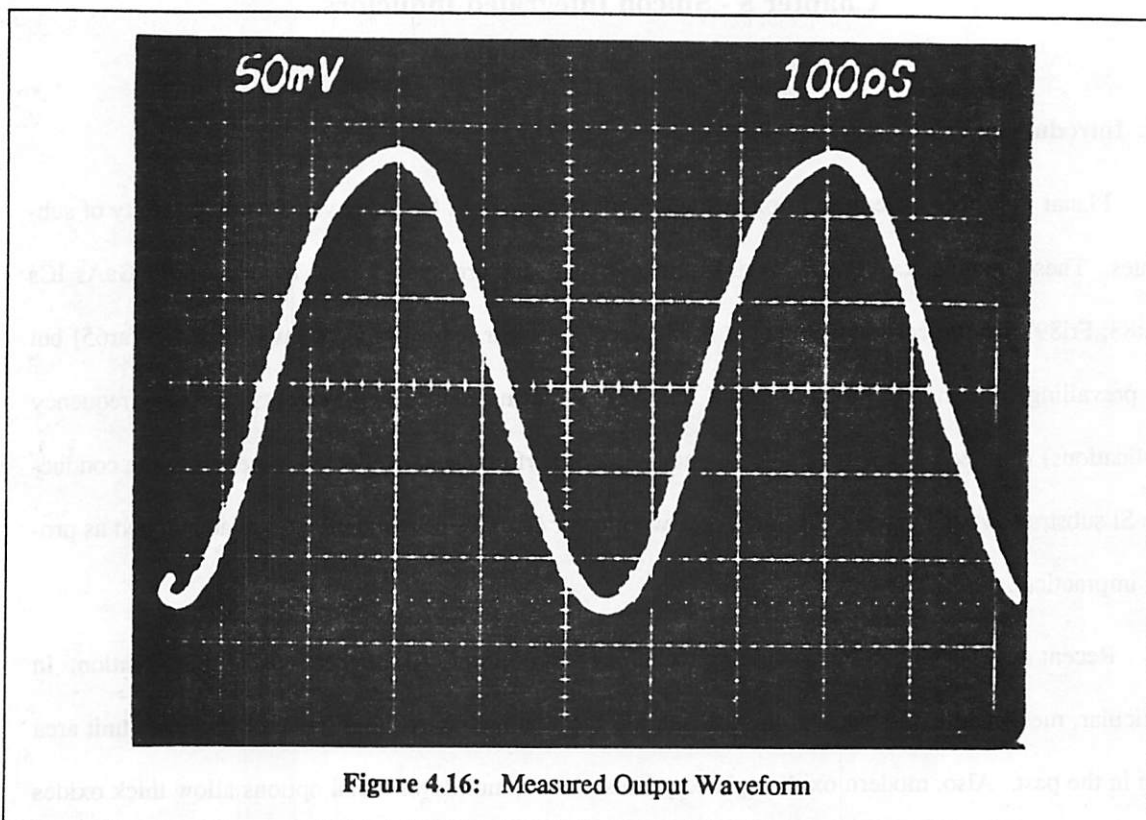


Figure 4.16: Measured Output Waveform

Chapter 5 - Silicon Integrated Inductors

5.1. Introduction

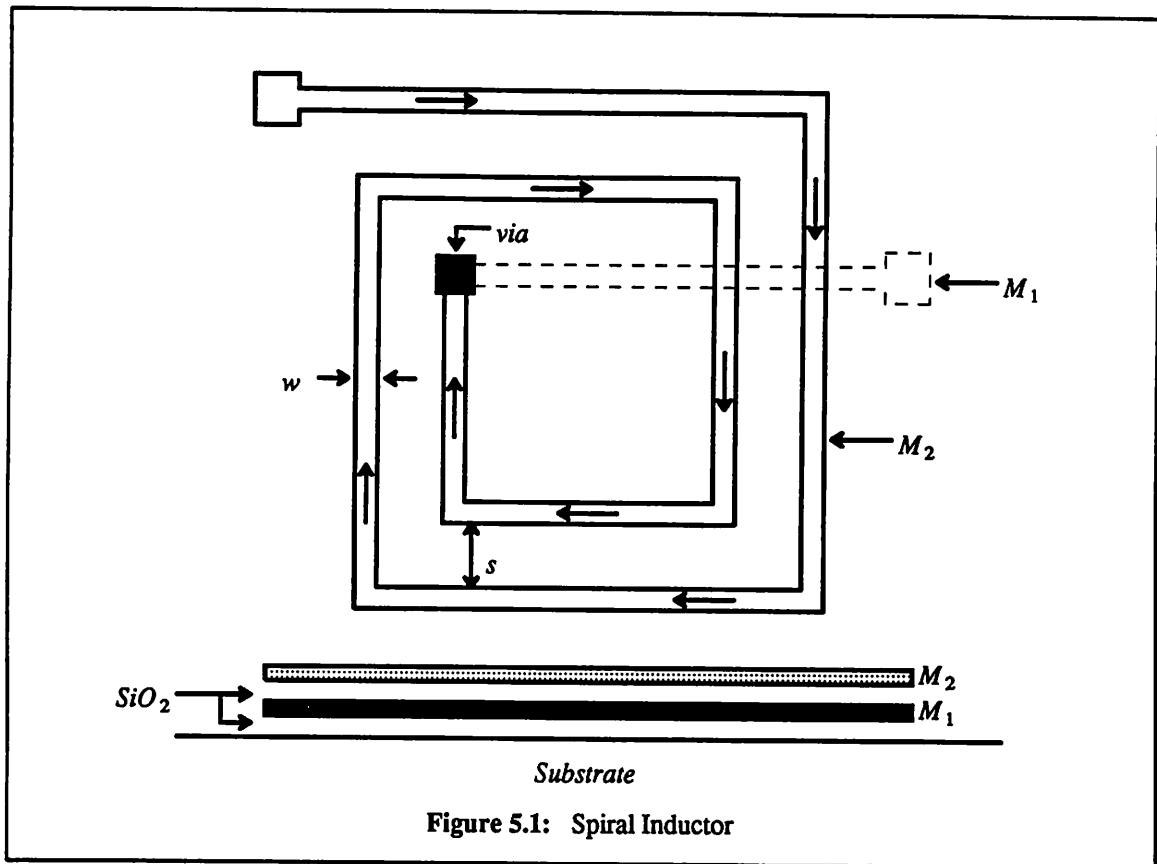
Planar inductors have been implemented in practical systems for many years using a variety of substrates. These include standard PC boards, ceramic and sapphire hybrids, and more recently GaAs ICs [Pet88, Fri89]. In the early development of silicon ICs, planar inductors were investigated [War65] but the prevailing lithographic limitations and relatively large inductance requirements (for low-frequency applications) resulted in excessive silicon area and poor performance. Reflected losses from the conductive Si substrate were a major contributor to low inductor Q . This research effort was abandoned as proven impractical.

Recent advances in Si IC processing technology have prompted another look at this situation. In particular, metal width and pitch in the low micron range allow many more inductor turns per unit area than in the past. Also, modern oxide-isolated processes with multilayer metal options allow thick oxides to help isolate the inductor from the Si substrate. In addition, interest is growing in applications at much higher frequencies with the advent of 900-MHz communications and gigahertz-range satellite reception. Inductors of only a few nano-Henries are sufficient in these high-frequency applications.

In this chapter we describe inductors fabricated in a production Si bipolar process featuring oxide isolation and two layers of metal. In the frequency range of interest (above about 1 GHz) the Q of the inductors is quite usable (3-8) and appears to be almost totally limited by metal and contact resistance, with little effect from the Si substrate. In this regard, there is little difference between these inductors and those implemented in GaAs.

5.2. Inductor Structure and Characterization

There are a number of possible inductor structures [Bah88]. They include strip, loop, and spiral inductors. For inductors of a few tens of nano-Henries, the square-spiral structure [Fig. 5.1] is suitable for monolithic integration. In this structure the top metal layer M_2 is used predominantly to minimize the parasitic metal-substrate capacitance and the accumulated sheet resistance, while the bottom layer M_1



is used as the lead-out bridge. In order to facilitate the characterization of this inductor structure, we first discuss two fundamental concepts: the self inductance and mutual inductance. In any current-carrying conductor there is an associated self inductance, defined as the ratio of the change in magnetic flux to the change in current. For the rectangular conductor shown in Fig. 5.2(a), Grover has derived a closed-form self-inductance expression that depends on the length, width, and thickness of the conductor [Gro46]. And for any pair of parallel conductors, there is a mutual inductance due to the magnetic coupling between them. This mutual inductance is positive if the currents in the two conductors point in the same direction, and negative otherwise. Grover has also derived a closed-form mutual-inductance expression for the two parallel rectangular conductors shown in Fig. 5.2(b). It is important to emphasize that if the conductors are made of non-magnetic materials, the associated inductance is independent of the current strength and only depends on the geometry of the conductors. Also, the "skin effect" is neglected in Grover's analysis (the current is assumed uniformly distributed over the cross section of the conductor).

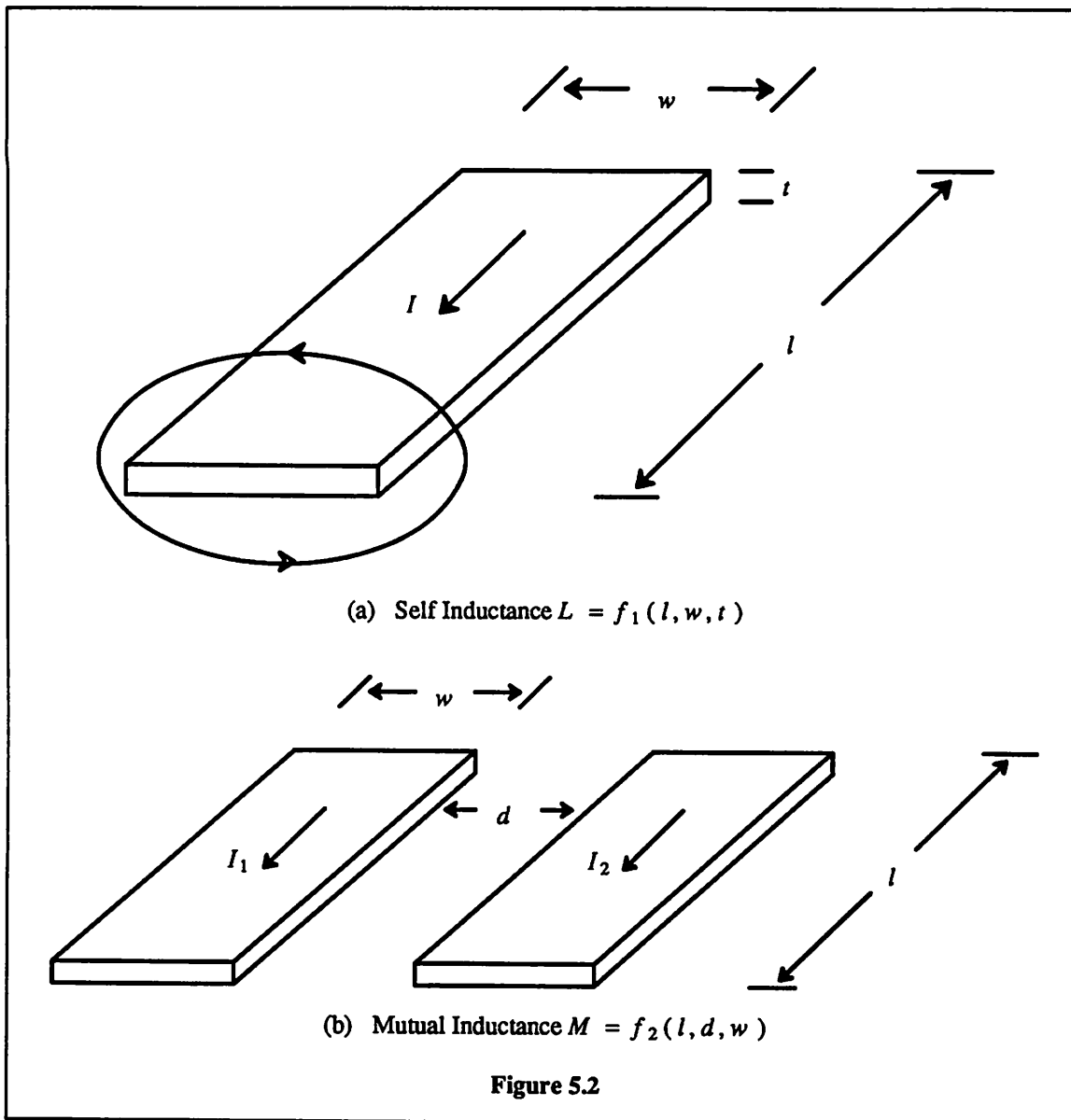
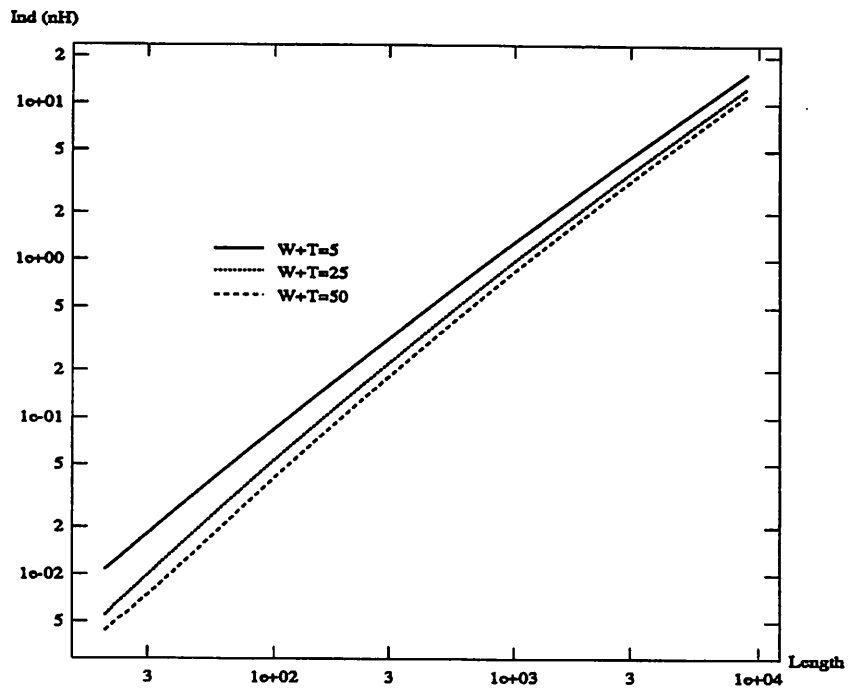


Figure 5.2

This assumption may not be valid at very high frequencies where the current tends to crowd toward the surface of the conductor. Figures 5.3(a) and 5.3(b) show, respectively, the self inductance of a rectangular conductor and the mutual inductance between two parallel rectangular conductors. The mutual inductance is observed to depend significantly on the space separating the two conductors. This observation suggests that the spacing between metal segments in the spiral inductor should be minimized in order to achieve a high ratio of inductance per unit area, which in turn implies higher inductor Q .



(a) Self Inductance for Different Combinations of Conductor Width and Thickness

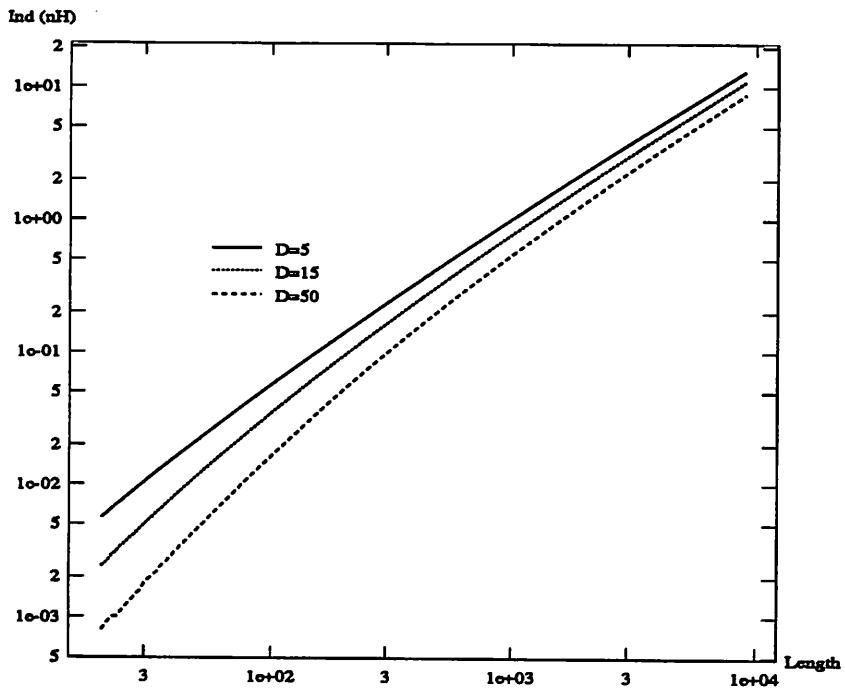
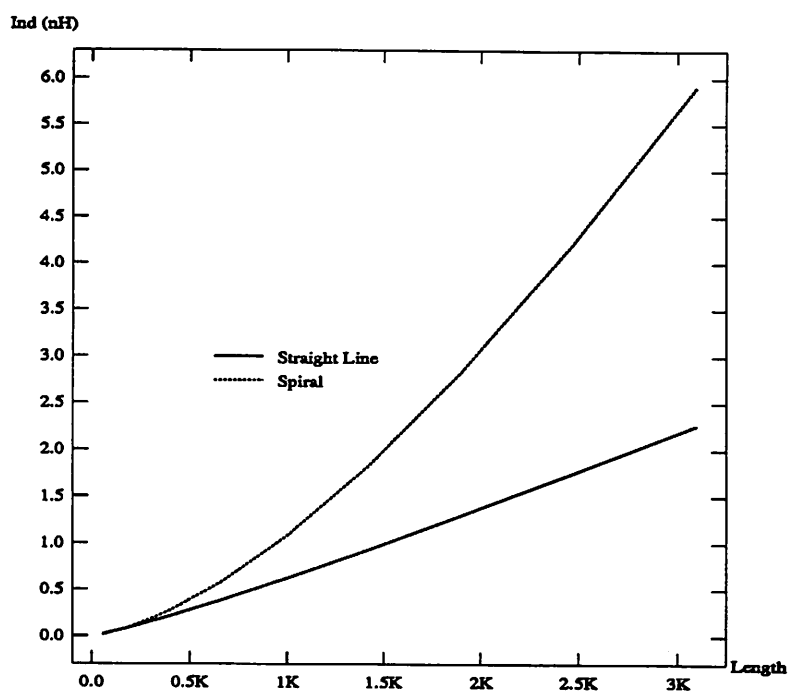
(b) Mutual Inductance as a function of Spacing (μm)

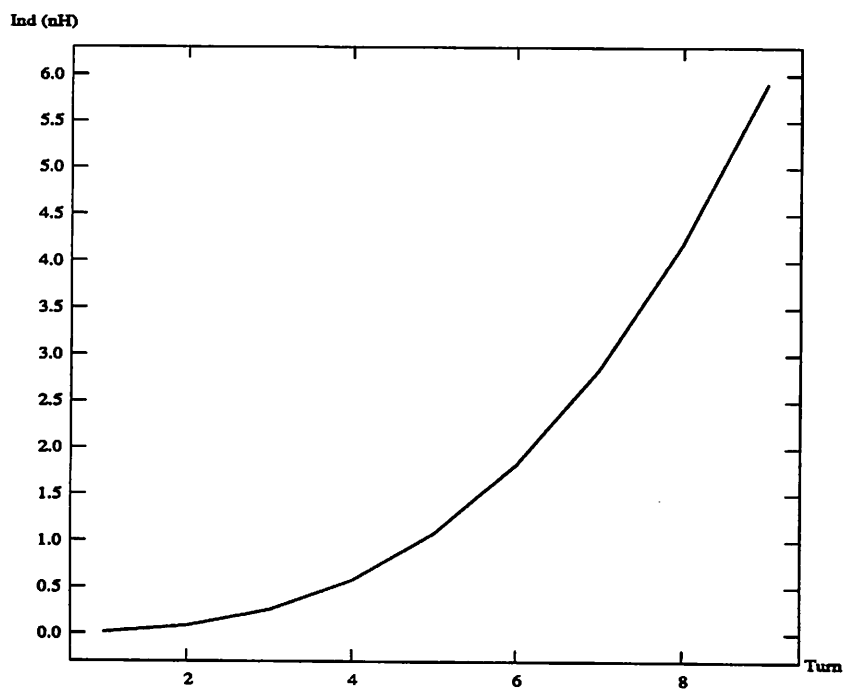
Figure 5.3

The effective inductance of the spiral structure can be shown to be the sum of all the self-inductance terms and mutual-inductance terms [Gre74]. This inductance calculation can be numerically intensive and is best solved with a software program. Appendix B lists the source code of a software package developed during the course of this research and has been used for predicting the inductance value of the spiral inductor. Note that the segments having the same current direction in the spiral structure of Fig. 5.1 are relatively near to each other, whereas the segments having the opposite current direction are farther apart. The positive mutual inductance is hence typically larger than the negative mutual inductance, and thus enhance the effective inductance of the spiral inductor. Figure 5.4(a) shows the inductance achieved with a straight-line inductor and that achieved with a spiral inductor of the same effective length. The spiral inductor is observed to have higher inductance due to the positive mutual inductance enhancement. The inductance as a function of turn number is shown in Fig. 5.4(b).

An equivalent circuit for the square-spiral inductor has been derived and is shown in Fig. 5.5. In this circuit, L_e models the effective inductance, R_s is the accumulated sheet resistance, C_p models the parasitic capacitance from the second-metal layer to the substrate, and R_p represents the resistance of the conductive silicon substrate. Coupling capacitance between metal segments due to fringing fields in both the dielectric region and the air region is neglected in this model. Such an approximation is valid because the relative dielectric constant of the oxide is small and the inductor is used at frequencies well below its self-resonant frequency. Since the structure of the square-spiral inductor is not symmetrical, the parasitic capacitance values at the inductor terminals should be different from one another. This difference, however, is small [Par84] and the two capacitors are assumed the same. If the spiral inductor is modeled as a lossless transmission line with the total length much smaller than the quarter wavelength, it can be shown that C_p is approximately equal to one half the input capacitance of the open-circuited line [Appendices B and C]. This gives a first-order estimate of C_p . More accurate analytical expressions for C_p can be found in [Gar79]. The substrate resistance R_p can be derived from measured S parameters. It is interesting to note that in a GaAs inductor using microstrip lines, substrate resistance R_p is not present because the GaAs substrate acting as the dielectric layer is in direct contact with the conductive ground plane.

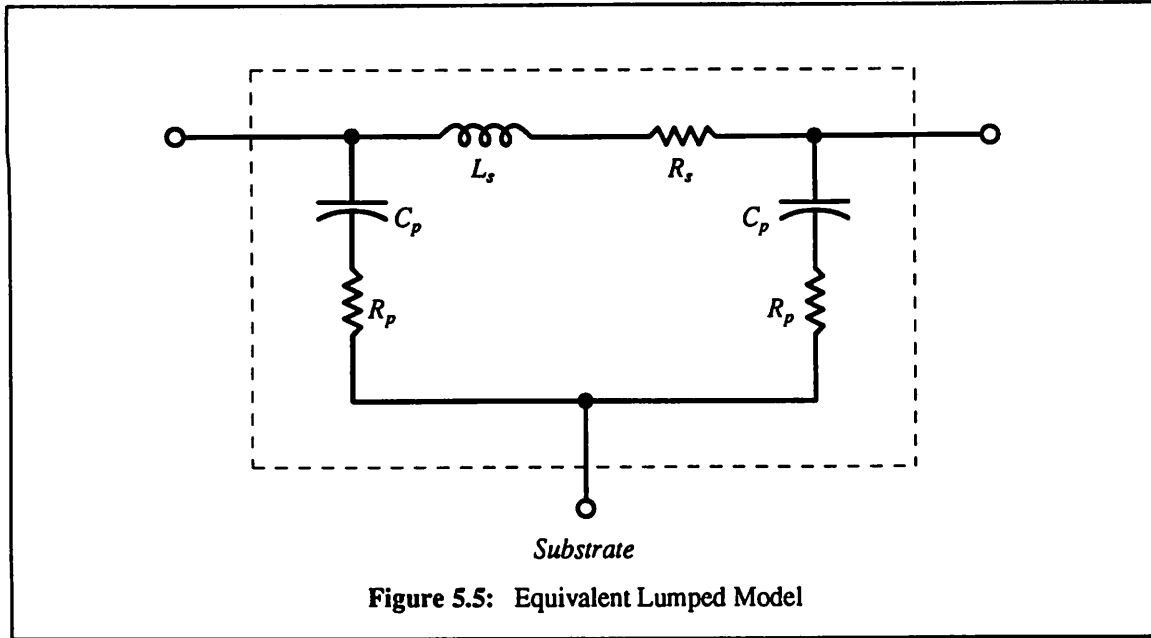


(a) Straight Line versus Spiral for the Same Effective Length (μm)



(b) Inductance versus Turn Number

Figure 5.4: $W = 7 \mu\text{m}$, $S = 2 \mu\text{m}$, $T = 1.8 \mu\text{m}$, $l_1 = l_2 = 21 \mu\text{m}$ (innermost)



If one side of the inductor is grounded, the self-resonant frequency of the spiral inductor can be derived from the equivalent circuit. It is approximately equal to

$$\omega_R = \frac{1}{\sqrt{L_s C_p}} \left[\frac{1 - R_s^2 \left[\frac{C_p}{L_s} \right]}{1 - R_p^2 \left[\frac{C_p}{L_s} \right]} \right]^{\frac{1}{2}} \quad (5.1)$$

Beyond the resonant frequency, the inductor becomes capacitive. Frequency ω_R is limited mainly by C_p which is inversely proportional to the oxide thickness between the second-metal layer and the substrate.

The frequency at which the inductor Q is maximum can also be derived. It is

$$\omega_Q = \frac{1}{\sqrt{L_s C_p}} \left\{ \frac{R_s}{2 R_p} \left[\left[1 + \frac{4 R_p}{3 R_s} \right]^{\frac{1}{2}} - 1 \right] \right\}^{\frac{1}{2}} \quad (5.2)$$

If the inductor is used as a floating inductor, the shunt branches in the equivalent circuit are effectively in series with one another. Equations (5.1) and (5.2) still hold provided that C_p and R_p are replaced by $\frac{C_p}{2}$ and $2 R_p$, respectively.

5.3. Implementations

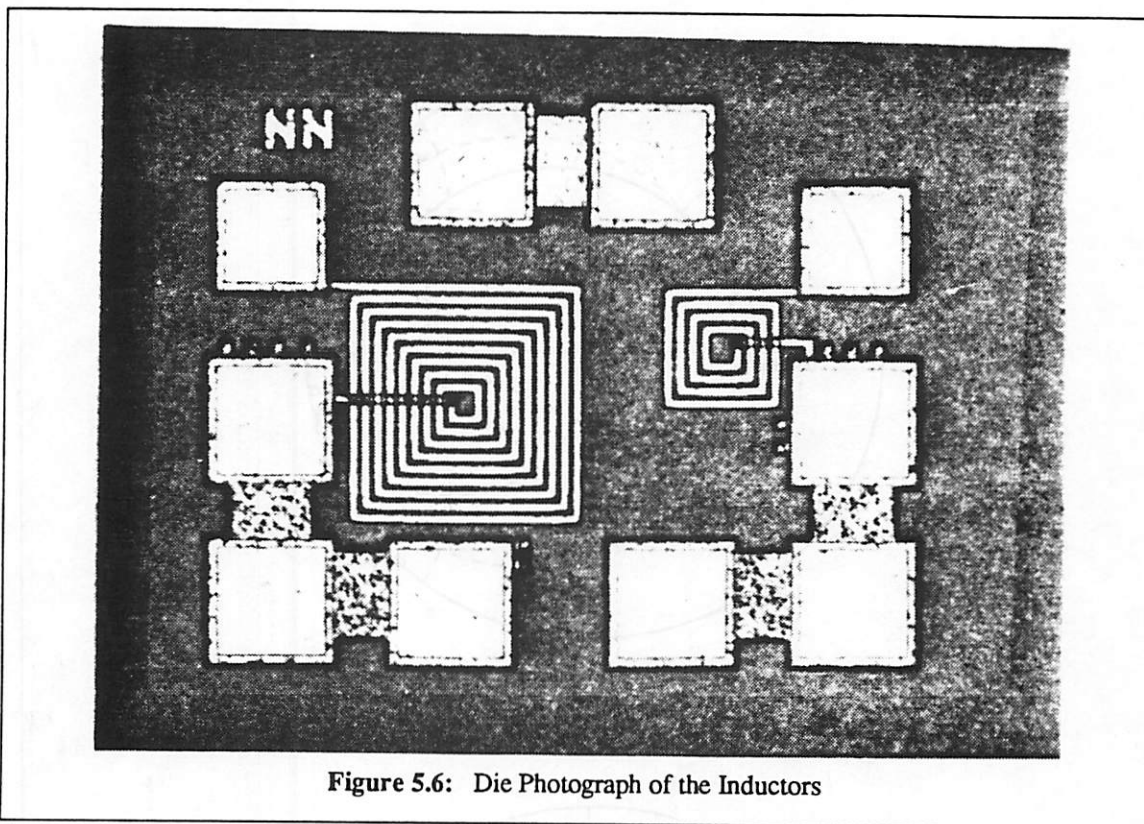
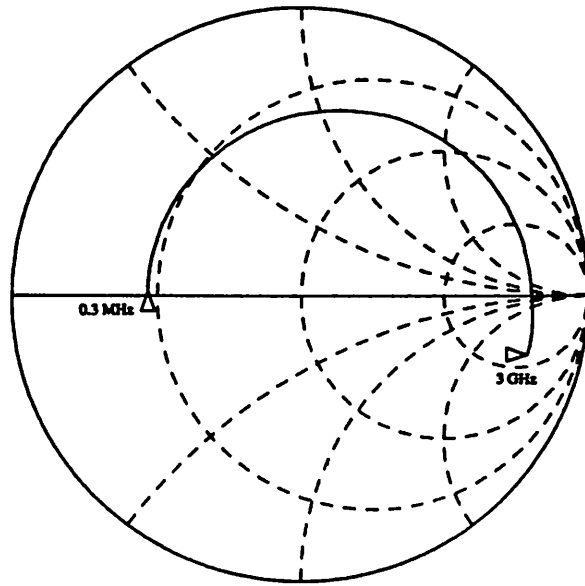
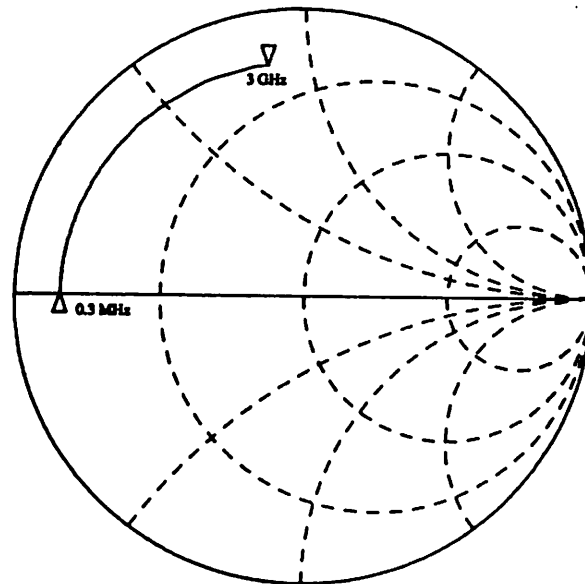


Figure 5.6: Die Photograph of the Inductors

Two square-spiral inductors were fabricated, measured, and characterized. A die photo of the test layout is shown in Fig. 5.6. Metal width was $6.5\ \mu\text{m}$ with $5.5\text{-}\mu\text{m}$ spacing of $1.8\text{-}\mu\text{m}$ -thick second-metal Al. The sheet resistance of Al was $20\ \text{m}\Omega/\square$ over $1.7\ \mu\text{m}$ of oxide, and the parasitic capacitance from Al to the substrate was $0.016\ \text{fF}/\mu^2$. The substrate resistivity was $14\ \Omega\text{-cm}$ and $500\text{-}\mu\text{m}$ -thick p-type silicon. The larger inductor had 9 turns with an outer dimension of about $230\ \mu\text{m}$. The smaller one had 4 turns with an outer dimension of about $115\ \mu\text{m}$. Measured S_{11} plots from $0.3\ \text{MHz}$ to $3\ \text{GHz}$ for these inductors in a $50\text{-}\Omega$ system are shown in Fig. 5.7. The large inductor is self resonant at $2.47\ \text{GHz}$ while the small one has an estimated resonant frequency of $9.7\ \text{GHz}$. Pad capacitance was zeroed out of the on-chip measurement. The large inductor had a measured value of $9.7\ \text{nH}$ while the smaller was $1.9\ \text{nH}$. The theoretical values are, respectively, $9.3\ \text{nH}$ and $1.3\ \text{nH}$. The differences are attributed to lead inductances and possible minor imprecision in calibration of the test equipment. The series loss in the inductors deduced from RF measurements agreed very closely with measured and predicted dc series



(a) Small Inductor



(b) Large Inductor

Figure 5.7: Measured S_{11} from 0.3 MHz to 3 GHz

resistance, indicating that coupled loss from the silicon substrate was negligible. While metal shrinkage due to photolithography and etching tolerances can affect the series-loss value, it theoretically has negligible effect on the inductance value. With a typical $\pm 0.2\text{-}\mu\text{m}$ metal shrinkage, the inductance value in the large inductor has been calculated to vary less than 1%. The large inductor has a measured maximum- Q of 3 at 0.9 GHz and the small one has an estimated maximum- Q of 8 at 4.1 GHz. Circuit elements in the equivalent circuit for the large inductor were derived from both theory and measured S parameters. The set $\{L_s, R_s, C_p, R_p\}$ is equal to $\{9.7\text{ nH}, 15.4\ \Omega, 590\text{ fF}, 70\ \Omega\}$.

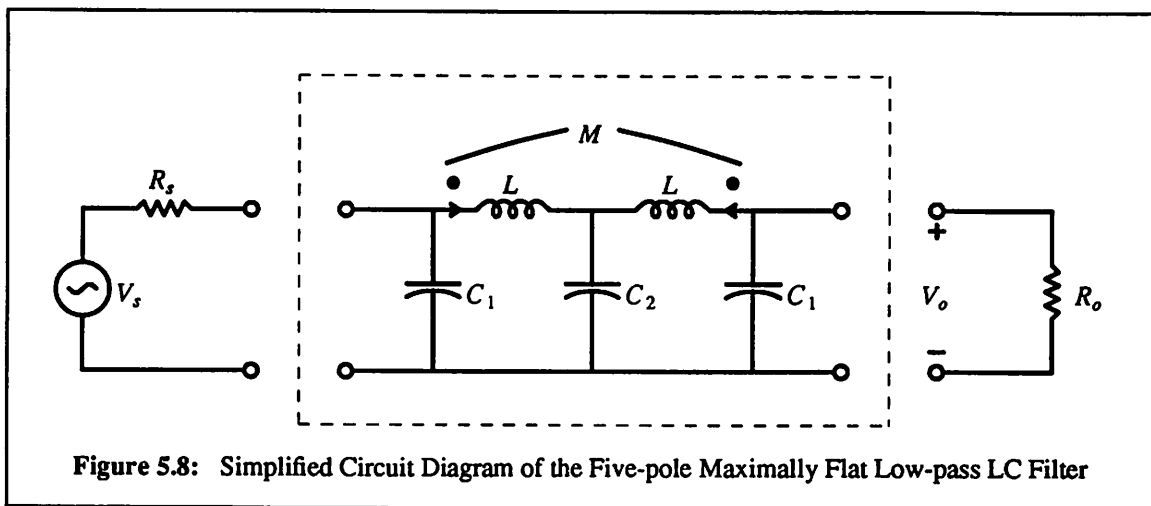


Figure 5.8: Simplified Circuit Diagram of the Five-pole Maximally Flat Low-pass LC Filter

As a test vehicle, a five-pole maximally flat low-pass filter with nominal designed -3-dB frequency of 880 MHz and midband insertion loss of 2.25 dB was fabricated. The circuit is shown in Fig. 5.8 where R_s and R_o are $50\text{-}\Omega$ off-chip resistors. Element values are $L \approx 9.7\text{ nH}$, $M \approx 0.4\text{ nH}$, $C_1 \approx 1.3\text{ pF}$, and $C_2 \approx 4.3\text{ pF}$ where parasitic capacitance associated with the inductors is included in the capacitor values. Mutual inductor M exists between the inductors due to layout proximity. The capacitors were fabricated in standard form using metal over $1500\ \text{\AA}$ of oxide with an n^+ bottom plate. Since the sheet resistance of n^+ is high ($20\ \Omega/\square$), the series loss in the capacitor must be minimized by reducing the ratio $\frac{L}{W}$, where L and W are, respectively, the length and width that define the capacitor area. Pads were included with the filter to allow testing but were not included in the design and were zeroed out of the on-chip measurements. This would correspond to use of such a filter in an on-chip environment where pads are not present. If a packaged stand-alone filter was required, pads and bond wires would have to be included in

the design.

The transfer function can be derived from the simplified circuit in Fig. 5.8 and is given by

$$\frac{V_o(s)}{V_s(s)} = \frac{a_2 s^2 + a_0}{b_5 s^5 + b_4 s^4 + b_3 s^3 + b_2 s^2 + b_1 s + b_0} \quad (5.3)$$

where

$$a_2 = MC_2$$

$$a_0 = 1$$

$$b_5 = (L-M)C_1 (L+M)C_2 R_s C_1$$

$$b_4 = (L-M)C_1 (L+M)C_2 \left[1 + \frac{R_s}{R_o} \right]$$

$$b_3 = (L+M)C_2 \frac{(L-M)}{R_o} + [2(L-M)C_1 + 2LC_2] R_s C_1$$

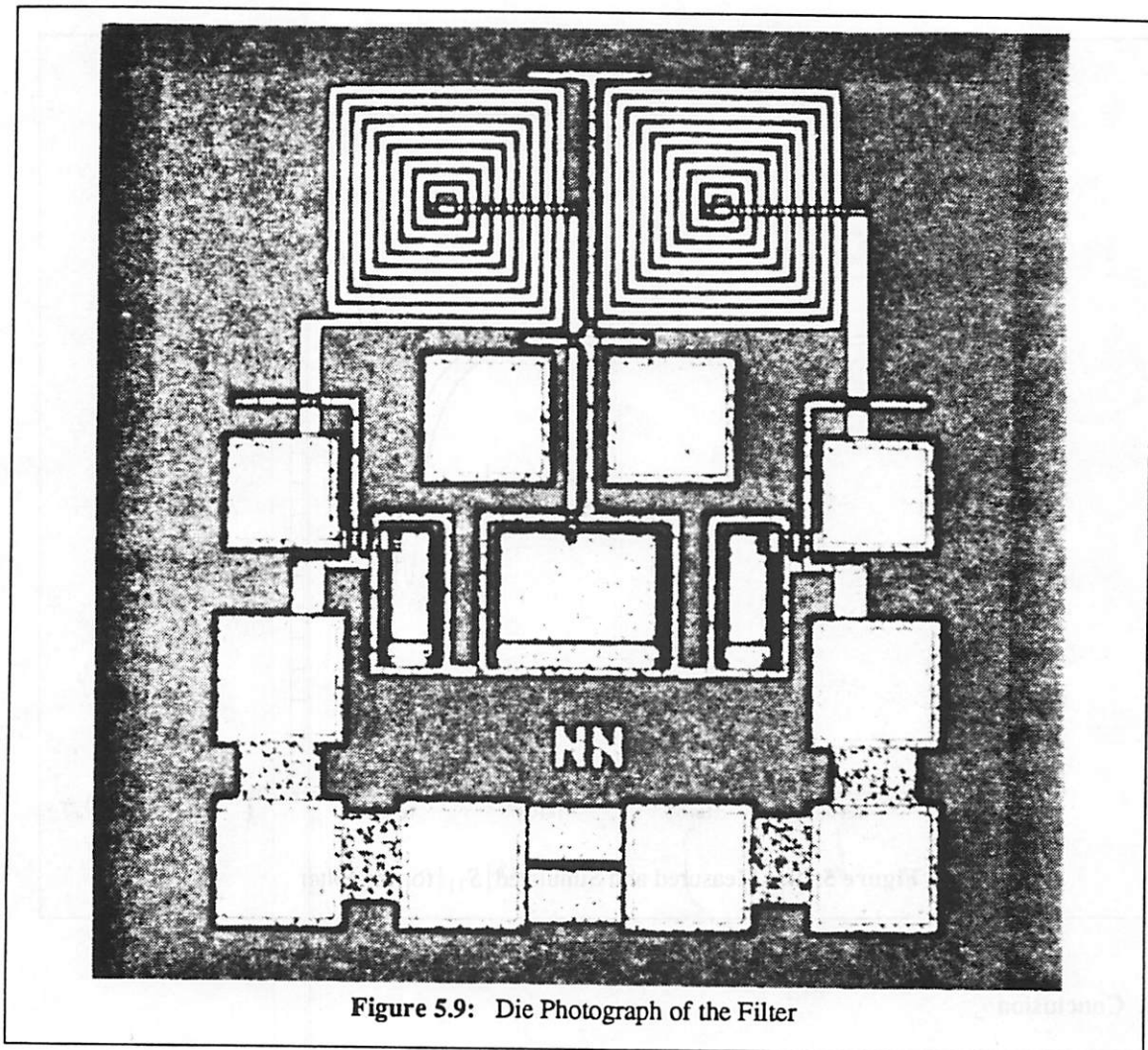
$$b_2 = 2(L-M)C_1 + LC_2 + \frac{R_s}{R_o} [2(L-M)C_1 + LC_2]$$

$$b_1 = 2 \frac{(L-M)}{R_o} + R_s (2C_1 + C_2)$$

$$b_0 = \left[1 + \frac{R_s}{R_o} \right].$$

As seen from (5.3), the mutual inductance M creates two high-frequency zeros on the $j\omega$ axis. Since M is relatively small compared to the inductance value L , its effect on the filter attenuation is significant only in the stopband. Let $f_z (= 1/[2\pi\sqrt{MC_2}])$ denote the magnitude of the complex-conjugate zeros. It can be shown that the zeros increase the stopband loss at frequencies below f_z but decrease the loss at frequencies above. If maximum high-frequency attenuation is desired, the value of M should be minimized by separating the two inductors far apart in the layout. If $M = 0$, (5.3) reduces to a simple five-pole transfer function.

A die photo of the filter is shown in Fig. 5.9. In order to minimize the electrical coupling through the substrate, a buried p-type layer was placed around the I/O pads and around the periphery of each device. Measured $|S_{11}|$ is shown in Fig. 5.10 and is close to the simulated values. The filter was simulated using the 3σ limits of capacitance of $\pm 10\%$ due to process variations but assuming all capacitors tracked



closely. The resulting spread of S_{21} characteristics is shown in Fig. 5.11 together with two measured characteristics from opposite sides of a 4-in wafer. The filter has a measured midband insertion loss of 2.4 dB and measured -3 -dB frequencies of 845 MHz and 860 MHz. Simulation with capacitor tolerances predicted the -3 -dB frequencies at 830 MHz, 880 MHz, and 930 MHz with 880 MHz being the nominal design value.

Since MOS capacitors display small but finite voltage coefficients [McC81], the filter was checked for nonlinearity by a third-order intermodulation measurement at 500 MHz. Measurements at signal levels of +15 dBm indicated that the third-order intercept was better than the measurement resolution of +42 dBm.

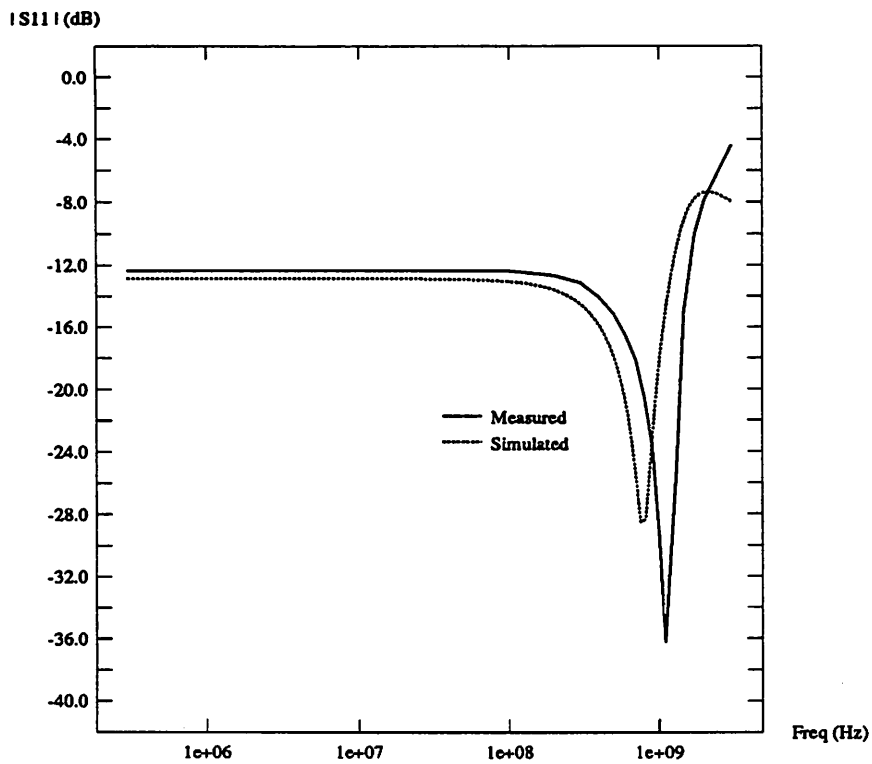
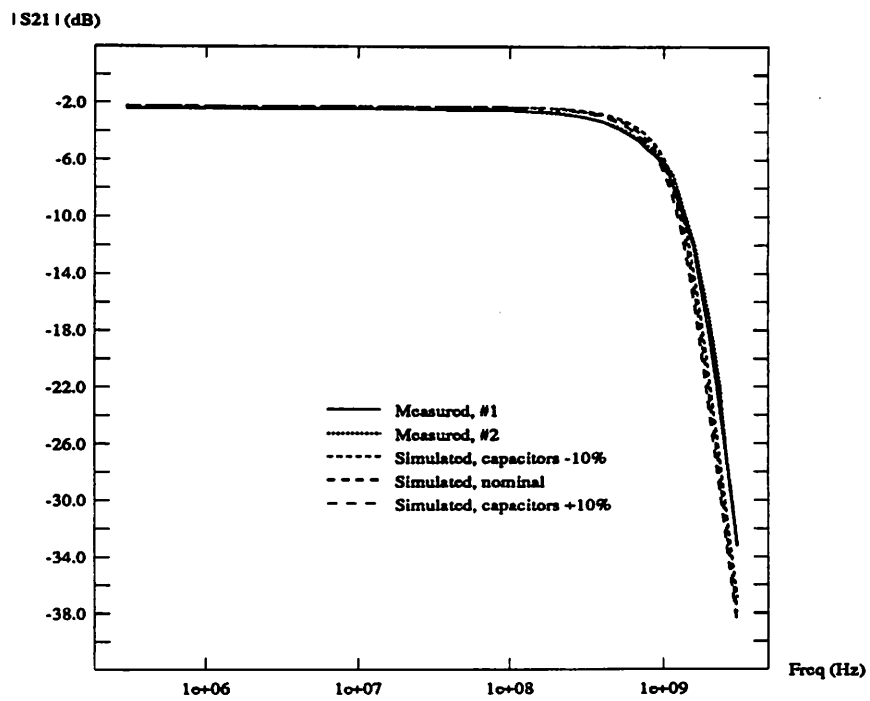


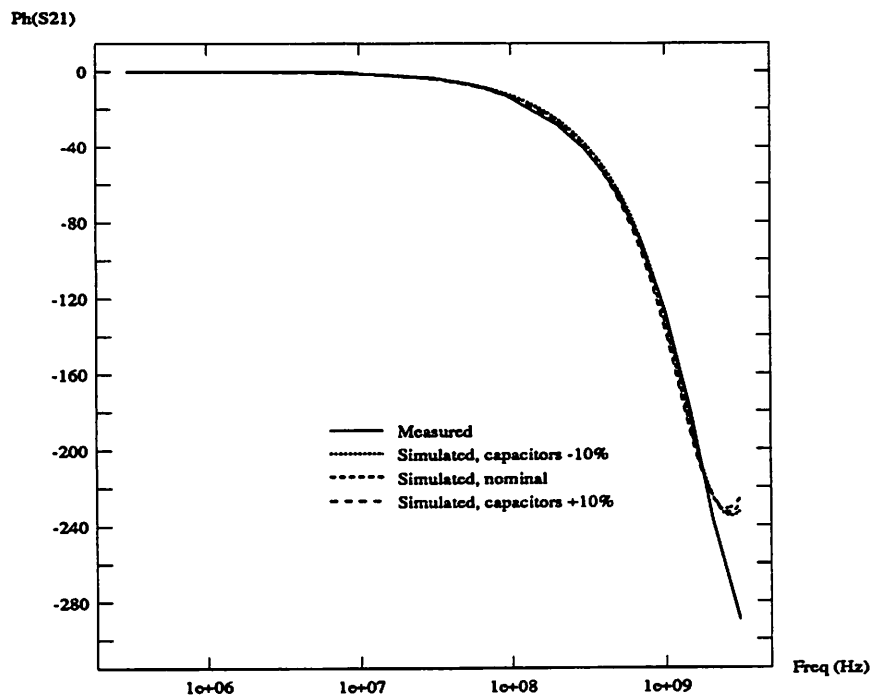
Figure 5.10: Measured and Simulated $|S_{11}|$ for the Filter

5.4. Conclusion

Passive inductors and LC filters useful in the gigahertz range are demonstrated in standard Si IC processing. These elements can be used for high-frequency on-chip filtering, inductive peaking of high-frequency amplifiers, and impedance matching for low-noise amplifiers.



(a) Magnitude



(b) Phase

Figure 5.11: Measured and Simulated S_{21} Characteristics of the Filter

Chapter 6 - Monolithic LC Voltage-Controlled Oscillators

6.1. Introduction

In the design of a phase-locked loop (PLL) [Fig. 6.1], the voltage-controlled oscillator (VCO) is the most critical component since its characteristics directly determine the performance of the system. Important characteristics of the VCO include frequency stability, linear voltage-to-frequency conversion, wide tuning range, high-frequency capability, frequency accuracy, and monolithic-technology compatibility. The VCO characteristics depend strongly on the VCO configurations [Liu88]. Depending on the shape of the oscillation waveform, we can categorize VCO circuits into two groups: relaxation oscillators and sinusoidal oscillators. A relaxation VCO produces either a square or triangular signal, whereas a sinusoidal VCO produces a near-sinusoidal signal. Most presently available VCOs in monolithic IC technology are relaxation based since they require only capacitors as the frequency-selective elements [Cor75]. Sinusoidal VCOs on the other hand often require external varactors (voltage-controlled capacitors) and inductors for defining oscillation frequency and hence are not suitable for monolithic integration.

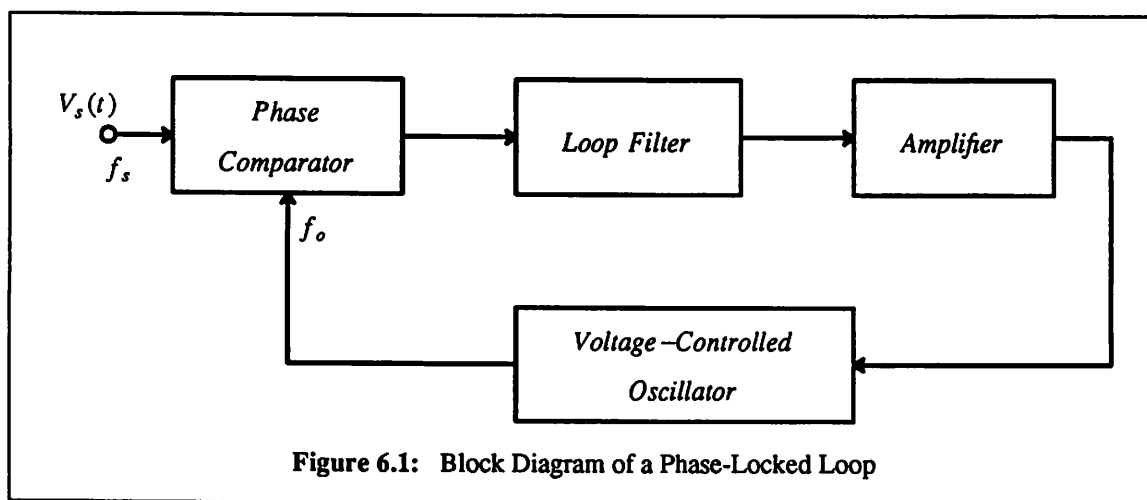
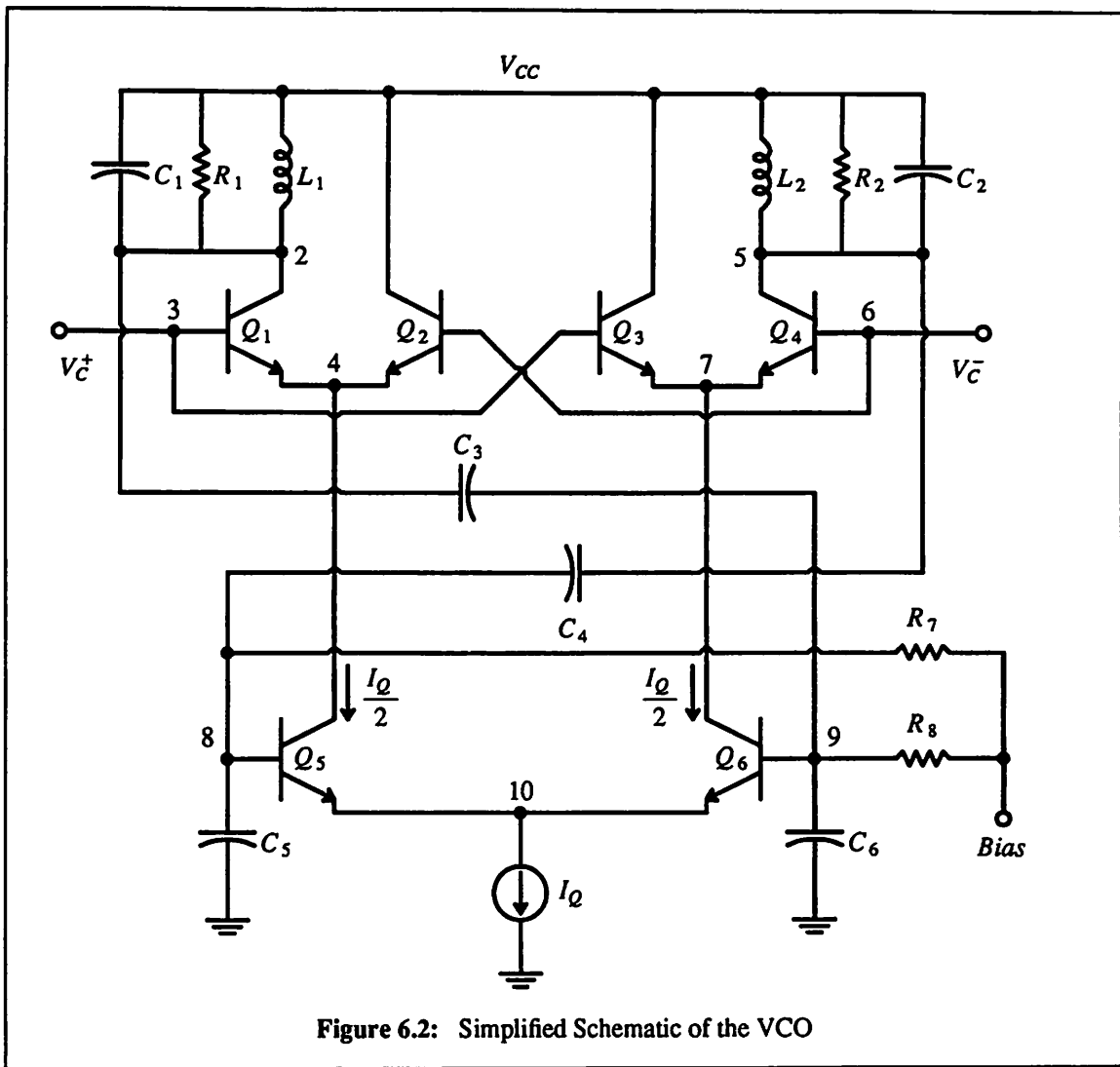


Figure 6.1: Block Diagram of a Phase-Locked Loop

In this chapter we discuss a novel microwave sinusoidal VCO in monolithic IC technology. The circuit does not require a varactor for frequency tuning but instead relies on characteristics inherent in the circuit configuration. As a test vehicle, a Si bipolar monolithic VCO has been fabricated. It achieves a



simulated tuning range of 300 MHz extending from 1.5 GHz to 1.8 GHz. The oscillator was fabricated in an oxide-isolated BiCMOS IC process with typical f_T (npn) = 10 GHz.

6.2. Circuit Configuration

The simplified circuit schematic of the LC VCO is shown in Fig. 6.2. It consists of two capacitive-feedback Colpitts oscillators. The *left* oscillator is comprised of Q_1 , L_1 , R_1 , C_1 , C_3 , and C_6 . The *right* oscillator is comprised of Q_4 , L_2 , R_2 , C_2 , C_4 , and C_5 . Voltages V_C^+ and V_C^- control the amount of bias current I_Q that flows into the two Colpitts oscillators. We now study the properties inherent in this circuit configuration that dictate the voltage-frequency translation.

6.2.1. Oscillation Frequency

The characteristics of this cross-coupled LC VCO are best understood using the feedback model discussed in Chapter 2. Let $T_1(\omega)$ and $T_2(\omega)$ denote the loop gains of the two Colpitts oscillators. Furthermore, let α_1 and α_2 denote the fractions of bias current $I_Q / 2$ that drive the transistors Q_1 and Q_4 ($0 \leq \alpha_1 \leq 1$, $0 \leq \alpha_2 \leq 1$, $\alpha_1 + \alpha_2 = 1$). Quantities α_1 and α_2 are set by voltages V_C^+ and V_C^- , respectively. It is shown in Section 6.3 that the effective loop gain for the circuit of Fig. 6.2 is

$$T(\omega) = \alpha_1 T_1(\omega) + \alpha_2 T_2(\omega). \quad (6.1)$$

It is shown subsequently that the conventional start-up condition is valid for this feedback oscillator. According to this condition, the circuit of Fig. 6.2 is unstable about its bias point if the loop gain (6.1) is larger than one at the zero-phase frequency. Since the zero-phase frequency is often used as an estimate for the oscillation frequency, we observe from (6.1) that if $\alpha_1 \gg \alpha_2$, the zero-phase frequency is determined mainly by the left Colpitts oscillator; whereas if $\alpha_2 \gg \alpha_1$, it is determined mainly by the right Colpitts oscillator; and if α_1 and α_2 are comparable to one another, both oscillators are equally significant. If $\alpha_2 = 0$ ($\alpha_1 = 1$), the circuit of Fig. 6.2 effectively reduces to a simple Colpitts oscillator. Under this condition the effective oscillation frequency is solely determined by the left (right) oscillator.

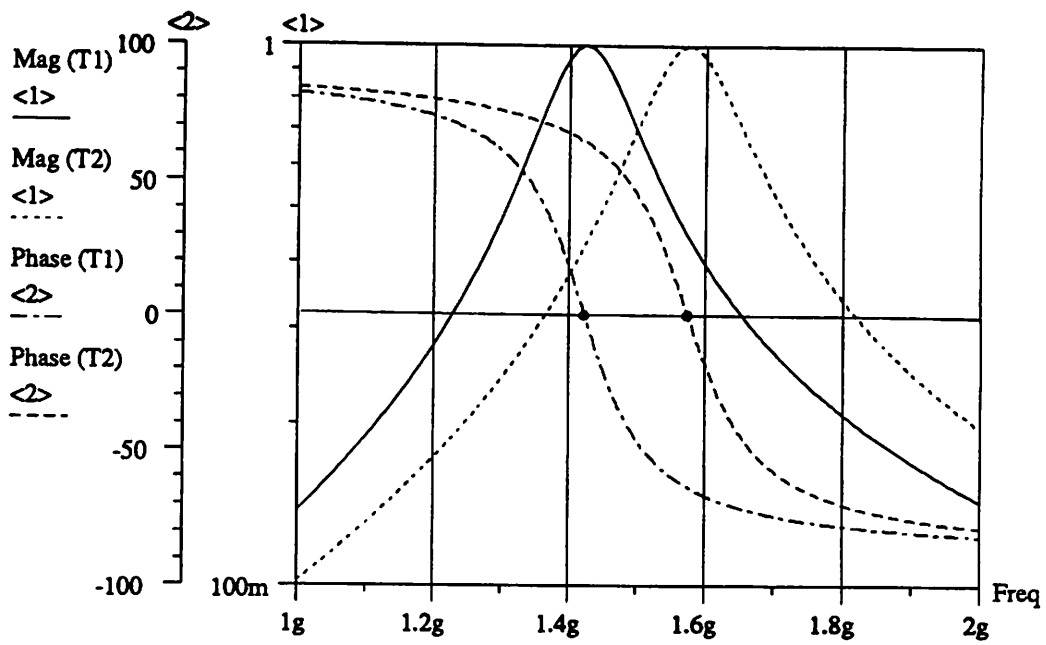
To understand the summing property of (6.1) further, we consider the simulated loop gains $T_1(\omega)$ and $T_2(\omega)$ in Fig. 6.3(a) assuming the same tank-circuit Q and the same maximum loop gain. Quantities ω_1 and ω_2 denote the zero-phase frequencies of the stand-alone Colpitts oscillators and are related to each other according to

$$\omega_2 - \omega_1 = \frac{\omega_C}{Q} \quad (6.2)$$

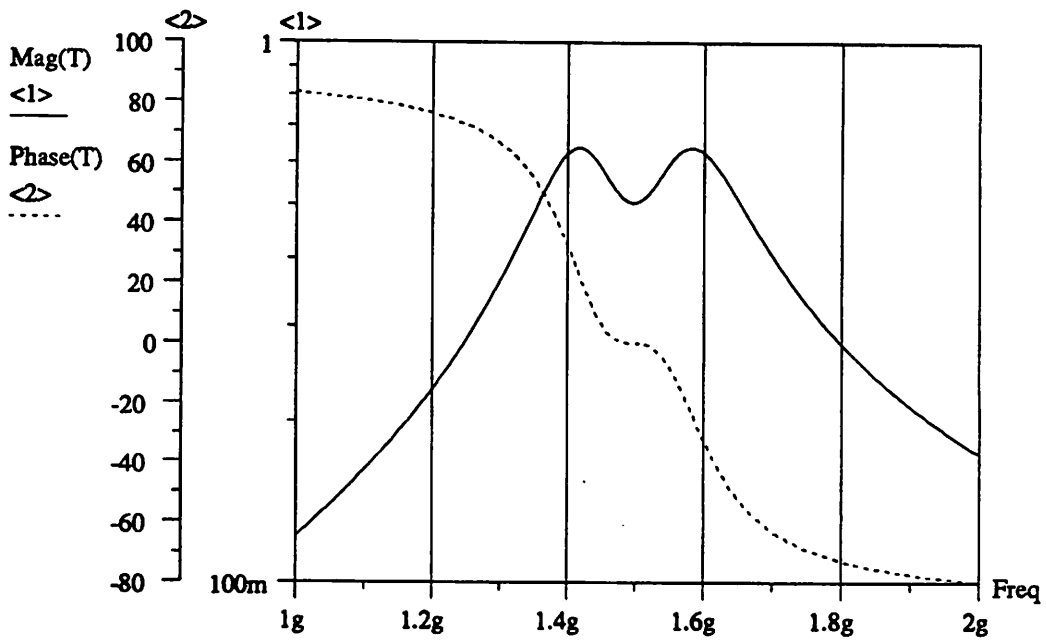
where

$$\omega_C = \frac{\omega_1 + \omega_2}{2}. \quad (6.3)$$

It has been determined that the relationship (6.2) gives the allowable tuning range for this circuit; any further separation than this can result in the multi-oscillation phenomenon discussed in Chapter 3. The



(a) $Q = 10, \omega_c = 1.50 \text{ GHz}, \omega_1 = \omega_c \left[1 - \frac{1}{2Q} \right], \omega_2 = \omega_c \left[1 + \frac{1}{2Q} \right]$



(b) Resultant Loop Gain

Figure 6.3

resultant loop gain for $\alpha_1 = \alpha_2 = \frac{1}{2}$ is shown in Fig. 6.3(b). We note that the effective zero-phase frequency is between ω_1 and ω_2 . By varying α_1 from 1 to 0 while maintaining the constraint $\alpha_1 + \alpha_2 = 1$, we achieve a zero-phase frequency that varies from ω_1 to ω_2 . Note that no varactor is needed in this circuit for frequency tuning.

In the following paragraphs we confirm the simulation results of Fig. 6.3(b). It can be shown that the loop gain has the form of (a more elaborate derivation is given in Section 6.3)

$$T(s) = \alpha_1 T_{\max} \left[\frac{s \frac{L_1}{R_1}}{s^2 L_1 C_x + s \frac{L_1}{R_1} + 1} \right] + \alpha_2 T_{\max} \left[\frac{s \frac{L_2}{R_2}}{s^2 L_2 C_y + s \frac{L_2}{R_2} + 1} \right] \quad (6.4)$$

where it is assumed that $T_1(s)$ and $T_2(s)$ have the same maximum gain. It is useful to define the following quantities

$$Q_1 = R_1 \sqrt{\frac{C_x}{L_1}} \quad (6.5)$$

$$Q_2 = R_2 \sqrt{\frac{C_y}{L_2}} \quad (6.6)$$

$$\omega_1 = \frac{1}{\sqrt{L_1 C_x}} \quad (6.7)$$

$$\omega_2 = \frac{1}{\sqrt{L_2 C_y}}. \quad (6.8)$$

Using the above definitions in (6.4) and replacing $s = j\omega$ gives

$$T(\omega) = \alpha_1 T_{\max} \left[\frac{1}{1 + jQ_1 \left[\frac{\omega}{\omega_1} - \frac{\omega_1}{\omega} \right]} \right] + \alpha_2 T_{\max} \left[\frac{1}{1 + jQ_2 \left[\frac{\omega}{\omega_2} - \frac{\omega_2}{\omega} \right]} \right]. \quad (6.9)$$

$$= \alpha_1 T_{\max} |e^{j\theta_1}| + \alpha_2 T_{\max} |e^{j\theta_2}|.$$

For $Q_1 = Q_2 \equiv Q = 10$, the values of $|e^{j\theta_1}|$ and $|e^{j\theta_2}|$ as functions of frequency are given in Table 6.1.

$$\omega_c = \omega_2 = \left[\frac{1 + \frac{2\sigma}{1}}{1} \right] \omega_2 \approx \omega_2 \left[1 - \frac{2\sigma}{1} \right] \quad (6.13)$$

and

$$\omega_c = \omega_1 = \left[\frac{1 - \frac{2\sigma}{1}}{1} \right] \omega_1 \approx \omega_1 \left[1 + \frac{2\sigma}{1} \right] \quad (6.12)$$

We also express quantity ω_c in terms of ω_1 and ω_2 , respectively. Combining (6.2) and (6.3) gives

$$f(x) = \frac{1+x}{1-x} \approx 1 - 2x \quad \text{for } x \ll 1.$$

where the following approximation has been used

$$\omega_2 = \omega_1 \left[\frac{1 + \frac{2\sigma}{1}}{1 - \frac{2\sigma}{1}} \right] \approx \omega_1 \left[1 + \frac{\sigma}{1} \right] \quad (6.11)$$

and

$$\omega_1 = \omega_2 \left[\frac{1 - \frac{2\sigma}{1}}{1 + \frac{2\sigma}{1}} \right] \approx \omega_2 \left[1 - \frac{\sigma}{1} \right] \quad (6.10)$$

combining (6.2) and (6.3) we obtain

To facilitate subsequent calculations, we express quantity ω_i in terms of ω_2 and vice versa. By

Table 6.1: $\sigma = 10$; t denotes either 1 or 2

ω	$\omega_i (1 - \frac{1}{\sigma})$	$\omega_i (1 + \frac{2\sigma}{1})$	$\omega_i (1 + \frac{1}{\sigma})$
$ \epsilon^{j\theta} $.428 $e^{j64.7}$.698 $e^{j45.7}$	1.0
		.716 $e^{-j44.3}$.464 $e^{-j62.4}$

where the following approximation has been used

$$f(x) = \frac{1}{1-x} \approx 1+x \quad \text{for } x \ll 1.$$

We now evaluate the loop gain (6.9) at frequencies ω_1 , ω_C , and ω_2 . For $\alpha_1 = \alpha_2 = \frac{1}{2}$, the effective loop gain evaluated at ω_1 using (6.10-6.13) and Table 6.1 is

$$\begin{aligned} T(\omega_1) &= \frac{1}{2} T_{\max} \left[|e^{j\theta_1}|_{\omega=\omega_1} + |e^{j\theta_2}|_{\omega=\omega_2(1-\frac{1}{Q})} \right] \\ &= \frac{1}{2} T_{\max} \left[1.0 + .428 e^{j64.7^\circ} \right] = \frac{1.24}{2} T_{\max} e^{j18.1^\circ}. \end{aligned} \quad (6.14)$$

Similarly,

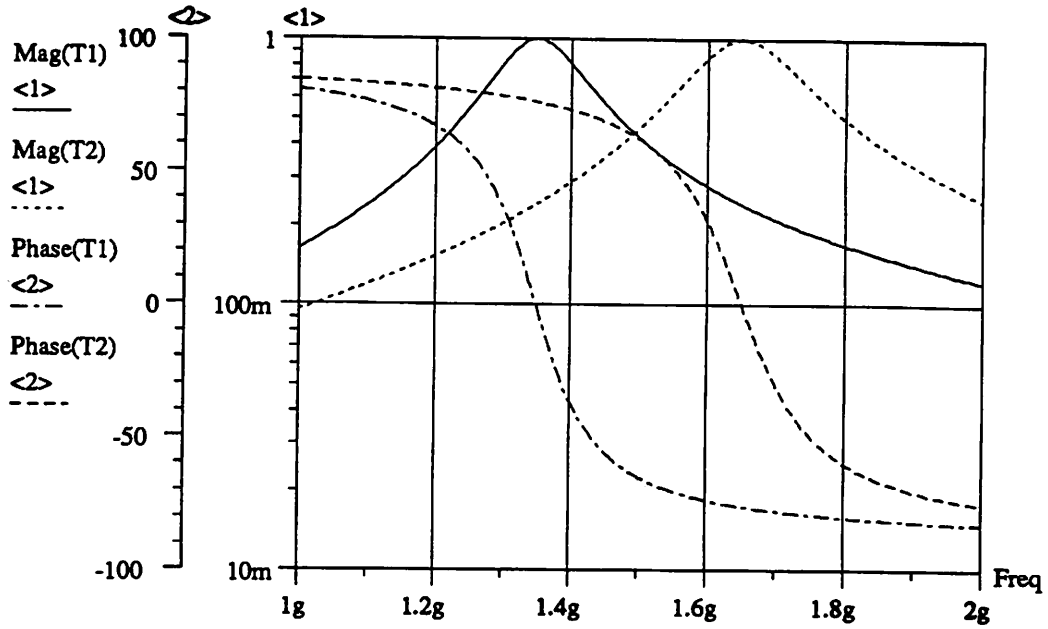
$$\begin{aligned} T(\omega_C) &= \frac{1}{2} T_{\max} \left[|e^{j\theta_1}|_{\omega=\omega_1(1+\frac{1}{2Q})} + |e^{j\theta_2}|_{\omega=\omega_2(1-\frac{1}{2Q})} \right] \\ &= \frac{1}{2} T_{\max} \left[.716 e^{-j44.3^\circ} + .698 e^{j45.7^\circ} \right] \approx \frac{1}{2} T_{\max} \end{aligned} \quad (6.15)$$

$$\begin{aligned} T(\omega_2) &= \frac{1}{2} T_{\max} \left[|e^{j\theta_1}|_{\omega=\omega_1(1+\frac{1}{Q})} + |e^{j\theta_2}|_{\omega=\omega_2} \right] \\ &= \frac{1}{2} T_{\max} \left[.464 e^{-j62.4^\circ} + 1.0 \right] = \frac{1.28}{2} T_{\max} e^{-j18.7^\circ}. \end{aligned} \quad (6.16)$$

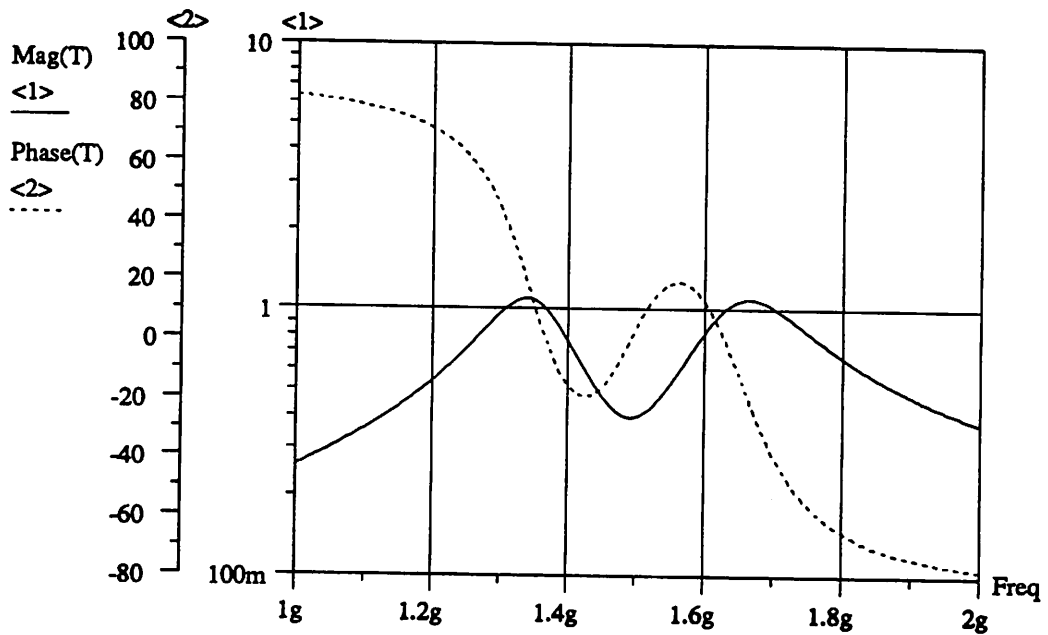
The above analysis agrees well with the simulated results. For $\alpha_1 = \alpha_2 = \frac{1}{2}$, the zero-phase frequency is approximately equal to ω_C according to (6.15). As α_1 varies from 1 to 0 and α_2 varies from 0 to 1, it can be shown that the effective loop gain of the circuit decreases from T_{\max} at ω_1 , reaches the minimum value of $T_{\max} / 2$ at ω_C , and increases back to T_{\max} at ω_2 .

6.2.2. Frequency Variation

We observe from the above analysis that if $\omega_2 - \omega_1 = \omega_C / Q$, the effective frequency variation is



(a) $Q = 10$, $\omega_c = 1.50 \text{ GHz}$, $\omega_1 = \omega_c \left[1 - \frac{1}{Q} \right]$, $\omega_2 = \omega_c \left[1 + \frac{1}{Q} \right]$



(b) Resultant Loop Gain

Figure 6.4

approximately $\pm \frac{1}{2Q}$ with respect to ω_C [Eqns. (6.12) and (6.13)]. For a Q of 10, the tuning range is $\pm 5\%$ of the center frequency. If wide tuning bandwidth is desired, the tank-circuit Q should be reduced. We now determine whether it is plausible to separate the frequencies ω_1 and ω_2 further apart in order to achieve a tuning bandwidth wider than ω_C / Q . Figures 6.4(a) and 6.4(b) show the loop gains of the two Colpitts oscillators and the resultant loop gain for the case $\omega_2 - \omega_1 = \frac{\omega_C}{0.5 Q}$. From Fig. 6.4(b) we observe that the multi-oscillation phenomenon can occur since the non-monotonic phase function crosses the zero point at multiple frequencies. The Nyquist diagram (not shown) corresponding to the characteristic of Fig. 6.4(b) reveals that given a sufficient T_{\max} , there can be more than two natural frequencies in the right-half plane which give rise to multiple expanding signals.

In conclusion, the relationship $\omega_2 - \omega_1 = \omega_C / Q$ gives the allowable tuning range for this circuit.

6.3. Loop-Gain Derivation and Root Loci

We now confirm the relationship (6.1). The simplified ac circuit schematic of the VCO is shown in Fig. 6.5. If we break the circuit at the common emitter node shared by transistors Q_5 and Q_6 and apply a test signal, this signal would traverse through the left and right oscillators along the paths numbered from #1 to #4 and from #a to #d, respectively. The block diagram of the paths is shown in Fig. 6.6. Upon traversing through the loops, the two signals return to the emitter node of Q_5 and Q_6 and are added up due to the summing property of the emitter-coupled pair. This rather unique property has been observed and derived from a varactor-tuned multivibrator circuit configuration [Duc89].

In the following paragraphs we derive the effective loop gain of the VCO. The simplified ac circuit of the left Colpitts oscillator is given in Fig. 6.7 where for ease of analysis, the base of the transistor Q_5 is assumed grounded. Under this assumption we can show that

$$\frac{dI_1}{dV_1} = \frac{g_{m5}}{2} = \frac{g_{m6}}{2} \equiv G_m \quad (6.17)$$

and the approximate impedance looking into the base of Q_6 is $\frac{C_{\pi 5}}{2} = \frac{C_{\pi 6}}{2} \equiv \frac{C_{\pi}}{2}$. Figure 6.8 shows the

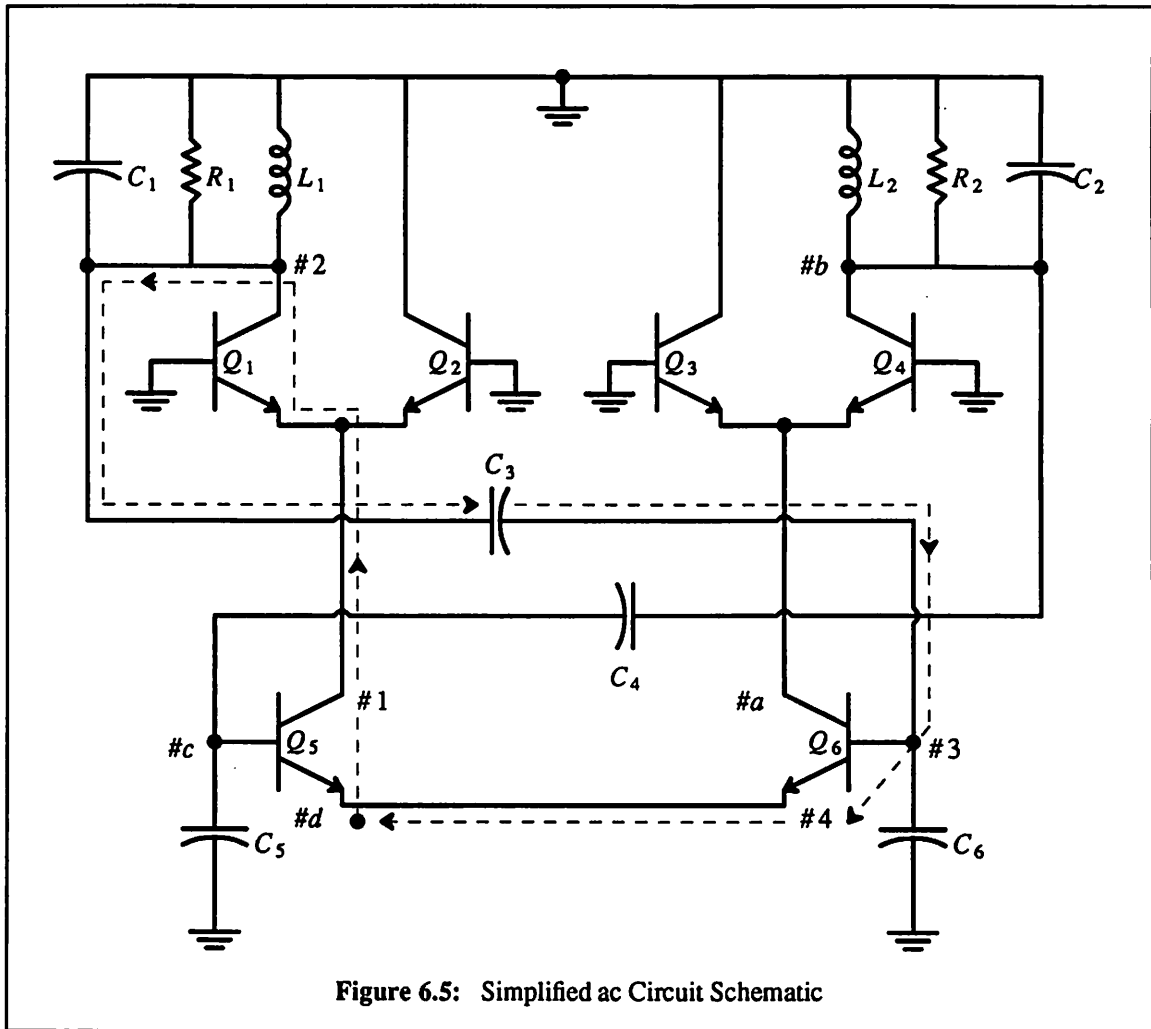


Figure 6.5: Simplified ac Circuit Schematic

simplified equivalent circuit for deriving the loop gain $T_1(s)$. It can be shown that

$$T_1(s) = G_m \left[\frac{sL_1}{s^2L_1C_x + s\frac{L_1}{R_1} + 1} \right] \left[\frac{C_3}{C_3 + \frac{C_\pi}{2} + C_6} \right] \quad (6.18)$$

where

$$C_x = C_1 + \left[C_3 \parallel \left[\frac{C_\pi}{2} + C_6 \right] \right]. \quad (6.19)$$

It is useful to define

$$n_1 = \left[\frac{C_3 + \frac{C_\pi}{2} + C_6}{C_3} \right] \quad (6.20)$$

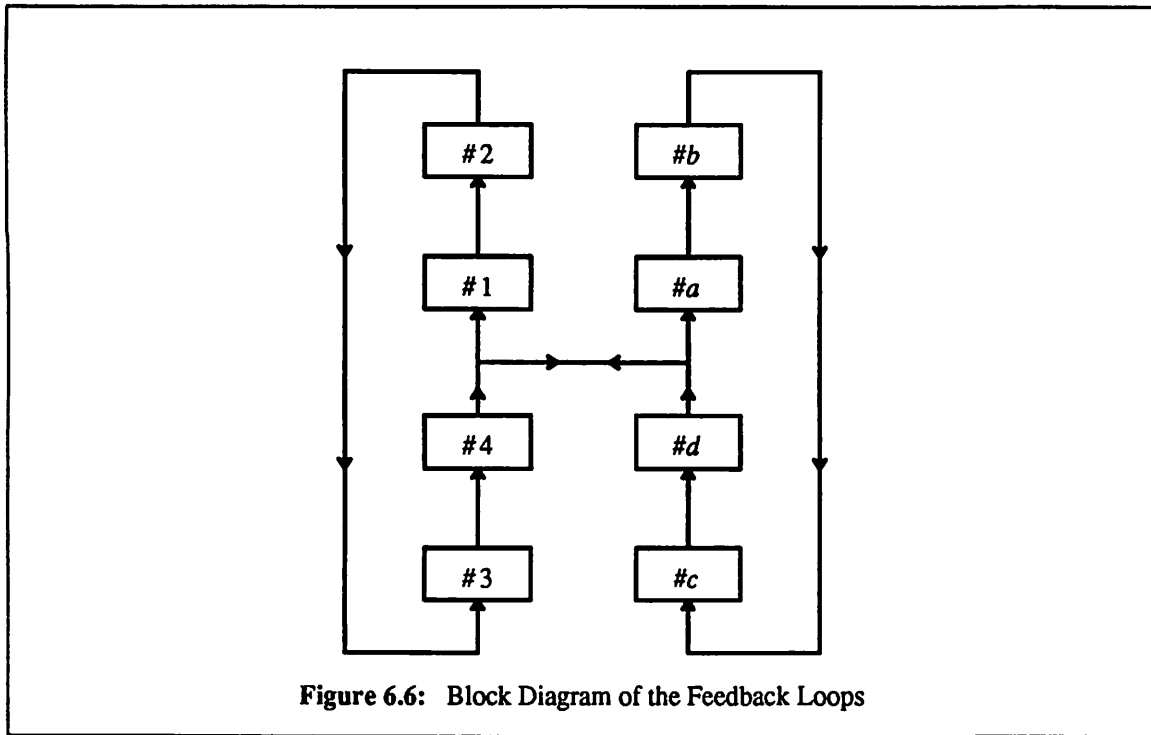


Figure 6.6: Block Diagram of the Feedback Loops

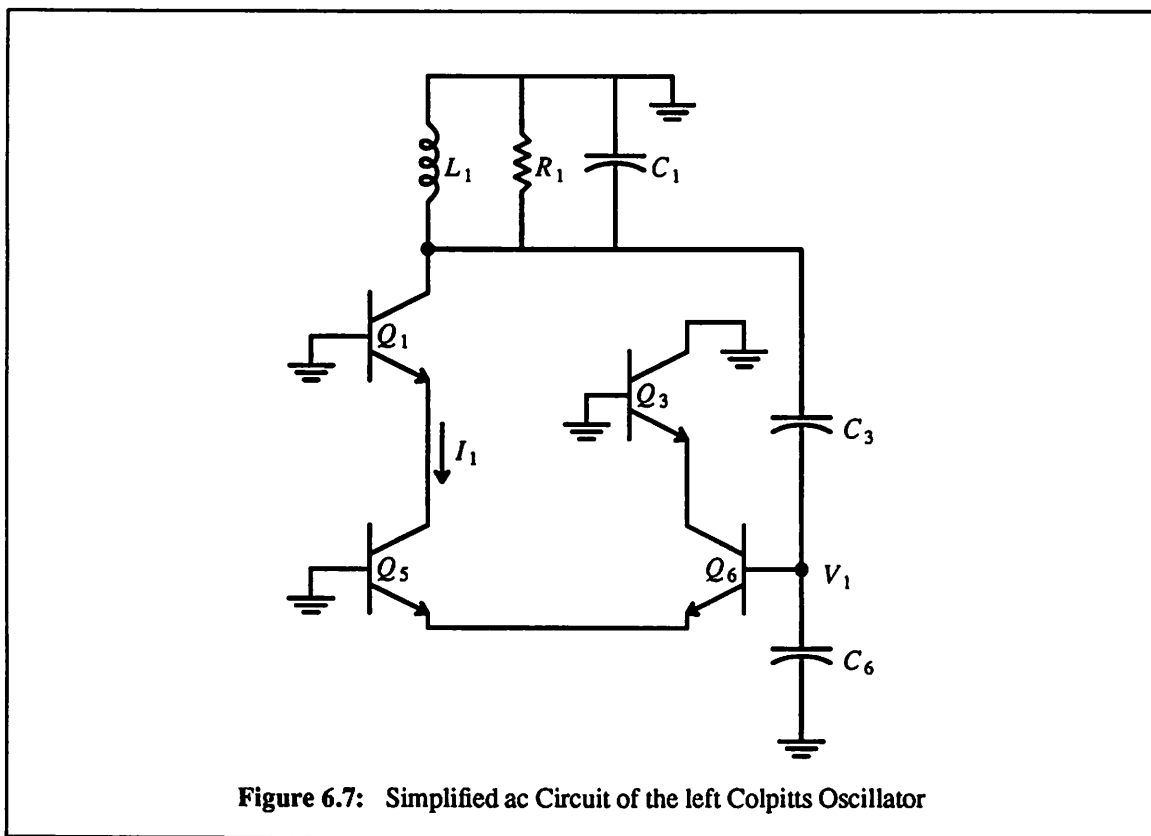
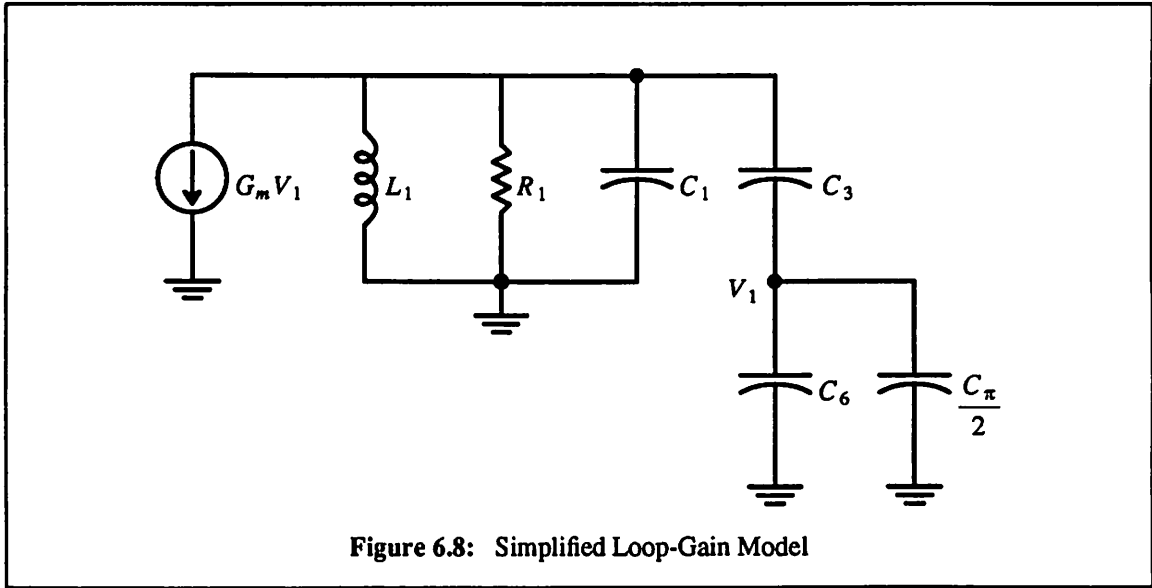


Figure 6.7: Simplified ac Circuit of the left Colpitts Oscillator



$$T_{\max 1} = \left[\frac{G_m R_1}{n_1} \right] \quad (6.21)$$

Using the definitions (6.20) and (6.21) in (6.18) gives

$$T_1(s) = T_{\max 1} \left[\frac{s \frac{L_1}{R_1}}{s^2 L_1 C_x + s \frac{L_1}{R_1} + 1} \right] \quad (6.22)$$

In similar fashion, we can derive the loop gain $T_2(s)$. It is equal to

$$T_2(s) = T_{\max 2} \left[\frac{s \frac{L_2}{R_2}}{s^2 L_2 C_y + s \frac{L_2}{R_2} + 1} \right] \quad (6.23)$$

where

$$C_y = C_2 + \left[C_4 \parallel \left[\frac{C_\pi}{2} + C_5 \right] \right] \quad (6.24)$$

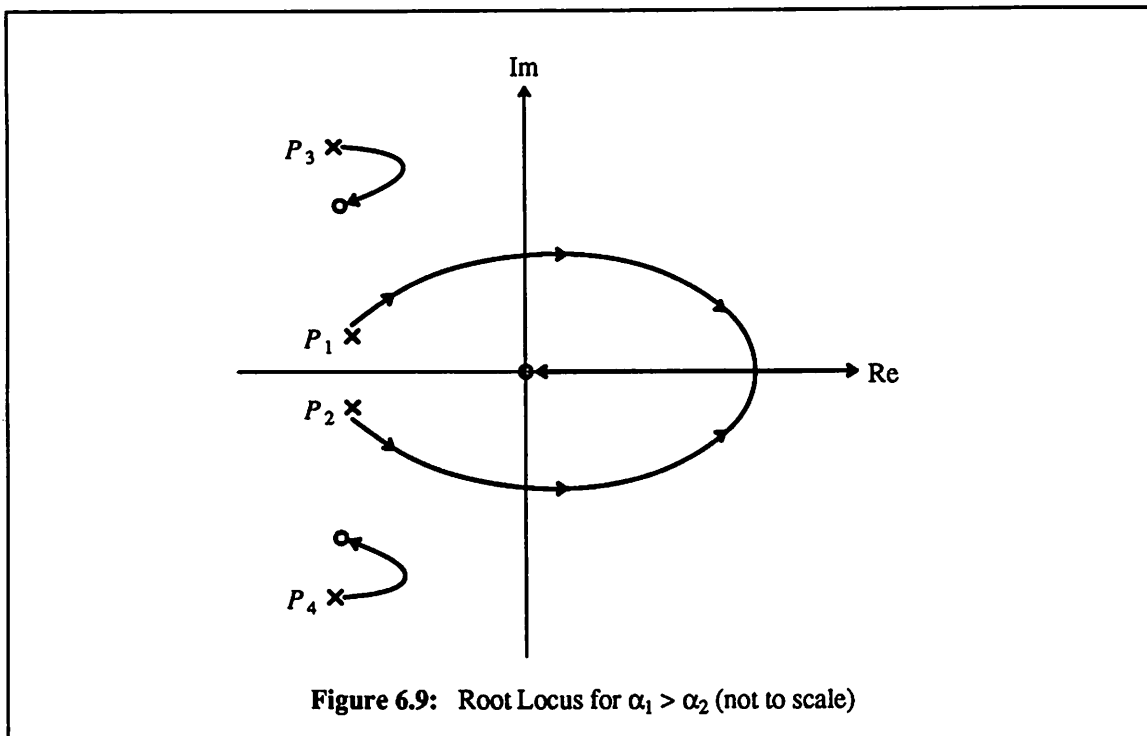
$$n_2 = \left[\frac{C_4 + \frac{C_\pi}{2} + C_5}{C_4} \right] \quad (6.25)$$

$$T_{\max 2} = \left[\frac{G_m R_2}{n_2} \right]. \quad (6.26)$$

The effective loop gain of the circuit is

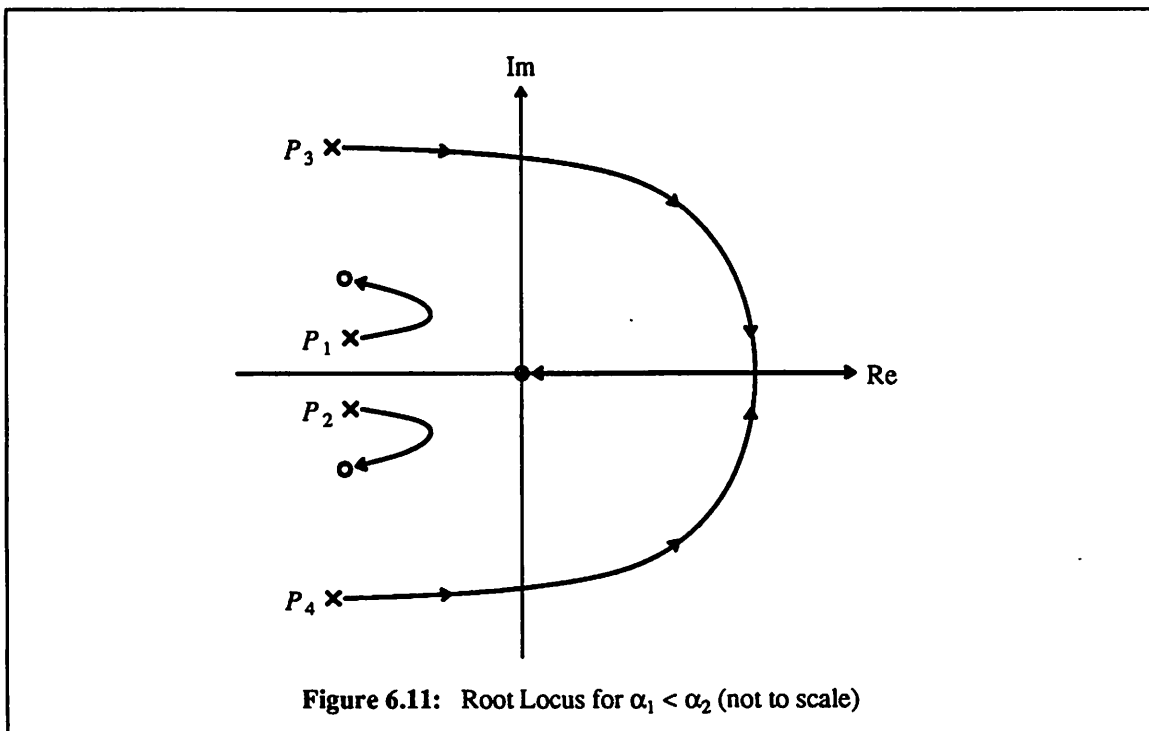
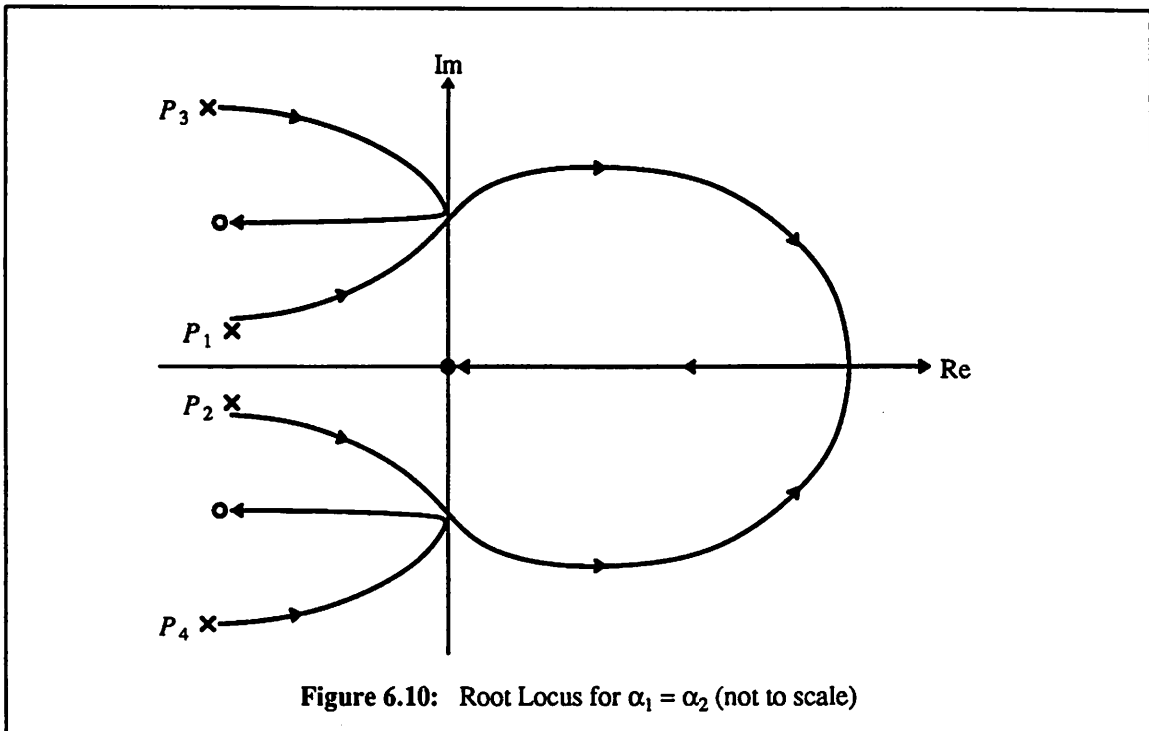
$$T(s) = \alpha_1 T_1(s) + \alpha_2 T_2(s). \quad (6.27)$$

According to (6.21) and (6.26), the two Colpitts oscillators have the same maximum loop gain T_{\max} if $R_1 / n_1 = R_2 / n_2$. Quantity T_{\max} should be chosen to be about 6 so that the loop gain has a minimum value of about 3 [Eqn. (6.15)]. This is sufficiently large for ensuring a reliable oscillation start-up when subject to temperature changes and power-supply fluctuations in a practical implementation.



We now construct the root loci for the circuit from the characteristic equation $1 - T(s) = 0$. The root loci for $\alpha_1 > \alpha_2$, $\alpha_1 = \alpha_2$, and $\alpha_1 < \alpha_2$ are given in Figures 6.9, 6.10, and 6.11, respectively. In these figures, the natural frequencies P_1 and P_2 are contributed by $T_1(s)$ and the natural frequencies P_3 and P_4 (at relatively higher frequencies) are contributed by $T_2(s)$. We note that with sufficient loop gain, the circuit always has a unique pair of RHP natural frequencies. The oscillation build-up is expected to be well behaved. These root loci also indicate that for $\alpha_1 \geq \alpha_2$, the oscillation behavior is

determined mainly by the left Colpitts oscillator; whereas for $\alpha_1 < \alpha_2$, it is determined mainly by the right Colpitts oscillator.

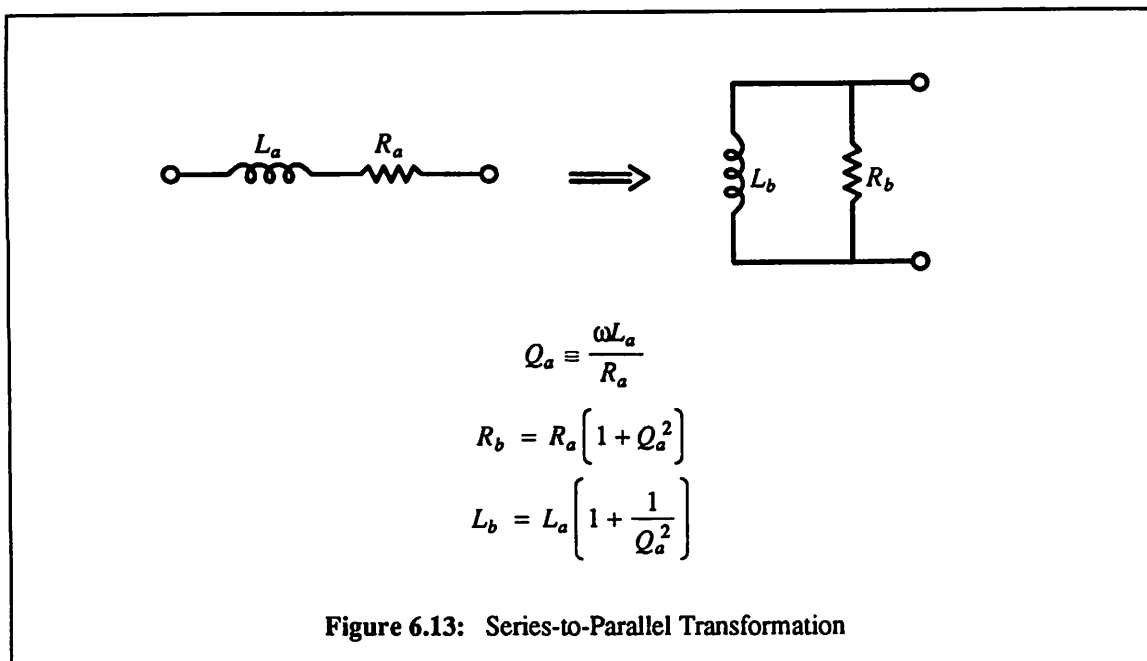


6.4. Circuit Implementation and Performance

A monolithic LC VCO has been realized which achieves a simulated tuning range of 300 MHz extending from 1.5 GHz to 1.8 GHz. The center frequency of the VCO is approximately 1.65 GHz. For a tank-circuit Q of 5, the tuning range is $\pm 10\%$ of the center frequency. The complete circuit is shown in Fig. 6.12. The input differential pair Q_7 and Q_8 converts a single-ended input signal to a differential output signal which is used to control the amount of bias current I_Q that drives the transistors Q_1 and Q_4 . Resistor R_5 sets the proper bias voltage for the succeeding stage. Resistors R_3 and R_4 are used to improve the linear input range for V_{IN} . The differential pair Q_{21} and Q_{22} forms an output amplifier with resistance value R_{17} chosen to be equal to the system impedance of 50Ω . Transistors Q_1 to Q_6 form the core of the VCO. Important element values are $L_1 = 6.5$ nH, $C_1 = 0.2$ pF, $C_3 = 1.0$ pF, $C_6 = 3.0$ pF, $L_2 = 3.7$ nH, $C_4 = 1.6$ pF, and $C_5 = 1.0$ pF. Parasitic elements associated with inductors L_1 and L_2 are used to replace capacitor C_2 and resistors R_1 and R_2 of Fig. 6.2. Recall from Chapter 5 that parasitic elements associated with a silicon integrated inductor include the sheet resistance R_s , parasitic capacitance C_p from the metal layers to the substrate, and substrate resistance R_p . The set $\{R_s, C_p, R_p\}$ for L_1 is approximately $\{9.9 \Omega, 460$ fF, $70 \Omega\}$ and for L_2 is approximately $\{5.8 \Omega, 450$ fF, $50 \Omega\}$. The network transformation in Fig. 6.13 is used to convert the series L_s - R_s branch of the inductor equivalent circuit into a parallel network.

In the preceding sections, the natural frequencies due to the resonant circuits have been assumed to be dominant. At high frequencies, other less significant natural frequencies in the active transistors can produce excess phase shift and cause significant loop gain loss. This effect is more eminent in the right Colpitts oscillator since it must operate at higher frequencies than the left Colpitts oscillator. For this reason, the ratio n_2 was intentionally chosen to be less than n_1 so as to compensate for the loop gain loss [Eqn. (6.26)].

The nominal bias current I_Q is 10 mA. Diodes D_1 - D_5 form protection circuits against electrostatic discharges. The simulated quiescent power dissipation is 95 mW from a single supply of 5 V. The VCO is simulated assuming the 3σ limits of $\pm 10\%$ on the capacitance values. When subject to these process



variations, the frequency tuning range is observed to vary at less than $\pm 3\%$, indicating that the circuit is insensitive to process variations. This is intuitively expected since the oscillation frequency is inversely proportional to the square root of the LC time constant. Figure 6.14 displays the oscillation frequency as a function of the controlling voltage V_{IN} .

The steady-state condition for feedback oscillators is described by the so-called Barkhausen criterion which states that the “large-signal” loop gain evaluated at the oscillation frequency and amplitude is equal to one, i.e., $T^{(1)}(\omega_o, A_o) = 1$. It is important to emphasize that one must utilize the concept of the describing function to describe the large-signal loop gain quantity. This VCO circuit achieves its steady-state behavior through distortion limiting due to the active transistors Q_1 and Q_4 . As the oscillation frequency varies from ω_1 to ω_2 , the output signal taken from either the base of Q_5 or the base of Q_6 is not expected to be constant. In fact, the signal V_{o2} decreases from its peak value at ω_1 and reaches a minimum value at ω_2 . This is expected since as the oscillation frequency increases, the effective “large-signal” impedance at the collector of Q_1 decreases; the output signal is reduced accordingly. The signal V_{o1} behaves oppositely from the signal V_{o2} . In order to maintain a somewhat constant amplitude of oscillation over the whole tuning bandwidth, it is necessary to use the differential output signal between V_{o1}

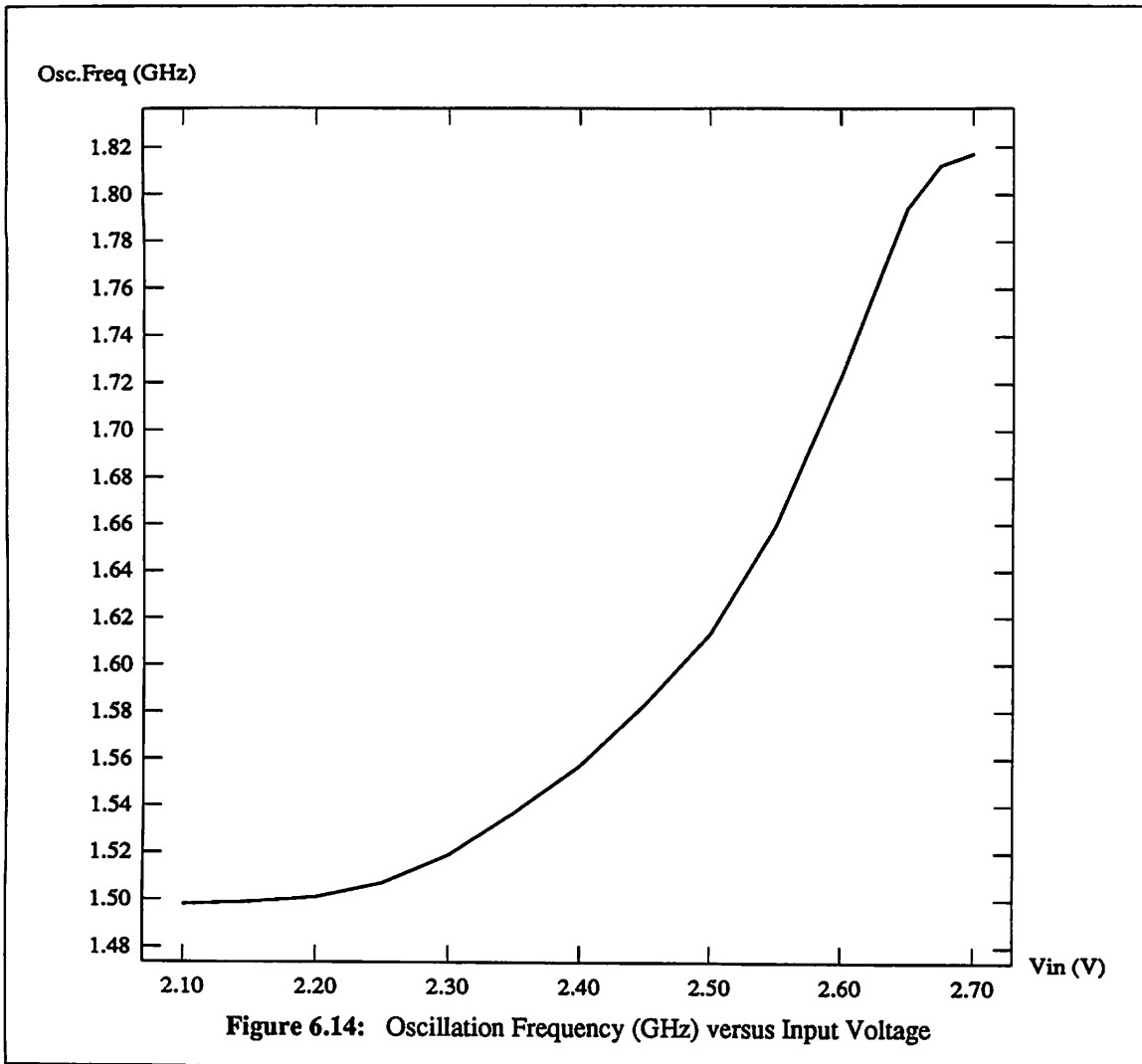
and V_{o2} .

The oscillator was fabricated in an oxide-isolated BiCMOS IC process with typical f_T (npn) = 10 GHz. Preliminary testing of the circuit in package form showed circuit performance close to the simulated results. Further characterization on the oscillator phase noise and the voltage-to-oscillation translation has been planned. Since the oscillator phase noise is inversely proportional to the square of the oscillator Q [Rob82], good phase noise performance can be achieved at the expense of a narrow tuning bandwidth.

6.5. Conclusion

A monolithic microwave sinusoidal LC voltage-controlled oscillator (VCO) has been described. Unlike conventional sinusoidal VCOs that must depend on a varactor for frequency tuning, this VCO uses two cross-coupled Colpitts oscillators to achieve the objective. The obtainable tuning bandwidth is $\omega_2 - \omega_1 = \omega_C / Q$ where ω_1 and ω_2 are the oscillation frequencies of the stand-alone Colpitts oscillators.

Simulation results indicate that the circuit is insensitive to process tolerances and temperature variations. This VCO can be used in a high-frequency phase-locked loop for various communication applications.



Chapter 7 - Si Bipolar Monolithic RF Bandpass Amplifiers

7.1. Introduction

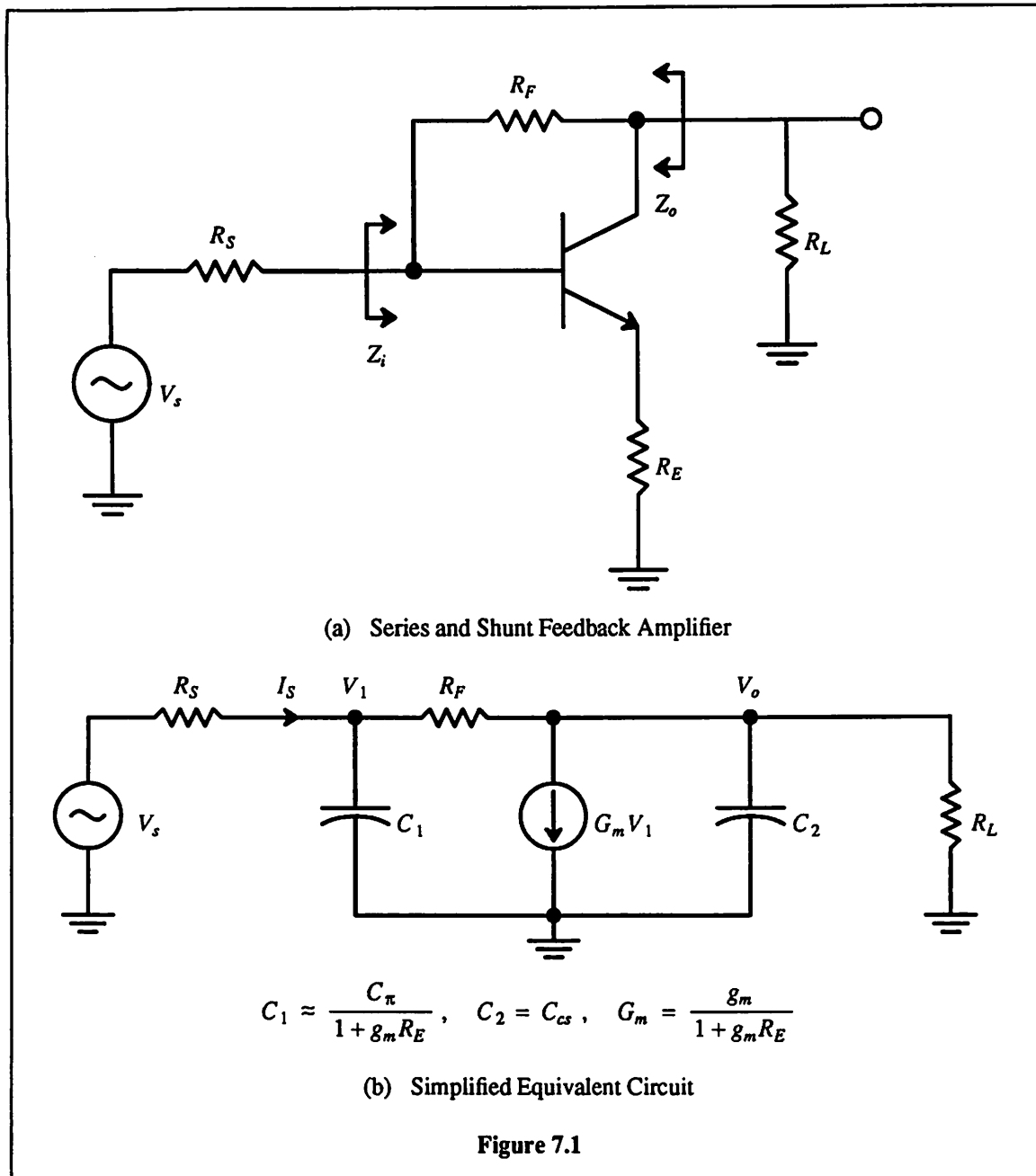
RF amplifiers are widely used in many RF communication systems. Important characteristics include gain per stage, frequency response and noise performance. Resistive feedback amplifiers are often used to achieve the above objectives [Mey81, Pet83]. In the frequency range extending from dc to the -3 -dB frequency, these amplifiers achieve simultaneous input and output impedance match, while maintaining flat gain and relatively low amplifier noise. Beyond the -3 -dB frequency, the circuit noise increases as the circuit gain drastically reduces and the terminal impedances are severely mismatched. The performance of such circuits can be optimized for use with band-limited RF signals by focusing on the passband of interest. In this chapter we investigate the application of monolithic inductors in the design and fabrication of Si monolithic RF amplifiers in the L band (1-2 GHz). The inductors are used to boost the gain of the RF amplifiers and to improve noise performance.

As a test vehicle, a bipolar monolithic bandpass amplifier has been fabricated, measured, and characterized. A 4-nH silicon integrated inductor was used to achieve a peak S_{21} gain of 8 dB, a simulated noise figure of 6.4 dB, and a matched input impedance of 50Ω in the frequency range 1-2 GHz. The amplifier was fabricated in an oxide-isolated Si bipolar IC process with peak $f_T = 9$ GHz.

7.2. Design Approach

A simplified ac circuit schematic of a widely-used resistive feedback amplifier is shown in Fig. 7.1(a). The circuit incorporates a shunt feedback resistor (R_F) and a series feedback resistor (R_E) to achieve stabilized circuit gain, low output distortion, and simultaneous input and output impedance matching. In order to predict the frequency response of this circuit, the simplified equivalent circuit shown in Fig. 7.1(b) which neglects the effects of C_μ and r_b of the bipolar transistor is used. It can be shown that the transimpedance gain is

$$\frac{V_o(s)}{I_S(s)} = \frac{(1 - G_m R_F) R_L}{(1 + G_m R_L) + s \left[C_1 R_F + (C_1 + C_2) R_L \right] + s^2 C_1 R_F C_2 R_L} \quad (7.1)$$



The denominator of (7.1) can be written as

$$D(s) = \left[1 - \frac{s}{P_1}\right] \left[1 - \frac{s}{P_2}\right] = 1 - s \left[\frac{1}{P_1} + \frac{1}{P_2}\right] + \frac{s^2}{P_1 P_2} = 1 + a_1 s + a_2 s^2. \quad (7.2)$$

If P_1 is a dominant pole, it can be approximated by

$$P_1 \approx -\frac{1}{a_1} = -\frac{1 + G_m R_L}{C_1 R_F + (C_1 + C_2) R_L} = f_{-3\text{dB}}. \quad (7.3)$$

The midband gain of the circuit from (7.1) is

$$A_o = \frac{(1 - G_m R_F) R_L}{1 + G_m R_L} \quad (7.4)$$

Equations (7.3) and (7.4) can be combined to yield the gain-bandwidth product of this circuit. It is approximately equal to

$$GB \equiv A_o f_{-3\text{dB}} \approx \omega_T R_L \quad (7.5)$$

where $\omega_T \approx \frac{g_m}{C_\pi}$ denotes the transition frequency of the bipolar transistor. It is seen from (7.5) that the gain-bandwidth product is a constant quantity, implying that if the -3dB frequency is optimized well into the microwave region, a considerable amount of circuit gain is sacrificed.

For the low-pass amplifier of Fig. 7.1(a) the -3dB frequency is observed to be limited mainly by capacitance C_1 . Beyond the -3dB frequency, the terminal impedances are severely mismatched while the circuit gain is greatly reduced. The performance of such circuits can be optimized for use with band-limited RF signals by focusing on the passband of interest. For the circuit in Fig. 7.1(b), this can be accomplished with the addition of a shunt inductor across capacitor C_1 . Effectively, this inductor transforms the “untuned” low-pass amplifier into a bandpass amplifier.

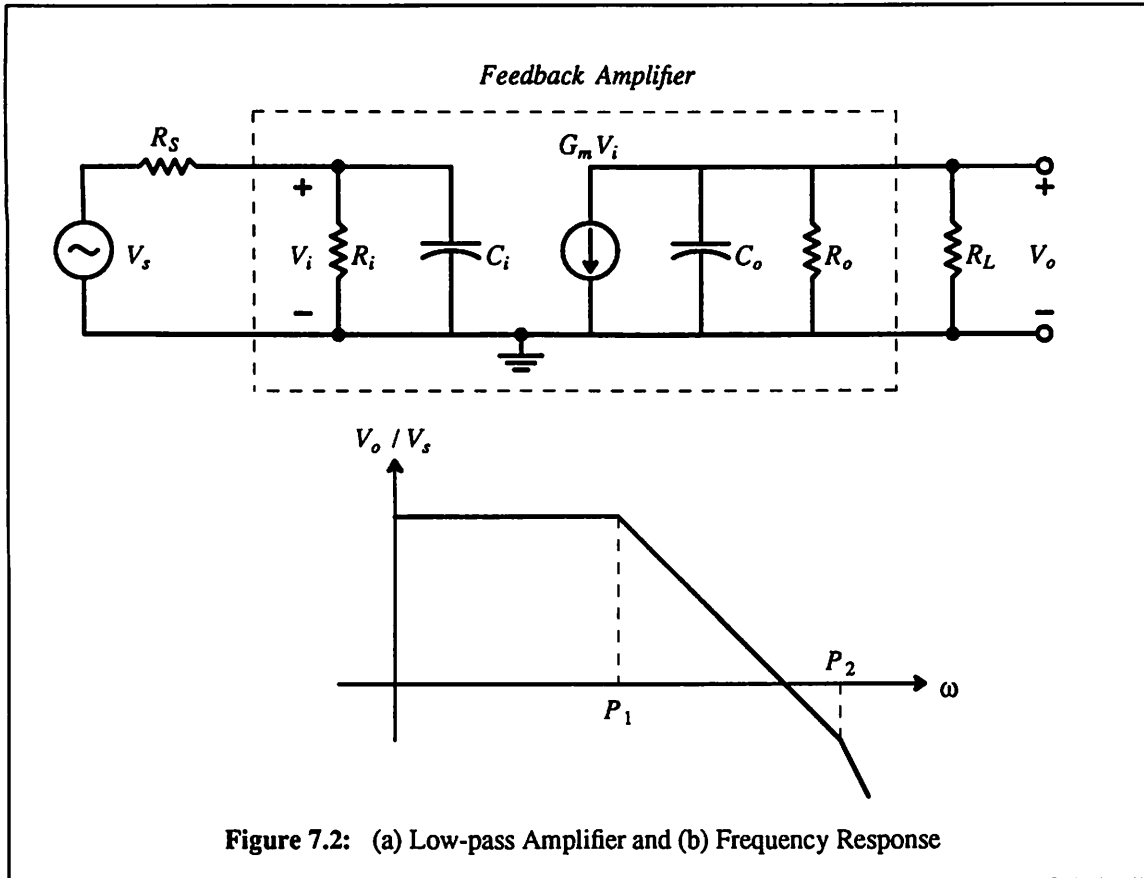
In order to understand how the shunt inductor used in this topology modifies the circuit bandwidth, we first consider the general representation of a low-pass amplifier shown in Fig. 7.2(a). The gain function can be derived to be

$$\frac{V_o(s)}{V_s(s)} = -G_m (R_L \parallel R_o) \frac{R_i}{R_i + R_S} \left[\frac{1}{1 - s/P_1} \right] \left[\frac{1}{1 - s/P_2} \right] \quad (7.6)$$

where

$$P_1 = -\frac{1}{(R_S \parallel R_i) C_i} \quad \text{and} \quad P_2 = -\frac{1}{(R_L \parallel R_o) C_o} \quad (7.7)$$

A typical plot of (7.6) is shown in Fig. 7.2(b) where the assumed dominant pole P_1 determines the bandwidth of the circuit. Since the input resistance R_i must be matched to the source resistance R_S in order to minimize reflected signal loss, quantity C_i dictates the frequency P_1 . We next consider the



modified circuit shown in Fig. 7.3(a). It can be shown that

$$\frac{V_o(s)}{V_s(s)} = -G_m (R_L \parallel R_o) \left[\frac{1}{1 - s/P_2} \right] \left[\frac{s(L_1/R_s)}{s^2 L_1 C_i + s L_1 (1/R_i + 1/R_s) + 1} \right]. \quad (7.8)$$

A typical plot of (7.8) is shown in Fig. 7.3(b). At frequencies well below or above the center frequency $\omega_c (= 1/\sqrt{L_1 C_i})$, the parallel $R_i L_1 C_i$ tank circuit behaves like a short circuit, and consequently, little signal power can be transmitted to the output. Denote the frequencies at which the peak gain drops by 3-dB by ω_- and ω_+ , and the bandwidth of the circuit by $\omega_{-3\text{dB}}$. If $P_2 \gg \omega_+$, it can be shown that [Chu87]

$$\omega_{-3\text{dB}} \equiv \omega_+ - \omega_- = \frac{\omega_c}{Q} \quad (7.9)$$

where

$$Q = (R_s \parallel R_i) \sqrt{\frac{C_i}{L_1}}. \quad (7.10)$$

By substituting (7.10) into (7.9) we obtain

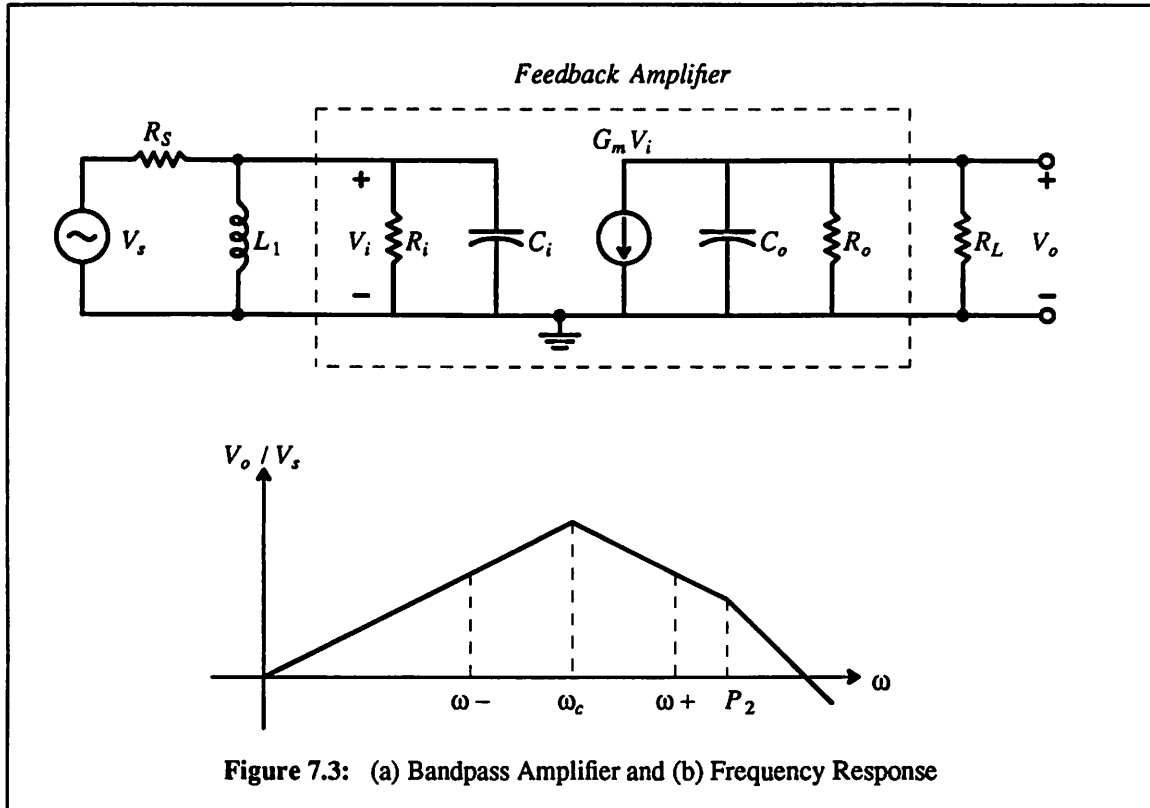


Figure 7.3: (a) Bandpass Amplifier and (b) Frequency Response

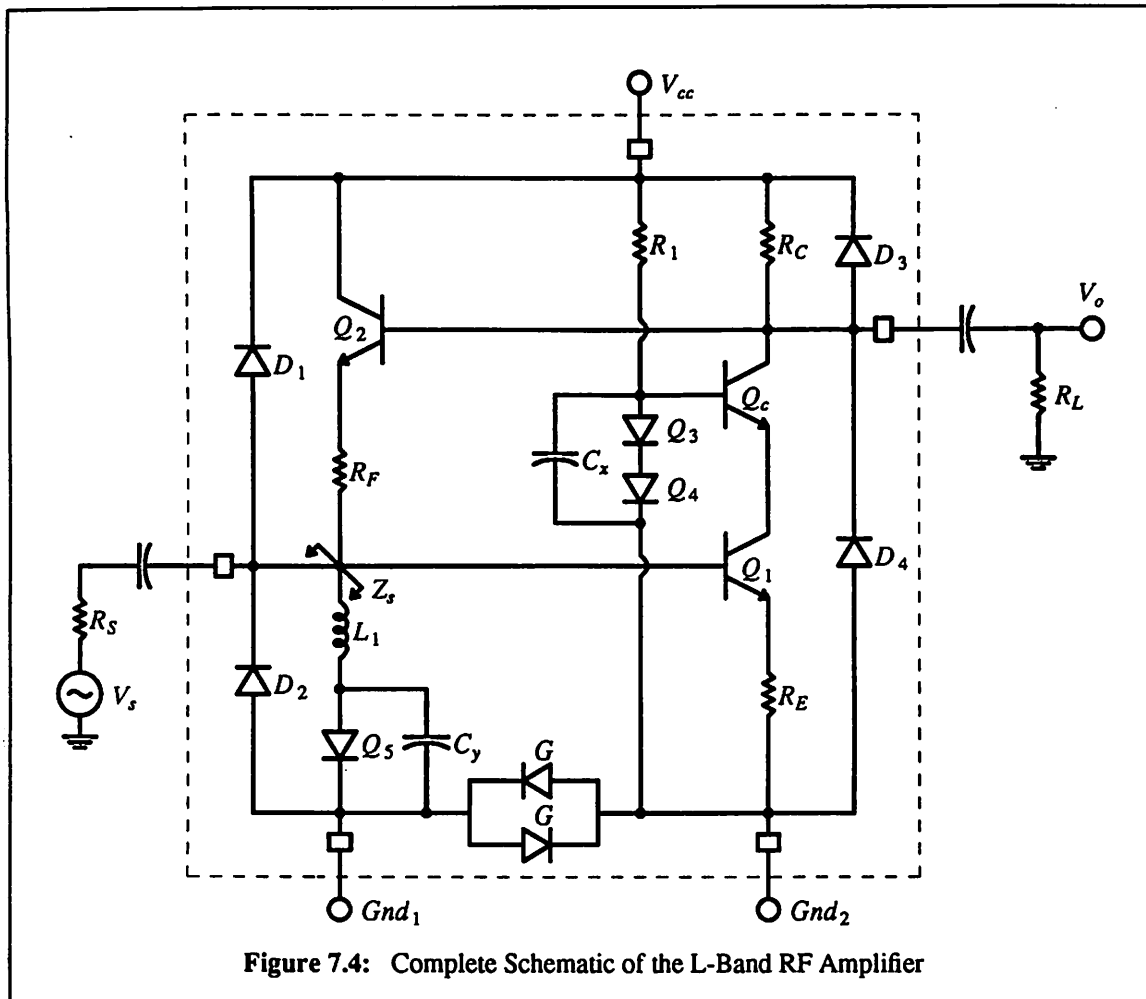
$$\omega_{-3\text{dB}} = \frac{1}{(R_S \parallel R_i) C_i} \quad (7.11)$$

It is interesting to note that the bandwidth of the modified circuit is equal to that of the original circuit.

The new circuit technique effectively transforms a low-pass frequency response to a bandpass response, centered around ω_c . This method is attractive because it achieves the required bandwidth without reducing circuit gain. In addition, it can also achieve a matched input impedance. By tuning out the device capacitance near the center frequency ω_c , the shunt inductor also improves the noise performance at high frequencies. A detailed analysis illustrating this point is presented in Section 7.4.

7.3. Circuit Configuration and Implementation

As an application of the above circuit technique, an L-band (1-2 GHz) bipolar monolithic amplifier has been realized. The complete circuit is shown in Fig. 7.4. Cascode transistor Q_c eliminates the Miller effect resulting from capacitance C_{bc} of transistor Q_1 . Transistor Q_2 functions as a voltage buffer that minimizes forward transmission through the feedback resistor R_F . The only drawback to having the



buffer Q_2 is that simultaneous impedance matching at both the input and output cannot be achieved. For optimum noise performance, R_E and the base resistance of Q_1 must be minimized, and R_F maximized. Diodes D_1 – D_4 function as protection circuit against electrostatic discharges. The amplifier utilizes a 4-nH silicon integrated inductor [Ngu90] to achieve a peak S_{21} gain of 8 dB and a bandwidth of 1.2 GHz that extends from 700 MHz to 1.9 GHz. The input transistor Q_1 is a large device and is fabricated with six $30 \times 2 \mu\text{m}$ base strips, yielding a $17\text{-}\Omega$ base resistance at 6 mA of collector bias current. The measured quiescent power dissipation is 130 mW from a single supply of 10 V.

A die photograph of the amplifier is shown in Fig. 7.5. In order to minimize electrical coupling through the substrate, a buried p-type layer was placed around the I/O pads and around the periphery of critical devices. Measured $|S_{21}|$ and $|S_{11}|$ are shown in Figs. 7.6 and 7.7, respectively. They agree well

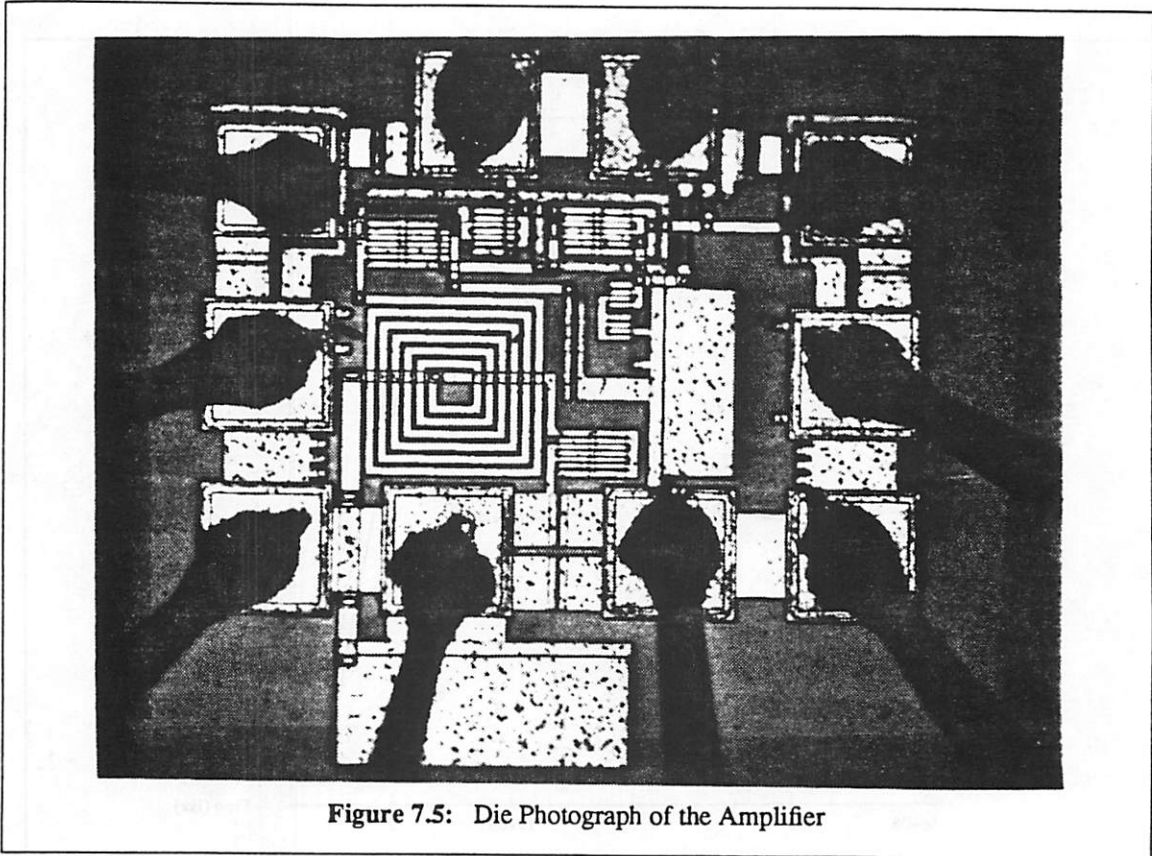


Figure 7.5: Die Photograph of the Amplifier

with the simulated results.

The amplifier's input resistance is matched to a system impedance Z_T of 50Ω with careful selection of R_F and R_E according to the derived relationship

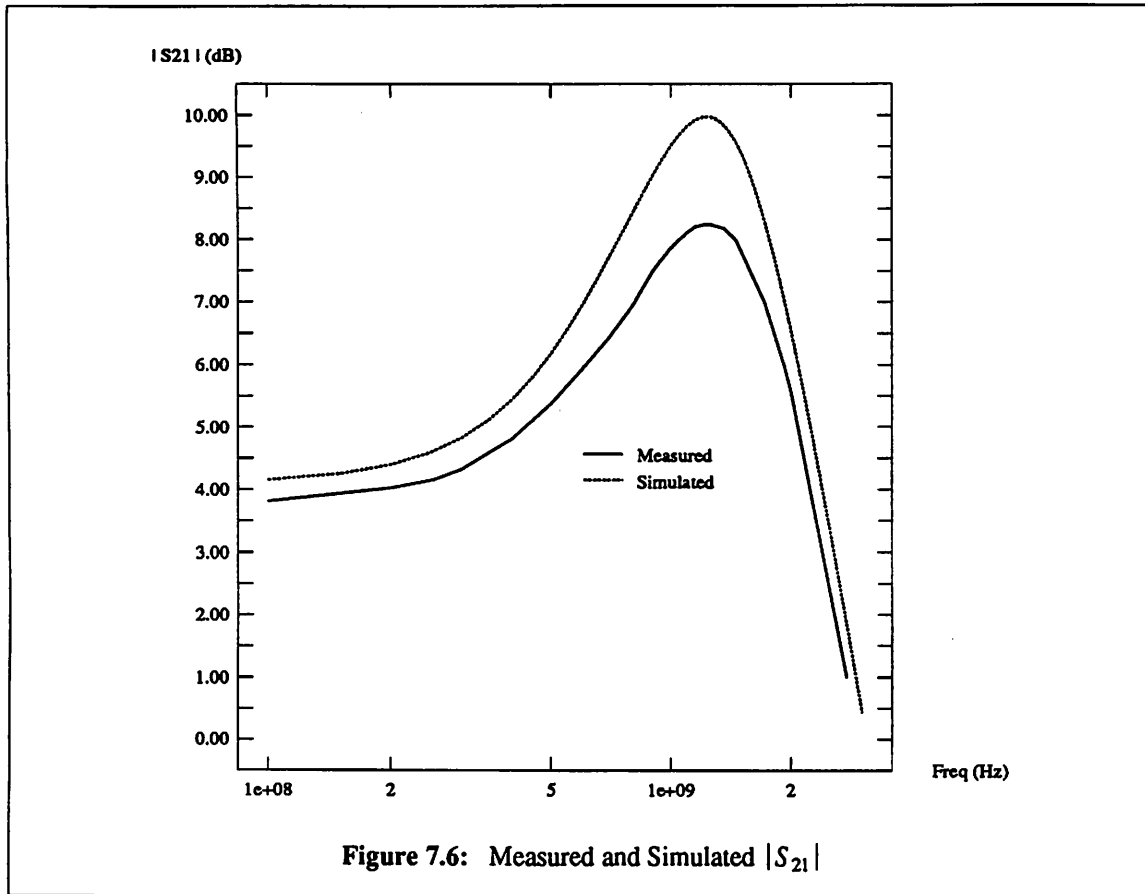
$$R_F = A_V Z_T \quad (7.12)$$

where $A_V \equiv G_m Z_T$, $G_m = \frac{g_{m1}}{1 + g_{m1} R_E}$, and $R_S = R_L = Z_T (= 50 \Omega)$. The circuit bandwidth can be

determined from the untuned amplifier (without L_1) shown in Fig. 7.8. By neglecting the effect of base resistances and by treating the cascode transistor Q_c as a unity current buffer, we can show that the admittance matrix of the two-port amplifier is

$$\begin{bmatrix} Y_{11} & Y_{12} \\ Y_{21} & Y_{22} \end{bmatrix} \approx \begin{bmatrix} \frac{1}{R_F} + sC_1 & -\frac{1}{R_F} \\ -\frac{1}{R_F} \frac{s}{\omega_t} + G_m & \frac{1}{R_F} \frac{s}{\omega_t} + sC_2 \end{bmatrix} \quad (7.13)$$

where



$$C_1 = \frac{C_{\pi 1}}{1 + g_{m1}R_E}$$

$$C_2 = C_{csC} + C_{bcC} + C_{bc2}.$$

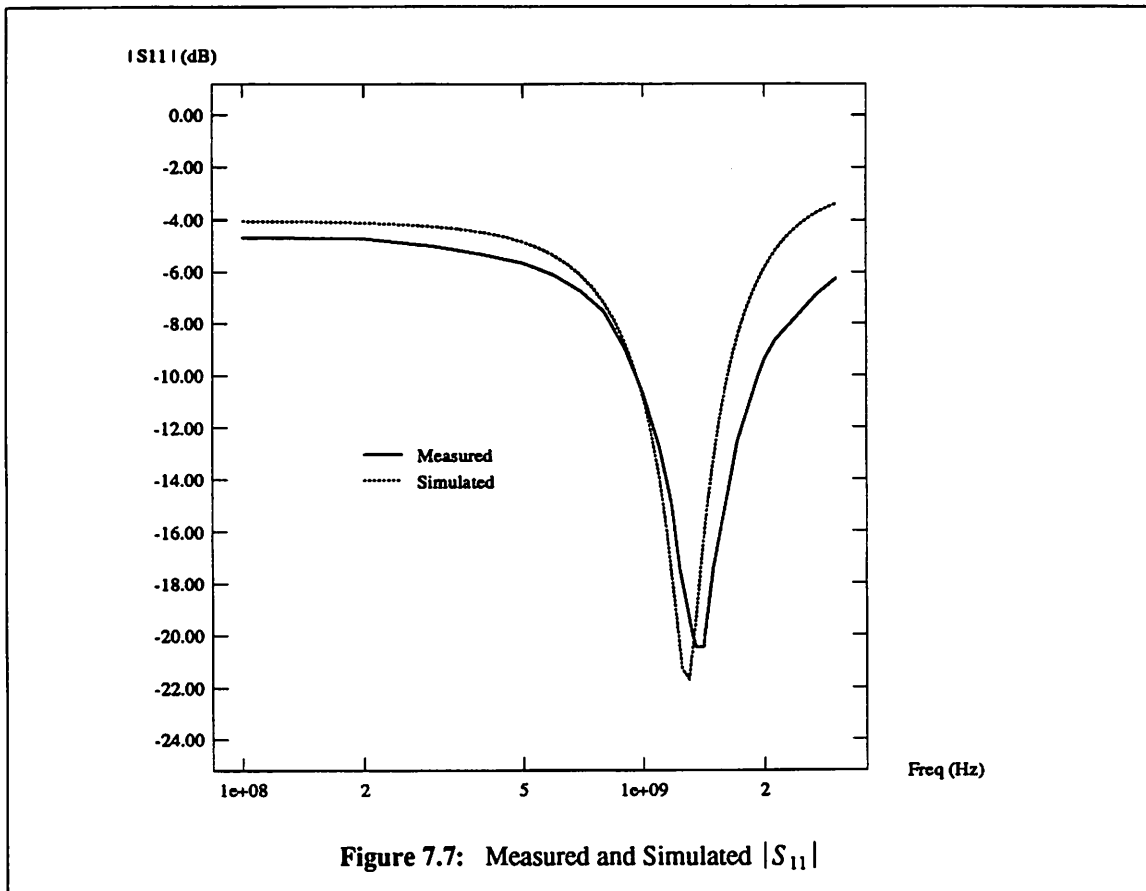
The gain function can be derived to be

$$\frac{V_o(s)}{V_s(s)} = \frac{Y_S Y_{21}}{Y_{12} Y_{21} - (Y_{11} + Y_S)(Y_{22} + Y_L)}$$

$$\approx - \frac{A_V}{s^2 C_1 C_2 Z_T^2 + s Z_T \left[C_1 + C_2 \left(1 + \frac{1}{A_V} \right) \right] + \left(2 + \frac{1}{A_V} \right)}.$$
(7.14)

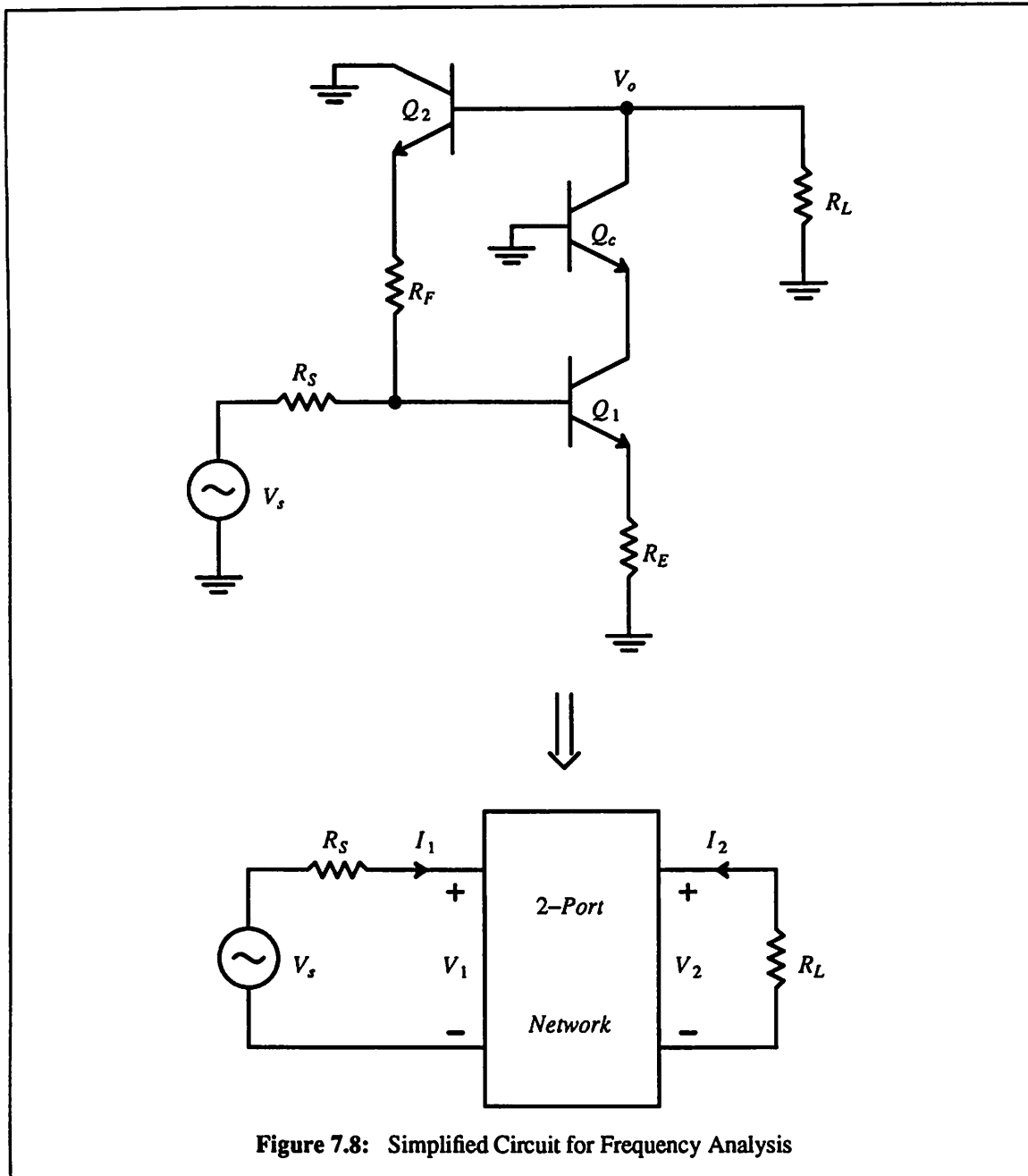
From (7.14), the -3 -dB frequency can be predicted assuming that the transfer function has the dominant pole

$$f_{-3\text{dB}} \approx - \frac{2}{Z_T(C_1 + C_2)} \approx -2 \frac{\omega_i}{A_V}.$$
(7.15)



The above analysis agrees well with simulation results.

While frequency response is an important requirement in an RF amplifier, a good noise performance is equally significant since it places a limit on the smallest RF signal that can be detected. Noise figure (NF) is commonly used as a figure of merit in low-noise amplifiers (LNA). It is shown in Section 7.4 that this bandpass amplifier has better noise performance than that of the corresponding low-pass amplifier since the source impedance Z_s , as defined in Fig. 4 has an inductive reactance component which is closer to the optimum for lowest noise figure. The simulated noise figure has a minimum of 6.4 dB at the frequency 1.5 GHz, of which 0.5 dB is contributed by transistor Q_5 and resistive loss in L_1 . For purposes of comparison, the untuned circuit has a -3 -dB frequency of 1.2 GHz and a noise figure of greater than 7 dB at the frequency 1.5 GHz.



7.4. Noise Figure Derivation

Noise figure is defined as the ratio of the total output noise power to the output noise power contributed by the source resistance. Because of the influence of the source resistance on the noise figure, an LNA often incorporates an impedance-matching network (ideally noiseless) at the input in order to obtain an optimum source resistance for noise performance. In the following paragraphs, a general expression

for the noise figure is derived and then used to predict the noise performance of the amplifier in Fig. 7.4.

Let Z_s denote the source impedance, $\overline{v_s^2}$ denote the noise power of the source resistance, and represent the noise performance of the amplifier by equivalent input noise voltage and current generators $\overline{v_i^2}$ and $\overline{i_i^2}$. After the noise voltage v_i (*rms value*) is decomposed into

$$v_i = v_u + i_i Z_c \quad (7.16)$$

where with respect to the noise current i_i , v_u is an uncorrelated part and Z_c is a correlation factor [Har76], the noise figure can be shown to be

$$\text{NF} = 1 + \frac{\overline{v_u^2}}{\overline{v_s^2}} + \frac{\overline{i_i^2}}{\overline{v_s^2}} |Z_c + Z_s|^2. \quad (7.17)$$

Now assume

$$Z_c = R_c + jX_c \quad (7.18)$$

$$Z_s = R_s + jX_s \quad (7.19)$$

$$\overline{v_u^2} = 4kTR_u \Delta f \quad (7.20)$$

$$\overline{i_i^2} = 4kTG_i \Delta f \quad (7.21)$$

$$\overline{v_s^2} = 4kTR_s \Delta f. \quad (7.22)$$

Substituting (7.18-7.22) into (7.17) yields

$$\text{NF} = 1 + \frac{R_u}{R_s} + \frac{G_i}{R_s} \left[(R_c + R_s)^2 + (X_c + X_s)^2 \right]. \quad (7.23)$$

By taking the partial derivatives of (7.23) with respect to X_s and R_s , and setting them equal to zero we find that the noise figure is optimum if

$$X_s(\text{opt}) = -X_c \quad \text{and} \quad R_s(\text{opt}) = \sqrt{\frac{R_u}{G_i} + R_c^2}. \quad (7.24)$$

The above result is now applied to the circuit in Fig. 7.4. The amplifier noise is assumed to be dominated by noise in the input transistor Q_1 and feedback resistors R_F and R_E . Figure 7.9(a) shows the simplified input stage for noise analysis. In this figure, $\overline{v_{ia}^2}$ and $\overline{i_{ia}^2}$ are the equivalent noise generators for the bipolar transistor Q_1 . Quantities $\overline{i_f^2}$ and $\overline{v_e^2}$ are the associated thermal-noise generators for the feedback elements. In Fig. 7.7(b), all the noise sources in the circuit are replaced by two equivalent noise

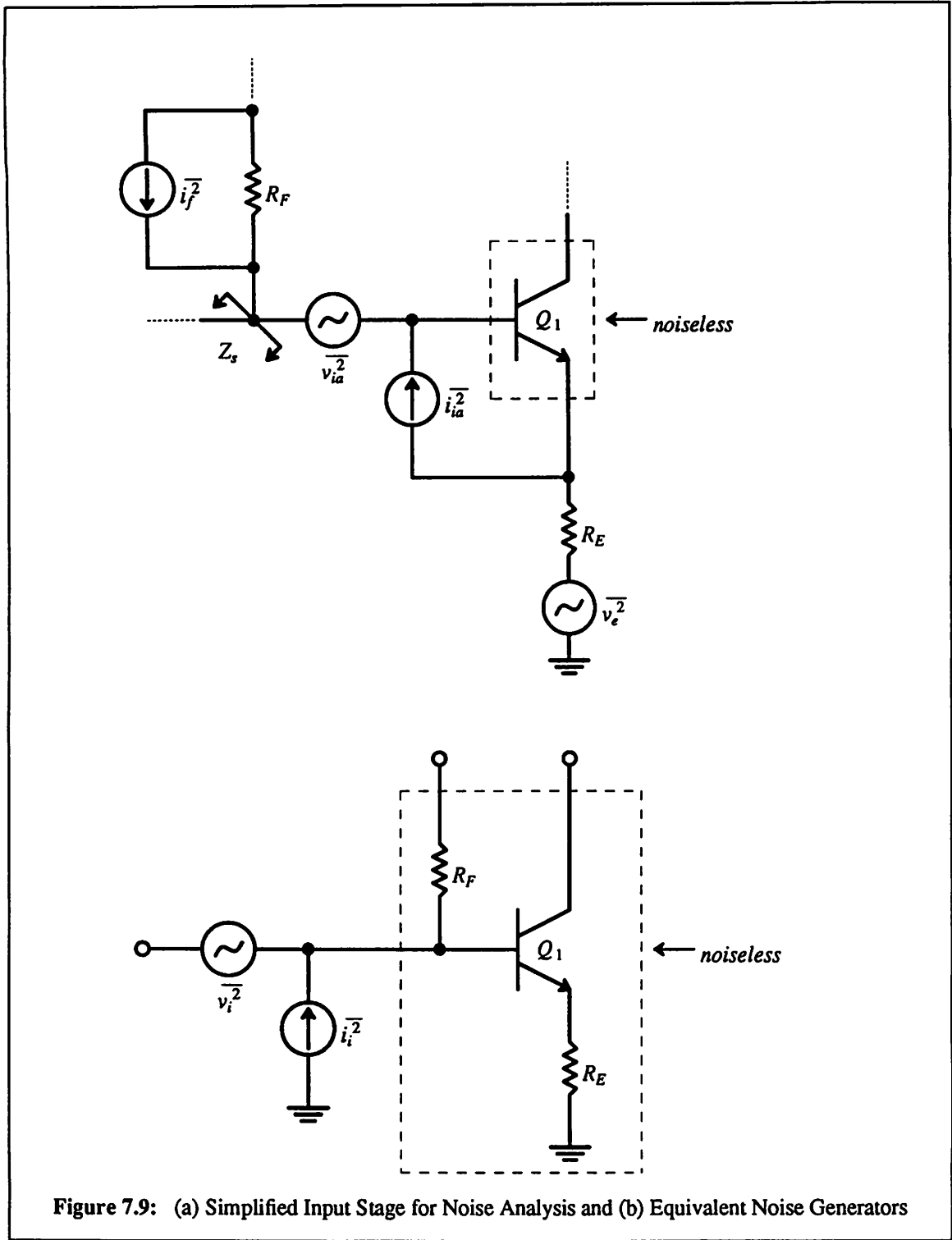


Figure 7.9: (a) Simplified Input Stage for Noise Analysis and (b) Equivalent Noise Generators

generators $\overline{v_i^2}$ and $\overline{i_i^2}$. The equivalent noise generators for the bipolar transistor are [Gra84]

$$\overline{v_{ia}^2} = \overline{v_b^2} + r_b^2 \overline{i_b^2} + \left| \frac{1}{g_m} + \frac{r_b}{\beta(\omega)} \right|^2 \overline{i_c^2} \quad (7.25)$$

$$\overline{i_{ia}^2} = \overline{i_b^2} + \left| \frac{1}{\beta(\omega)} \right|^2 \overline{i_c^2}. \quad (7.26)$$

In (7.25) and (7.26), quantities $\overline{v_b^2}$, $\overline{i_b^2}$, and $\overline{i_c^2}$ are the noise generators of the base resistor, base current, and collector current, respectively. They are expressed in terms of the *mean-square values*

$$\begin{aligned} \overline{v_b^2} &= 4kTr_b \Delta f \\ \overline{i_b^2} &= 2qI_B \Delta f + K \frac{I_B^a}{f} \Delta f \\ \overline{i_c^2} &= 2qI_C \Delta f = 4kT \frac{g_m}{2} \Delta f. \end{aligned}$$

Taking into account the thermal noise generated by feedback elements R_F and R_E , we can show that the overall equivalent noise generators are (*rms values*)

$$v_i = v_b + r_b i_b + \left[\frac{1}{g_m} + \frac{r_b + R_E}{\beta(\omega)} \right] i_c + v_e \quad (7.27)$$

$$i_i \approx i_b + \frac{i_c}{\beta(\omega)} + i_f \quad (7.28)$$

where $\overline{i_f^2} = 4kT \frac{1}{R_F} \Delta f$ and $\overline{v_e^2} = 4kTR_E \Delta f$.

The correlation factor Z_c as defined in (7.16) can be determined from the *autocorrelation function* of v_i and i_i [Lee88]

$$E \{ v_i i_i^* \} = E \{ (v_u + i_i Z_c) i_i^* \} = E \{ v_u i_i^* + Z_c |i_i|^2 \}.$$

By assumption, quantities v_u and i_i are uncorrelated and thus

$$Z_c = \frac{E \{ v_i i_i^* \}}{E \{ |i_i|^2 \}} = \frac{E \{ v_i i_i^* \}}{\overline{i_i^2}}. \quad (7.29)$$

If the base shot noise and flicker noise can be neglected due to small dc base current and high-frequency operation, respectively, the correlation factor can be derived to be

$$Z_c = \frac{\left[\frac{1}{g_m} + \frac{r_b + R_E}{\beta(\omega)} \right] \frac{1}{\beta^*(\omega)} \overline{i_c^2}}{\frac{1}{|\beta(\omega)|^2} \overline{i_c^2} + \overline{i_f^2}}. \quad (7.30)$$

Equation (7.30) can be simplified to

$$Z_c = \frac{(r_b + R_E) + \beta(\omega) / g_m}{1 + \alpha} = R_c + j X_c \quad (7.31)$$

where $\alpha \equiv |\beta(\omega)|^2 \frac{2}{g_m R_F}$. Equation (7.16) is now rewritten as

$$v_u = v_i - i_i Z_c. \quad (7.32)$$

Substituting (7.27), (7.28), and (7.31) into (7.32) gives

$$v_u = [v_b + v_e] + \left\{ \frac{1}{g_m} + \frac{r_b + R_E}{\beta(\omega)} \right\} \left[\frac{\alpha}{1 + \alpha} \right] i_c - \left\{ r_b + R_E + \frac{\beta(\omega)}{g_m} \right\} \left[\frac{1}{1 + \alpha} \right] i_f. \quad (7.33)$$

The mean-square value $\overline{v_u^2}$ can be determined directly from (7.33) where the noise generators v_b , v_e , i_c , and i_f are uncorrelated. Quantity R_u from $\overline{v_u^2} = 4kTR_u \Delta f$ is

$$\begin{aligned} R_u = (r_b + R_E) + \frac{g_m}{2} \left\{ \frac{1}{g_m^2} + \frac{(r_b + R_E)^2}{|\beta(\omega)|^2} \right\} \left[\frac{\alpha}{1 + \alpha} \right]^2 \\ + \frac{1}{R_F} \left\{ (r_b + R_E)^2 + \frac{|\beta(\omega)|^2}{g_m^2} \right\} \left[\frac{1}{1 + \alpha} \right]^2. \end{aligned} \quad (7.34)$$

Quantity G_i from $\overline{i_i^2} = 4kTG_i \Delta f$ is

$$G_i = \frac{1}{|\beta(\omega)|^2} \frac{g_m}{2} + \frac{1}{R_F}. \quad (7.35)$$

Quantities R_c , R_u , and G_i as given in (7.31), (7.34), and (7.35), respectively, can be now substituted in (7.24) for the optimum source resistance.

In the frequency range $\frac{\omega_l}{\beta_o} < \omega < \omega_t$, the current gain $\beta(\omega)$ can be approximated by

$$\beta(\omega) \approx \frac{\omega_t}{j\omega} \approx \frac{g_m}{j\omega C_\pi}. \quad (7.36)$$

Substituting (7.36) into the imaginary component of (7.31) gives

$$X_c = -\frac{1}{\omega C_\pi} \left[1 + \frac{2}{g_m R_F} \left[\frac{\omega_t}{\omega} \right]^2 \right]^{-1}. \quad (7.37)$$

Since $X_s(\text{opt}) = -X_c$, the optimum source reactance is inductive. The optimum source inductance is

$$L_s(\text{opt}) = \frac{1}{\omega^2 C_\pi} \left[1 + \frac{2}{g_m R_F} \left(\frac{\omega_f}{\omega} \right)^2 \right]^{-1} \quad (7.38)$$

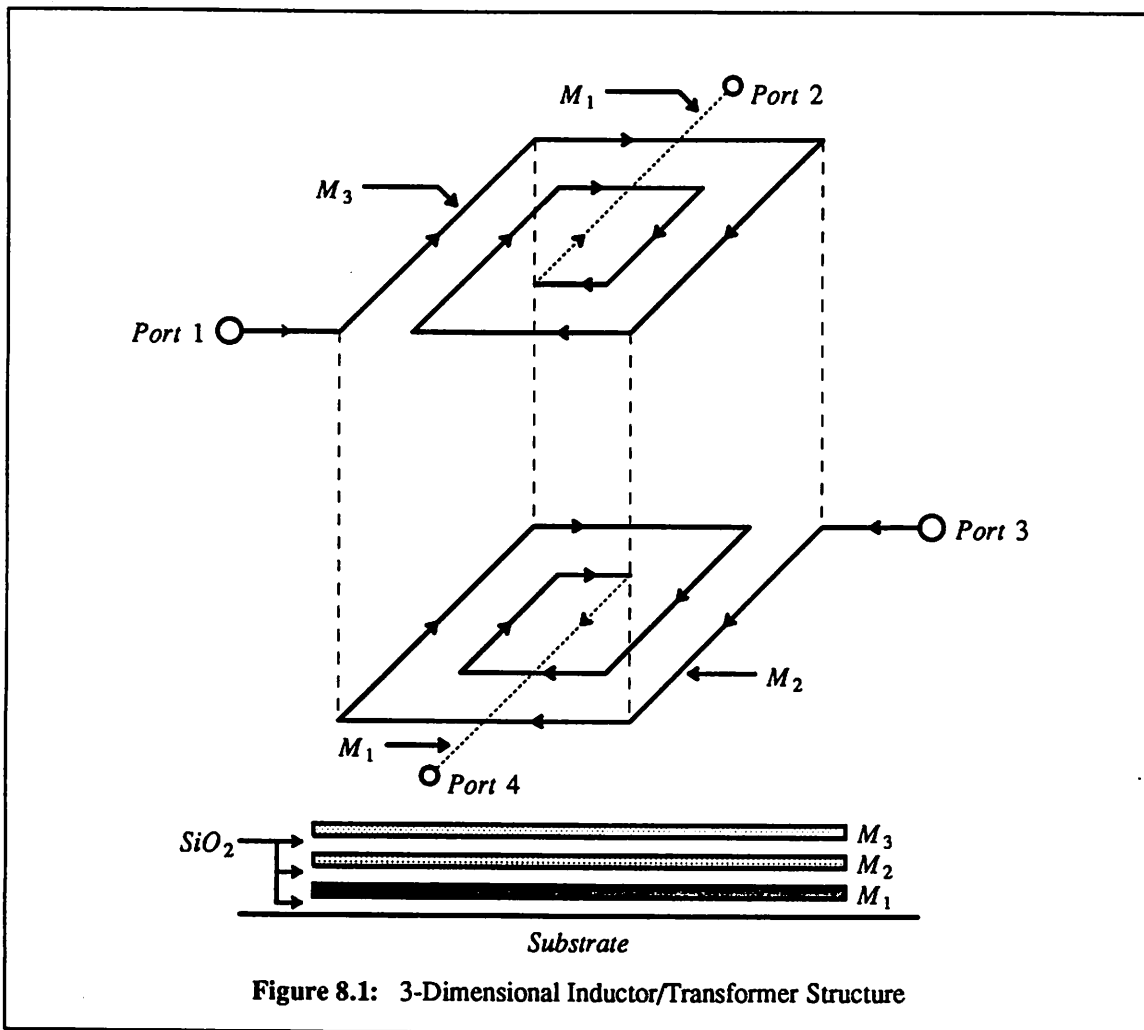
The above analysis predicts that better noise performance can be achieved with the presence of inductor L_1 . While this inductor is used mainly to shift the low-pass response to a bandpass response, it also functions as an inductive source reactance for improving noise performance.

7.5. Conclusion

The application of monolithic inductors in the design of RF bandpass amplifiers has been investigated in this chapter. Inductors can be used to boost circuit gain and to improve impedance matching and noise performance. An L-band RF amplifier has been realized to confirm the theoretical investigation.

Chapter 8 - Conclusions and Future Directions

This thesis has demonstrated the application of Si bipolar IC technology to the design and fabrication of microwave inductors, voltage-controlled oscillators, and amplifiers. The attainable performance with these individual circuits gives much promise and potential for the development of multifunction silicon MMICs (monolithic microwave integrated circuits). Analytical design techniques have been particularly emphasized throughout this dissertation. They provide much insight into the circuit performance and limitations, and have been pivotal in the development of new circuit configurations.



Future research with potential application in MMIC technology may include the characterization of the multispiral inductor/transformer structure shown in Fig. 8.1. Due to the magnetic field strongly cou-

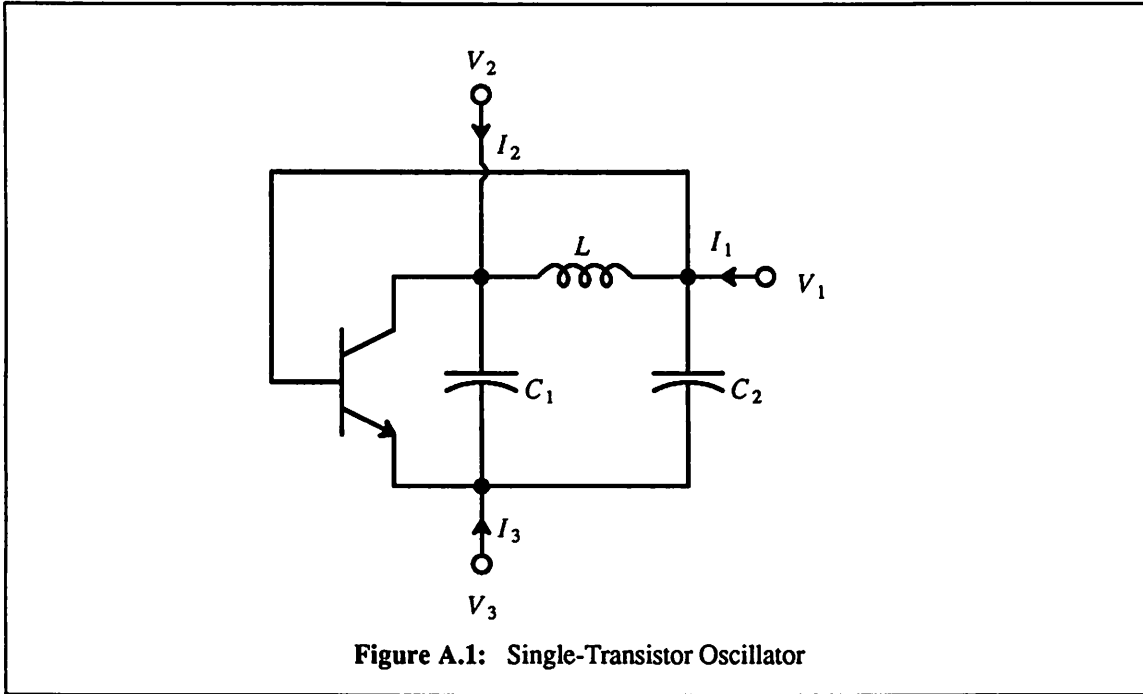
pling between the metal segments, this structure achieves a ratio of inductance per unit area higher than that of a single spiral structure, which in turn implies higher inductor Q . Characterization of this structure is expected to be complicated and may require intensive EM-field theory.

In the equivalent lumped model of the spiral inductor investigated in Chapter 5, the substrate resistor R_p is probably the most difficult element to characterize. Though its value can be derived from the measured S parameters, it is more desirable if the effect of this circuit element is minimized. One way to minimize its effect is to introduce a highly doped n^+ layer underneath the structure. This provides an alternative low-resistive conductive path to the substrate contact.

As frequencies of interest continue to increase, the electric coupling through the lossy Si substrate becomes important and can degrade the circuit performance, especially in Si microwave amplifiers. In an amplifier circuit, the substrate can link the input to the output through the collector-substrate capacitance of the active transistors, and may cause a reduction in circuit bandwidth due to the Miller multiplication effect. It is important, therefore, to understand the substrate structure and to be able to characterize it probably with a 3-D circuit model. Such research could provide explanations for many high-frequency monolithic-amplifier anomalies presently observed in practice.

Appendix A - Indefinite Admittance Matrix

The indefinite admittance matrix is derived for the single-transistor oscillator shown in Fig. A.1. For generality, the bias circuit is not shown and the datum node is not yet specified. The result obtained can be used for analyzing the linear behavior of the Colpitts and Pierce oscillators.



The circuit is redrawn in Fig. A.2 in which the bipolar transistor is represented by a simplified high-frequency model. The indefinite admittance matrix \mathbf{Y} is defined as follows

$$\begin{bmatrix} I_1 \\ I_2 \\ I_3 \end{bmatrix} = \begin{bmatrix} Y_{11} & Y_{12} & Y_{13} \\ Y_{21} & Y_{22} & Y_{23} \\ Y_{31} & Y_{32} & Y_{33} \end{bmatrix} \begin{bmatrix} V_1 \\ V_2 \\ V_3 \end{bmatrix}$$

where

$$Y_{11} = \frac{I_1}{V_1} (V_2 = V_3 = 0) \quad Y_{12} = \frac{I_1}{V_2} (V_1 = V_3 = 0) \quad Y_{13} = \frac{I_1}{V_3} (V_1 = V_2 = 0)$$

$$Y_{21} = \frac{I_2}{V_1} (V_2 = V_3 = 0) \quad Y_{22} = \frac{I_2}{V_2} (V_1 = V_3 = 0) \quad Y_{23} = \frac{I_2}{V_3} (V_1 = V_2 = 0)$$

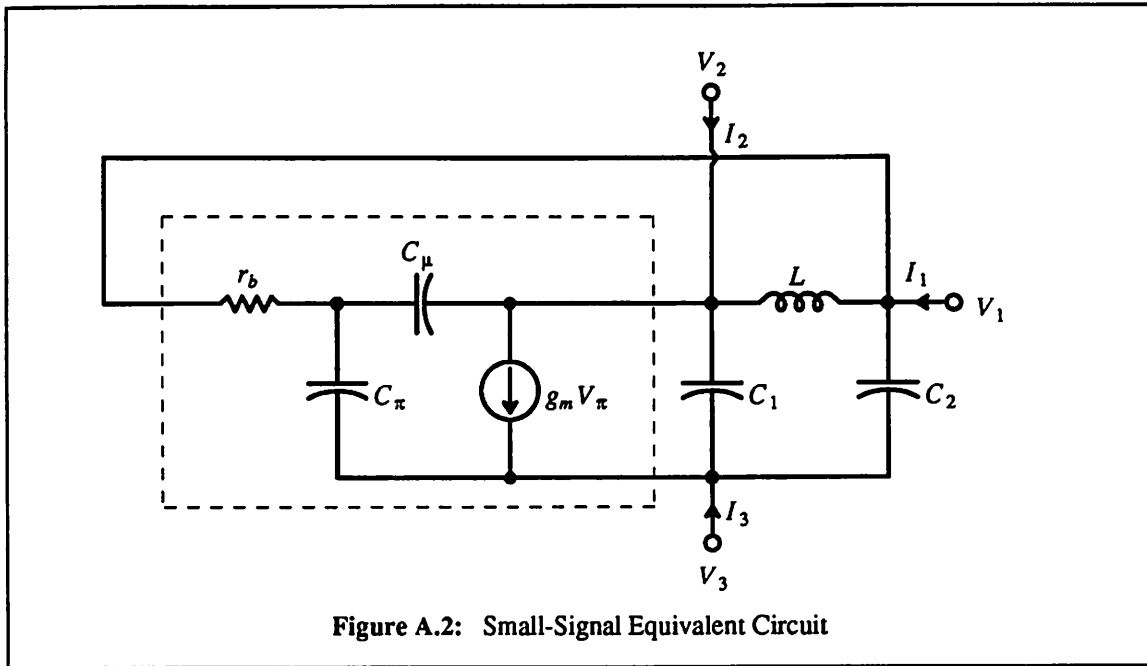


Figure A.2: Small-Signal Equivalent Circuit

$$Y_{31} = \frac{I_3}{V_1} (V_2 = V_3 = 0) \quad Y_{32} = \frac{I_3}{V_2} (V_1 = V_3 = 0) \quad Y_{33} = \frac{I_3}{V_3} (V_1 = V_2 = 0).$$

Any indefinite admittance matrix has a special property that the sum of any row or column in the matrix is equal to zero. The matrix \mathbf{Y} can be derived to be

$$Y_{11} = \frac{1}{sL_1} \left\{ \frac{1 + s(C_\pi + C_\mu)r_b + s^2L_1(C_2 + C_\pi + C_\mu) + s^3L_1C_2(C_\pi + C_\mu)r_b}{1 + s(C_\pi + C_\mu)r_b} \right\}$$

$$Y_{12} = -\frac{1}{sL_1} \left\{ \frac{1 + s(C_\pi + C_\mu)r_b + s^2L_1C_\mu}{1 + s(C_\pi + C_\mu)r_b} \right\}$$

$$Y_{13} = -g_m \left\{ \frac{s(C_2 + C_\pi)/g_m + s^2C_2r_b(C_\pi + C_\mu)/g_m}{1 + s(C_\pi + C_\mu)r_b} \right\}$$

$$Y_{21} = -\frac{1}{sL_1} \left\{ \frac{1 + s[(C_\pi + C_\mu)r_b - L_1g_m] + s^2L_1C_\mu}{1 + s(C_\pi + C_\mu)r_b} \right\}$$

$$Y_{22} = \frac{1}{sL_1} \left\{ \frac{1 + s(C_\pi + C_\mu)r_b + s^2L_1(C_1 + C_\mu + C_\mu r_b g_m) + s^3L_1C_1(C_\pi + C_\mu + C_\pi C_\mu / C_1)r_b}{1 + s(C_\pi + C_\mu)r_b} \right\}$$

$$Y_{23} = -g_m \left\{ \frac{1 + s(C_1/g_m + C_\mu r_b) + s^2C_1r_b(C_\pi + C_\mu + C_\pi C_\mu / C_1)/g_m}{1 + s(C_\pi + C_\mu)r_b} \right\}$$

$$Y_{31} = -g_m \left\{ \frac{1 + s(C_2 + C_\pi) / g_m + s^2 C_2 r_b (C_\pi + C_\mu) / g_m}{1 + s(C_\pi + C_\mu) r_b} \right\}$$

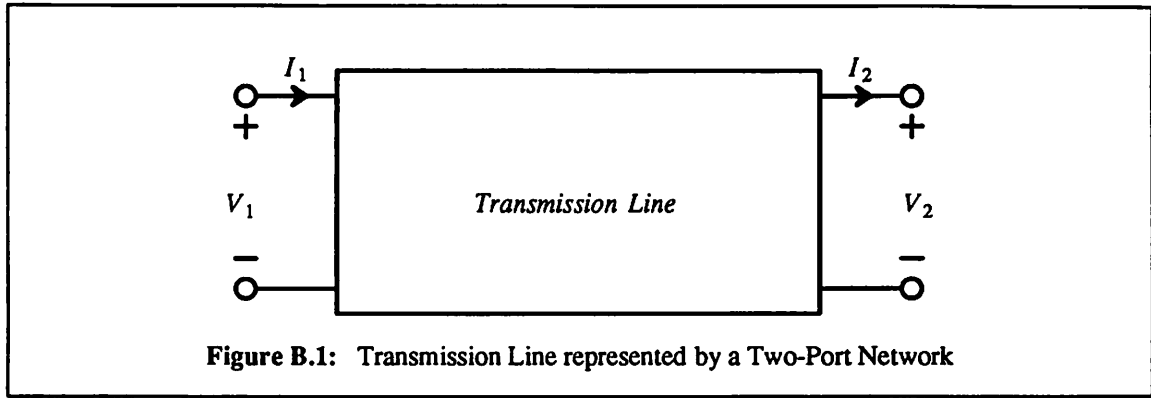
$$Y_{32} = -g_m \left\{ \frac{s(C_1 / g_m + C_\mu r_b) + s^2 C_1 r_b (C_\pi + C_\mu + C_\pi C_\mu / C_1) / g_m}{1 + s(C_\pi + C_\mu) r_b} \right\}$$

$$Y_{33} = g_m \left\{ \frac{1 + s[(C_1 + C_2 + C_\pi) / g_m + C_\mu r_b] + s^2[(C_1 + C_2) r_b (C_\pi + C_\mu) / g_m + C_\pi r_b C_\mu / g_m]}{1 + s(C_\pi + C_\mu) r_b} \right\}$$

Appendix B - Lossless Transmission Line Modeling

In this appendix we derive a simple lumped model for a lossless transmission line. This model can be used to predict the excess phase due to interconnection lines in microwave integrated circuits.

From transmission-line theory, the two-port network representing a transmission line in Fig. B.1 has the following *transmission matrix* [Lee88]



$$\begin{bmatrix} V_1 \\ I_1 \end{bmatrix} = \begin{bmatrix} \cosh(\gamma l) & Z_o \sinh(\gamma l) \\ \frac{1}{Z_o} \sinh(\gamma l) & \cosh(\gamma l) \end{bmatrix} \begin{bmatrix} V_2 \\ I_2 \end{bmatrix}. \quad (\text{B.1})$$

In (B.1), $\gamma = \alpha + j\beta$ is the propagation constant, α and β are the attenuation constant and phase constant, respectively. If the transmission line is lossless ($\alpha = 0$), the transmission matrix (B.1) can be simplified to

$$\begin{bmatrix} V_1 \\ I_1 \end{bmatrix} = \begin{bmatrix} \cos(\beta l) & jZ_o \sin(\beta l) \\ j\frac{1}{Z_o} \sin(\beta l) & \cos(\beta l) \end{bmatrix} \begin{bmatrix} V_2 \\ I_2 \end{bmatrix}. \quad (\text{B.2})$$

If port 2 is terminated by a load impedance Z_L , the input impedance $\frac{V_1}{I_1}$ is

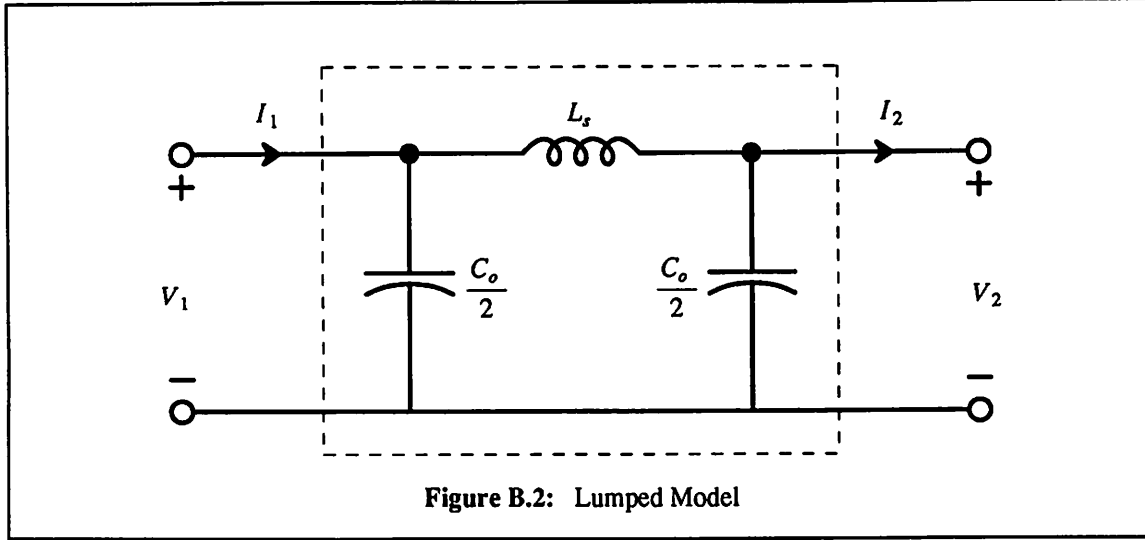
$$Z_i = Z_o \frac{Z_L + jZ_o \tan(\beta l)}{Z_o + jZ_L \tan(\beta l)}. \quad (\text{B.3})$$

If $Z_L = 0$ (shorted transmission line), the input impedance is purely inductive

$$Z_i = jZ_o \tan(\beta l) \Leftrightarrow L_s \equiv \frac{Z_o}{\omega} \tan(\beta l). \quad (\text{B.4})$$

If $Z_L = \infty$ (open-circuited transmission line), the input impedance is purely conductive

$$Z_i = \frac{Z_o}{j \tan(\beta l)} \Leftrightarrow C_o \equiv \frac{1}{Z_o \omega} \tan(\beta l). \quad (\text{B.5})$$



In the following paragraphs we show that the circuit in Fig. B.2 is adequate for modeling a lossless transmission line provided that quantity βl is much less than 1. The transmission matrix for the circuit of Fig. B.2 can be derived to be

$$\begin{bmatrix} V_1 \\ I_1 \end{bmatrix} = \begin{bmatrix} \left[1 + s^2 \frac{L_s C_o}{2} \right] & sL_s \\ sC_o \left[1 + s^2 \frac{L_s C_o}{4} \right] & \left[1 + s^2 \frac{L_s C_o}{2} \right] \end{bmatrix} \begin{bmatrix} V_2 \\ I_2 \end{bmatrix}. \quad (\text{B.6})$$

Substituting $s = j\omega$, $L_s = \frac{Z_o}{\omega} \tan(\beta l)$, and $C_o = \frac{1}{Z_o \omega} \tan(\beta l)$ into (B.6) yields

$$\begin{bmatrix} V_1 \\ I_1 \end{bmatrix} = \begin{bmatrix} 1 - \frac{1}{2} \tan^2(\beta l) & jZ_o \tan(\beta l) \\ j\frac{1}{Z_o} \tan(\beta l) \left[1 - \frac{1}{4} \tan^2(\beta l) \right] & 1 - \frac{1}{2} \tan^2(\beta l) \end{bmatrix} \begin{bmatrix} V_2 \\ I_2 \end{bmatrix}. \quad (\text{B.7})$$

If $\beta l (= \frac{2\pi}{\lambda} l)$ is much less than 1 or equivalently, the length l of the transmission line is much less

than the quarter wavelength $\frac{\lambda}{4}$

$$\tan(\beta l) \approx (\beta l) \quad (\text{B.8})$$

$$\cos(\beta l) \approx 1 - \frac{1}{2}(\beta l)^2 \quad (\text{B.9})$$

$$\sin(\beta l) \approx (\beta l). \quad (\text{B.10})$$

Using (B.8) in (B.7) gives

$$\begin{bmatrix} V_1 \\ I_1 \end{bmatrix} \approx \begin{bmatrix} 1 - \frac{1}{2}(\beta l)^2 & jZ_o(\beta l) \\ j\frac{\beta l}{Z_o} \left[1 - \frac{1}{4}(\beta l)^2 \right] & 1 - \frac{1}{2}(\beta l)^2 \end{bmatrix} \begin{bmatrix} V_2 \\ I_2 \end{bmatrix}. \quad (\text{B.11})$$

Substituting (B.9) and (B.10) into (B.2) gives

$$\begin{bmatrix} V_1 \\ I_1 \end{bmatrix} \approx \begin{bmatrix} 1 - \frac{1}{2}(\beta l)^2 & jZ_o(\beta l) \\ j\frac{\beta l}{Z_o} & 1 - \frac{1}{2}(\beta l)^2 \end{bmatrix} \begin{bmatrix} V_2 \\ I_2 \end{bmatrix}. \quad (\text{B.12})$$

From a comparison between (B.11) [lumped model] and (B.12) [transmission-line theory] we observe that if $\beta l \ll 1$, the lumped model of Fig. B.2 is adequate for modeling a lossless transmission line.

Appendix C - Software Characterization of the Spiral Inductor & Microstrip Line

C.1. Spiral Inductor

```
/*
 * Using the Grover method, this program predicts the inductance value of a silicon integrated planar
 * spiral-inductor. The program also predicts the resistive loss and shunting capacitance of the structure.
 *
 * References:
 * (1) Inductance Calculation, F. Grover, 1942.
 * (2) "Design of Planar Rectangular Microelectronics Inductors," H. Greenhouse, June 1974.
 *
 * Usage: spiral [-c -v -a -d -x] [-i <data>] [-o <output>]
 *
 * Options:
 * -c : keep outermost area constant, step down the turn number
 * -v : step down both the area and turn number
 * -a : consider the air-bridge segment
 * -d : print track distance & segment length
 * -x : xy coordinates for layout
 * -i : data file
 * -o : output file
 *
 * Input Data:
 * L1 : length of the outermost segment #1
 * L2 : length of the outermost segment #2
 * W : metal width
 * S : metal spacing
 * T : metal thickness
 * N : turn number
 *
 * Assumptions:
 * (1) Dielectric and metal are non-magnetic materials. Inductance value is hence
 * independent of the current.
 * (2) Neglect "skin effect", current is uniformly distributed. At low frequencies,
 * skin depth is significantly larger than the conductor thickness.
 * (3) Lumped model: good assumption up to the self-resonant frequency of the
 * spiral inductor.
 */
#include <stdio.h>
#define PI 3.14159
#define EPSILON 8.854e-14 /* F/cm */
#define RshM1 50e-3 /* sheet resistance, M1 */
#define RshM2 20e-3 /* sheet resistance, M2 */
#define CM1 0.029e-15 /* F/um^2, M1 to SUB */
#define CM2 0.016e-15 /* F/um^2, M2 to SUB */
#define TOX 1.7e-6 /* M2 to SUB */
#define LAMBDA 4

FILE *ifp, *ofp;
int constant=0, vary=0, air=0, verbose=0, coord=0;
```

```

double    L1, L2, W, S, T, n, Segment[100];

main(argc, argv)
int  argc;
char *argv[];
{
    int    ifind=0, ofind=0, argn=1, already_print=0;
    double Lself, Mplus, Mminus, Lt;
    double L, Length, Loss, M2Scap;
    double log(), exp(), pow(), sqrt();
    double Abs(), Q(), GMD();

    /* Open user-defined input and output files */
    while (argn < argc) {
        if (strcmp(argv[argn], "-c") == 0) constant=1;
        else if (strcmp(argv[argn], "-v") == 0) vary=1;
        else if (strcmp(argv[argn], "-a") == 0) air=1;
        else if (strcmp(argv[argn], "-d") == 0) verbose=1;
        else if (strcmp(argv[argn], "-x") == 0) coord=1;
        else if (strcmp(argv[argn], "-i") == 0) {
            ifp = fopen(argv[++argn], "r");
            ifind = 1;
        }
        else if (strcmp(argv[argn], "-o") == 0) {
            ofp = fopen(argv[++argn], "w");
            ofind = 1;
        }
        argn++;
    }

    /* Open default input and output files */
    if (ifind==0) ifp = stdin;
    if (ofind==0) ofp = stdout;

    /* Get information about the spiral structure */
    fscanf(ifp, "%f", &L1);
    fscanf(ifp, "%f", &L2);
    fscanf(ifp, "%f", &W);
    fscanf(ifp, "%f", &S);
    fscanf(ifp, "%f", &T);
    fscanf(ifp, "%f", &n);

    fprintf(ofp, "Input Data\n");
    fprintf(ofp, "L1      = %5.1f (uM)\n", L1);
    fprintf(ofp, "L2      = %5.1f (uM)\n", L2);
    fprintf(ofp, " W      = %5.1f (uM)\n", W);
    fprintf(ofp, " S      = %5.1f (uM)\n", S);
    fprintf(ofp, " T      = %5.1f (uM)\n", T);
    fprintf(ofp, " N      = %5.1f, %3.1f (max)\n", n, (L1-W)/(2.0*(W+S)+1));

    /* Determine xy coordinates for the layout of the spiral inductor */
    if (coord) print_xy();
}

```

```

/* Convert input data from micrometer to centimeter */
L1=(L1-W)*1e-4;
L2=(L2-W)*1e-4;
W=W*1e-4;
S=S*1e-4;
T=T*1e-4;

/* Check for valid structure */
if ((L1-(n-1)*(W+S)) <= (L1/2.0)) {
    printf(" *** Structure violated with %3.1f complete turns ***\n", n);
    exit(-1);
}

/* Start computation */
if ((constant) || (vary)) {
    /* determine the maximum turn for the given outermost length */
    n=(int) (L1/(2.0*(W+S))+1.0);
}
else if (air) {
    /* add air-bridge segment */
    n=n+(1.0/4.0);
}

do {
    segment();
    self(&Lself);
    pos_mutual(&Mplus);
    neg_mutual(&Mminus);
    res_loss(&Length, &Loss);
    sht_cap(Length, &M2Scap);

    Lt=Lself+Mplus-Mminus;

    if (!already_print) {
        heading();
        already_print=1;
    }
    fprintf(ofp, "%7.4f %7.4f %7.4f %5.1f %5.1f %4.2f %7.4f %6.1f %5.2f %6.3f\n",
        Lself, 2*Mplus, 2*Mminus, (L1+W)*1e4, (L2+W)*1e4, n, Lt, Length*1e4, Loss, M2Scap*1e12);

    /* Keep outermost area constant but step down the turn number */
    if (constant) n--;

    /* Step down both the area and the turn number */
    if (vary) {
        n--;
        L1=L1-2.0*(W+S);
        L2=L2-2.0*(W+S);
    }
}
while ((n>0.0 && vary) || ((n>0.0) && constant));

fclose(ofp);

```

```

}

/*
 * This procedure prints the output heading.
 */
heading()
{
    fprintf(ofp, "\nSelf-Ind Pos-Ind Neg-Ind L1 L2 Turn Eff-Ind Length Loss Cap\n");
    fprintf(ofp, " (nH) (nH) (nH) (uM) (uM) (nH) (uM) (Ohm) (pF)\n");
}

/*
 * This procedure determines the segment lengths in the spiral inductor.
 */
segment()
{
    int i, y;

    Segment[1]=L1;
    Segment[2]=L2;
    for (i=3; i<=(4*n); i++) {
        if (((i+1)%2)==0) {
            /* odd-numbered segments */
            if ((air) && (i==4*n)) Segment[i]=L1-((int)n-1)*(W+S)+(W+S);
            else {
                y=(i+1)/2;
                Segment[i]=L1-(y-2)*(W+S);
            }
        }
        else {
            /* even-numbered segments */
            y=i/2;
            Segment[i]=L2-(y-1)*(W+S);
        }
    }

    if (verbose) {
        printf("\nSegment Lengths (uM)\n");
        for (i=1; i<=(4*n); i++) {
            printf(" s[%2d] = %5.1f\n", i, Segment[i]*1e4);
        }
    }
}

/*
 * This function returns the absolute value.
 */
double Abs(value)
double value;

```

```

{
  if (value < 0.0) value=(-value);
  return (value);
}

/*
 * This function determines the geometric mean distance between two segments.
 */
double GMD(d, W)
double d, W;
{
  double gmd, r;

  r=d/W;
  gmd=log(d);
  gmd=gmd-1.0/(12.0*pow(r,2.0));
  gmd=gmd-1.0/(60.0*pow(r,4.0));
  gmd=gmd-1.0/(168.0*pow(r,6.0));
  gmd=gmd-1.0/(360.0*pow(r,8.0));
  gmd=gmd-1.0/(660.0*pow(r,10.0));
  gmd=exp(gmd);

  return(gmd);
}

/*
 * This function determines the mutual-inductance parameter Q.
 */
double Q(Length, gmd)
double Length, gmd;
{
  double q;

  if (Length==0.0) q=0.0;
  else {
    q=log((Length/gmd)+sqrt(1.0+pow((Length/gmd),2.0)));
    q=q-sqrt(1.0+pow((gmd/Length),2.0));
    q=q+(gmd/Length);
  }

  return(q);
}

/*
 * This procedure determines the self inductance of the straight-line segments.
 */
self(Lself)
double *Lself;

```

```

{
  int i, count=0;

  *Lself=0.0;
  for (i=1; i<=(4*n); i++) {
    *Lself = *Lself+(2.0*Segment[i])*(log(2.0*Segment[i]/(W+T))+.50049+(W+T)/(3.0*Segment[i]));
    count++;
  }
  if (verbose) printf("\nNumber of Self-Inductance Terms = %5d\n", count);
}

/*
 * This procedure determines the positive mutual inductance between all the
 * parallel segments that have the same current direction.
 *
 * General:      2M = M(l+m-delta) + M(delta) - M(l-delta) - M(m-delta)
 * Special Case: 2M = M(m+p) + M(m+q) - M(p) - M(q)
 */
pos_mutual(Mplus)
double *Mplus;
{
  int i, j, k, count=0;
  double d, p, q, m, Mmp, Mp;
  double l, delta, Mlmd, Md, Mld, Mmd;

  if (verbose) {
    printf("\nDistance between Track Centers (uM)\n");
    for (i=1; i<=(int) ((n-1)*4); i++) {
      j=(int) (4*n-i)/4;
      for (k=1; k<=j; k++) {
        if ((air) && (i+4*k==4*n)) {
          d=k*(W+S);
          delta=Segment[(int) (4*n-2)]+(k-1)*(W+S);
          printf("  d[%2d,%2d] = %5.1f delta = %5.1f\n", i, (int) (4*n), d*1e4, delta*1e4);
        }
        else {
          d=k*(W+S);
          p=q=k*(W+S);
          printf("  d[%2d,%2d] = %5.1f p = %5.1f q = %5.1f\n", i, (i+4*k), d*1e4, p*1e4, q*1e4);
        }
      }
    }
  }

  *Mplus=0.0;
  for (i=1; i<=(int) ((n-1)*4); i++) {
    j=(int) (4*n-i)/4;
    for (k=1; k<=j; k++) {
      if ((air) && (i+4*k==4*n)) {
        d=k*(W+S);
        l=Segment[i];
        m=Segment[(int) (4*n)];

```

```

    delta=Segment[(int) (4*n-2)]+(k-1)*(W+S);
    Mlmd=2.0*(1+m-delta)*Q((1+m-delta),GMD(d,W));
    Md=2.0*delta*Q(delta,GMD(d,W));
    Mld=2.0*Abs(1-delta)*Q(Abs(1-delta),GMD(d,W));
    Mmd=2.0*Abs(m-delta)*Q(Abs(m-delta),GMD(d,W));
    *Mplus = *Mplus+2.0*((Mlmd+Md-Mld-Mmd)/2.0);
    count++;
}
else {
    d=k*(W+S);
    p=k*(W+S);
    m=Segment[i+4*k];
    Mmp=2.0*(m+p)*Q((m+p),GMD(d,W));
    Mp=2.0*p*Q(p,GMD(d,W));
    *Mplus = *Mplus+2.0*(Mmp-Mp);
    count++;
}
}
}
}
if (verbose) printf("\nNumber of Positive Mutual-Inductance Terms = %5d\n", count);
}

/*
 * This procedure determines the negative mutual inductance between all the
 * parallel segments that have the opposite current direction.
 *
 * General:      2M = M(1+m-delta) + M(delta) - M(1-delta) - M(m-delta)
 * Special Case: 2M = M(m+p) + M(m+q) - M(p) - M(q)
 */
neg_mutual(Mminus)
double *Mminus;
{
    int i, j, k, count=0;
    double d, p, q, m, Mmp, Mmq, Mp, Mq;
    double l, delta, Mlmd, Md, Mld, Mmd;

    if (verbose) {
        printf("\nDistance between Track Centers (uM)\n");
        for (i=1; i<=(int) (n*4-2); i++) {
            j=(int) (4*n+2-i)/4;
            for (k=1; k<=j; k++) {
                if ((air) && (i+4*k-2==4*n)) {
                    d=Segment[i+1]-(k-1)*(W+S);
                    delta=Segment[(int) (4*n)]+(k-1)*(W+S);
                    printf(" d[%2d,%2d] = %5.1f delta = %5.1f\n", i, (int) (4*n), d*1e4, delta*1e4);
                }
                else {
                    d=Segment[i+1]-(k-1)*(W+S);
                    p=k*(W+S);
                    q=(k-1)*(W+S);
                    printf(" d[%2d,%2d] = %5.1f p = %5.1f q = %5.1f\n", i, (i+4*k-2), d*1e4, p*1e4, q*1e4);
                }
            }
        }
    }
}

```

```

    }
  }
}

*Mminus=0.0;
for (i=1; i<=(int) (n*4-2); i++) {
  j=(int) (4*n+2-i)/4;
  for (k=1; k<=j; k++) {
    if ((air) && (i+4*k-2==4*n)) {
      d=Segment[i+1]-(k-1)*(W+S);
      l=Segment[(int) (4*n)];
      m=Segment[i];
      delta=Segment[(int) (4*n)]+(k-1)*(W+S);
      Mlmd=2.0*(l+m-delta)*Q((l+m-delta),GMD(d,W));
      Md=2.0*delta*Q(delta,GMD(d,W));
      Mld=2.0*Abs(l-delta)*Q(Abs(l-delta),GMD(d,W));
      Mmd=2.0*Abs(m-delta)*Q(Abs(m-delta),GMD(d,W));
      *Mminus = *Mminus+2.0*((Mlmd+Md-Mld-Mmd)/2.0);
      count++;
    }
    else {
      d=Segment[i+1]-(k-1)*(W+S);
      p=k*(W+S);
      q=(k-1)*(W+S);
      m=Segment[i+4*k-2];
      Mmp=2.0*(m+p)*Q((m+p),GMD(d,W));
      Mmq=2.0*(m+q)*Q((m+q),GMD(d,W));
      Mp=2.0*p*Q(p,GMD(d,W));
      Mq=2.0*q*Q(q,GMD(d,W));
      *Mminus = *Mminus+2.0*((Mmp+Mmq-Mp-Mq)/2.0);
      count++;
    }
  }
}
}
if (verbose) printf("\nNumber of Negative Mutual-Inductance Terms = %5d\n", count);
}

```

```

/*
 * This procedure accumulates the sheet resistance in the segments.
 */
res_loss(Length, Loss)
double *Length, *Loss;
{
  int i;

  *Length=W;
  for (i=1; i<=4*n; i++) *Length = *Length+Segment[i];
  if (air)
    *Loss=(RshM2*(*Length-Segment[i-1])/W)+(RshM1*Segment[i-1]/W);
  else
    *Loss=RshM2*(*Length/W);
}

```

```

/*
 * This procedure determines the parasitic capacitance from the metal segments to the substrate.
 */
sht_cap(Length, M2Scap)
double Length, *M2Scap;
{
    int i=4*n;

    /* Determine cap per unit area using parallel-plate formula */
    *M2Scap=(3.9*EPSILON)/(TOX*1e2); /* F/cm^2 */
    *M2Scap>(*M2Scap)/1e8;          /* F/um^2 */

    /* Consider total area of spiral inductor, appears too large */
    *M2Scap=((L1+W)*(L2+W)*1e8)*CM2;

    /* Consider effective area, seems about right. Also add fringing effects, 25% to 30% of total cap */
    if (air)
        *M2Scap=((Length-Segment[i])*W*1e8)*CM2+(Segment[i]*W*1e8)*CM1;
    else
        *M2Scap=(Length*W*1e8)*CM2;
    *M2Scap>(*M2Scap)*1.25;
}

/*
 * This procedure determines the XY coordinates for the layout of the spiral inductor.
 */
print_xy()
{
    int i, L1s, L2s, Ws, Ss;

    printf("\nSegment (x1,y1) (x2,y2)\n");
    L1s=(int) (L1*LAMBDA);
    L2s=(int) (L2*LAMBDA);
    Ws=(int) (W*LAMBDA);
    Ss=(int) (S*LAMBDA);
    for (i=1; i<=(int) n; i++) {
        if (i==1) printf("%4d (%3d,%3d) ", (i-1)*4+1, 0, L2s-(i-1)*(Ws+Ss));
        else printf("%4d (%3d,%3d) ", (i-1)*4+1, (i-2)*(Ws+Ss), L2s-(i-1)*(Ws+Ss));
        printf("(%3d,%3d)\n", L1s-(i-1)*(Ws+Ss), L2s-i*(Ws+Ss)+Ss);

        printf("%4d (%3d,%3d) ", (i-1)*4+2, L1s-(i-1)*(Ws+Ss), L2s-(i-1)*(Ws+Ss));
        printf("(%3d,%3d)\n", L1s-i*(Ws+Ss)+Ss, (i-1)*(Ws+Ss));

        printf("%4d (%3d,%3d) ", (i-1)*4+3, L1s-(i-1)*(Ws+Ss), (i-1)*(Ws+Ss));
        printf("(%3d,%3d)\n", (i-1)*(Ws+Ss), i*(Ws+Ss)-Ss);

        printf("%4d (%3d,%3d) ", (i-1)*4+4, (i-1)*(Ws+Ss), (i-1)*(Ws+Ss));
        printf("(%3d,%3d)\n", i*(Ws+Ss)-Ss, L2s-i*(Ws+Ss));
    }
}

```

C.2. Microstrip Line

```

/*
 * This program determines the effective characteristic impedance and wavelength of a microstrip line.
 * It also determines the shorted-stub inductance and the open-stub capacitance.
 *
 * References:
 * (1) Microwave Circuit Analysis and Amplifier Design, S. Liao, 1987.
 * (2) "Principles of Microstrip Design", A. Tam, June 1988.
 *
 * Usage: strip [-m1 -m2 -ga] -w <width> -l <length> -f <frequency> [-o <output>]
 *
 * Options:
 * -m1 : microstrip line made of M1 metal
 * -m2 : microstrip line made of M2 metal
 * -ga : microstrip line using GaAs technology
 * -o : output file
 *
 * Input Data:
 * -w : width in micrometer
 * -l : length in micrometer
 * -f : frequency
 */
#include <stdio.h>
#define PI 3.14159
#define Eo 8.854e-12
#define C 3.0e8 /* velocity of light in vacuum, m/s */
#define EOx 3.9 /* relative dielectric constant of oxide */
#define ESi 11.7 /* relative dielectric constant of silicon */
#define EGaAs 13.1 /* relative dielectric constant of GaAs */
#define M1CAP 0.029e-15 /* parasitic cap from M1 to Sub */
#define M2CAP 0.016e-15 /* parasitic cap from M2 to Sub */

FILE *ifp, *ofp;

main (argc, argv)
int argc;
char *argv[];
{
    int ifind, ofind, argn=1, SiM1=0, SiM2=0, GaAs=0;
    double W, Length, Freq, T, H, CpA, Er;
    double Weff, Eeff, Zo, Coeff, Lambda;
    double Leff, Ceff, Sig, Par;
    double abs(), log(), exp(), pow(), sqrt(), tan();

    /* Open user-defined input and output files */
    while (argn < argc) {
        if (strcmp(argv[argn], "-m1") == 0) SiM1=1;
        if (strcmp(argv[argn], "-m2") == 0) SiM2=1;
        if (strcmp(argv[argn], "-ga") == 0) GaAs=1;
        if (strcmp(argv[argn], "-w") == 0)
            sscanf (argv[++argn], "%f", &W);
        if (strcmp(argv[argn], "-l") == 0)

```

```

    sscanf (argv[++argn], "%f", &Length);
    if (strcmp(argv[argn], "-f") == 0)
        sscanf (argv[++argn], "%f", &Freq);
    if (strcmp(argv[argn], "-i") == 0) {
        ifp = fopen(argv[++argn], "r");
        ifind = 1;
    }
    else if (strcmp(argv[argn], "-o") == 0) {
        ofp = fopen(argv[++argn], "w");
        ofind = 1;
    }
    argn++;
}

/* Open default input and output files */
if (ifind==0) ifp = stdin;
if (ofind==0) ofp = stdout;

if (SiM1) {
    T=0.675; H=0.8;
    CpA=M1CAP; Er=EOx;
}
else if (SiM2) {
    T=1.8; H=1.7;
    CpA=M2CAP; Er=EOx;
}
else if (GaAs) {
    T=1.8; H=200.0;
    CpA=0.0; Er=EGaAs;
}

/* Determine the effective width, Eqns. (6-1-8a) & (6-1-8b) */
if ((T/H >= .005) && (W/H >= 1.0/(2.0*PI)))
    Weff=W+(T/PI)*(1.0+log(2.0*H/T));
else if ((T/H >= .005) && (W/H <= 1.0/(2.0*PI)))
    Weff=W+(T/PI)*(1.0+log(4.0*PI*W/T));
else Weff=W;

/* Determine the effective relative dielectric constant, Eqns. (6-1-2) & (6-1-3) */
if (Weff/H <= 1.0)
    Eeff=(Er+1.0)/2.0 + ((Er-1.0)/2.0)*(pow(1.0+12*H/Weff,-0.5)+0.04*pow(1.0-Weff/H,2.0));
else
    Eeff=(Er+1.0)/2.0 + ((Er-1.0)/2.0)*pow(1.0+12*H/Weff,-0.5);

fprintf(ofp, " Input Data\n");
fprintf(ofp, " W      = %5.1f (uM, conductor width)\n", W);
fprintf(ofp, " L      = %5.1f (uM, conductor length)\n", Length);
fprintf(ofp, " T      = %5.1f (uM, conductor thickness)\n", T);
fprintf(ofp, " H      = %5.1f (uM, dielectric thickness)\n", H);
fprintf(ofp, " Er     = %5.1f (relative dielectric constant)\n", Er);
fprintf(ofp, " Weff   = %5.1f (uM, effective conductor width)\n", Weff);
fprintf(ofp, " Eeff   = %5.1f (effective dielectric constant)\n\n", Eeff);

```

```

/* Determine the characteristic impedance, Eqns. (6-1-6) & (6-1-7) */
if (Weff/H <= 1.0)
    Zo=(60.0/sqrt(Eeff))*log(8.0*H/Weff+0.25*Weff/H);
else
    Zo=(120.0*PI/sqrt(Eeff))/(Weff/H + 1.393 + .667*log(Weff/H + 1.444));

/* Determine the wavelength, Eqns. (6-1-4) & (6-1-5) */
if (Weff/H >= 0.6)
    Coeff=(1.0/sqrt(Er))*sqrt(Er/(1.0+0.63*(Er-1.0)*pow(Weff/H,.1255)));
else
    Coeff=(1.0/sqrt(Er))*sqrt(Er/(1.0+0.60*(Er-1.0)*pow(Weff/H,.0297)));
Lambda=Coeff*C/Freq;

/* Convert the conductor length from micrometer to meter */
Length=(Length*1e-6);

/* Shorted-stub inductance */
Leff=(Zo/(2.0*PI*Freq))*tan(2.0*PI*Length/Lambda);

/* Open-stub capacitance */
Ceff=(1.0/(2.0*PI*Freq*Zo))*tan(2.0*PI*Length/Lambda);

/* Parallel parasitic cap calculation. Use the original width in the computation */
Par=(Eeff*Eo)*(W/H)*Length;

/* Signetics parasitic cap calculation */
Sig=1.25*CpA*(Length*1e6)*W;

fprintf(ofp, "Characteristic Impedance = %4.1f\n", Zo);
fprintf(ofp, "Frequency = %7.1e\n", Freq);
fprintf(ofp, "Wave Length = %8.2e\n", Lambda);
fprintf(ofp, "Shorted-stub Inductance = %5.3f (pH)\n", Leff*1e12);
fprintf(ofp, "Open-stub Capacitance = %5.3f (fF)\n", Ceff*1e15);
fprintf(ofp, "Parallel-Plate Cap. = %5.3f (fF)\n", Par*1e15);
fprintf(ofp, "Signetic-Process Cap. = %5.3f (fF)\n", Sig*1e15);
}

```

References

- [Azz66] J. D'Azzo and C. Houpis, *Feedback Control System Analysis and Synthesis*, Chapter 18, McGraw-Hill, New York, 1966.
- [Bah88] I. Bahl and P. Bhartia, *Microwave Solid State Circuit Design*, Wiley Interscience, New York, 1988.
- [Bod45] H. W. Bode, *Network Analysis and Feedback Design*, D. Van Nostrand, New York, 1945.
- [Che68] E. M. Cherry and D. E. Hooper, *Amplifying Devices and Low-Pass Amplifier Design*, Wiley, New York, 1968.
- [Chu87] L. O. Chua, C. A. Desoer, and E. S. Kuh, *Linear and Nonlinear Circuits*, McGraw-Hill, New York, 1987.
- [Cla48] J. K. Clapp, "An Inductance-Capacitance Oscillators of Unusual Frequency Stability," *Proc. IRE*, vol. 36, pp. 356-358, March 1948.
- [Cla54] J. K. Clapp, "Frequency Stable LC Oscillators," *Proc. IRE*, vol. 42, pp. 1295-1300, August 1954.
- [Cla71] K. K. Clarke and D. T. Hess, *Communication Circuits: Analysis and Design*, Chapter 7, Addison Wesley, New York, 1971.
- [Cor75] R. Cordell and W. Garrett, "A Highly Stable VCO for Application in Monolithic Phase-Locked Loops," *IEEE J. Solid-State Circuits*, vol. SC-10, no. 6, pp. 480-485, Dec. 1975.
- [Duc89] T. Ducourant, P. Philippe, P. Dautriche, V. Pauker, C. Villalon, M. Pertus, and J. Damour, "A 3-Chip GaAs Double Conversion TV Tuner System with 70-dB Image Rejection," *1989 IEEE MTT-S Digest*, pp. 95-98.
- [Eds53] W. A. Edson, *Vacuum-Tube Oscillators*, John Wiley & Son, New York, 1953.
- [Eds55] W. A. Edson, "Frequency Memory in Multi-Mode Oscillators," *IRE Trans. on Circuit Theory*, pp. 58-66, March 1955.

- [Elk86] W. El-Kamali, J. Grimm, R. Meierer, and C. Tsironis, "New Design Approach for Wide-Band FET Voltage-Controlled Oscillators," *IEEE Trans. on Microwave Theory and Techniques*, vol. MTT-34, no. 10, pp. 1059-1063, Oct. 1986.
- [For46] J. Ford and N. Korman, "Stability and Frequency Pulling of Loaded Unstabilized Oscillators," *Proc. IRE*, vol. 34, pp. 794-799, Oct. 1946.
- [Fre78] M. E. Frerking, *Crystal Oscillator Design and Temperature Compensation*, Van Nostrand Reinhold, New York, 1978.
- [Fri89] E. Frian, S. Meszaros, M. Cuhaci, and J. Wight, "Computer-Aided Design of Square Spiral Transformers and Inductors," *1989 IEEE MTT-S Digest*, pp. 661-664.
- [Gar79] R. Garg and I. J. Bahl, "Characteristics of Coupled Microstrip Lines," *IEEE Trans. on Microwave Theory and Techniques*, vol. MTT-27, no. 7, pp. 700-705, July 1979.
- [Gib73] G. Gibbons, *Avalanche-Diode Microwave Oscillators*, Clarendon Press, Oxford, 1973.
- [Gon84] G. Gonzalez, *Microwave Transistor Amplifiers - Analysis and Design*, Chapter 5, Prentice-Hall, New Jersey, 1984.
- [Gra84] P. R. Gray and R. G. Meyer, *Analysis and Design of Analog Integrated Circuits*, Chapter 9, Wiley, New York, 1984.
- [Gre74] H. M. Greenhouse, "Design of Planar Rectangular Microelectronic Inductor," *IEEE Trans. on Parts, Hybrids and Packaging*, vol. PHP-10, no. 2, pp. 101-109, June 1974.
- [Gro33] J. Groszkowski, "The Interdependence of Frequency Variation and Harmonic Content, and the Problem of Constant-Frequency Oscillators," *Proc. IRE*, vol. 21, pp. 958-981, July 1933.
- [Gro64] J. Groszkowski, *Frequency of Self-Oscillations*, Macmillan, New York, 1964.
- [Gro46] F. W. Grover, *Inductance Calculations*, Van Nostrand, New Jersey, 1946.
- [Hac65] G. Hachtel, *Semiconductor Integrated Oscillators*, Ph.D. Thesis, University of California, Berkeley, 1965.

- [Har36] R. V. L. Hartley, "Oscillations in Systems with Non-Linear Reactance," *Bell System Technical Journal*, vol. 15, pp. 424-440, 1936.
- [Har76] K. Hartmann, "Noise Characterization of Linear Circuits," *IEEE Trans. on Circuits and Systems*, vol. CAS-23, no. 10, pp. 581-590, Oct. 1976.
- [Kur69] K. Kurokawa, "Some Basic Characteristics of Broadband Negative Resistance Oscillator Circuit," *Bell System Technical Journal*, pp. 1937-1955, July-August 1969.
- [Lee88] E. A. Lee and D. G. Messerschmitt, *Digital Communication*, Chapter 3, Kluwer Academic Publishers, Boston, 1988.
- [Lia87] S. Y. Liao, *Microwave Circuit Analysis and Amplifier Design*, Chapter 6, Prentice-Hall, New Jersey, 1987.
- [Lin61] J. G. Linvill and J. F. Gibbons, *Transistors and Active Circuits*, Chapter 12, McGraw-Hill, New York, 1961.
- [Liu88] T. P. Liu, *High-Frequency, Temperature-Compensated Monolithic Voltage-Controlled Oscillator Design Techniques*, Ph.D. Thesis, UCB/ERL M88/33, University of California, Berkeley, May 1988.
- [Maa86] S. Maas, *Nonlinear Microwave Circuits*, Chapter 12, Artech House, Norwood, 1988.
- [Mat85] T. Matsumoto, L. O. Chua, and M. Komuro, "The Double Scroll," *IEEE Trans. on Circuits and Systems*, vol. CAS-32, no. 8, pp. 798-817, August 1985.
- [McC81] J. L. McCreary, "Matching Properties, and Voltage and Temperature Dependence of MOS Capacitors," *IEEE J. Solid-State Circuits*, vol. SC-16, no. 6, pp. 608-616, Dec. 1981.
- [Mey80] R. G. Meyer and D. Soo, "MOS Crystal Oscillator Design," *IEEE J. Solid-State Circuits*, vol. SC-15, no. 2, pp. 222-228, April 1980.
- [Mey81] R. G. Meyer and R. A. Blauschild, "A 4-terminal Wide-band Monolithic Amplifier," *IEEE J. Solid-State Circuits*, vol. SC-16, pp. 634-638, Dec. 1981.

- [Mey89] R. G. Meyer, *Advanced Integrated Circuits for Communication*, EECS-242 Class Notes, University of California, Berkeley, 1989.
- [Mid75] R. D. Middlebrook, "Measurement of Loop Gain in Feedback System," *International J. of Electronics*, pp. 485-512, April 1975.
- [Mil79] J. Millman, *Microelectronic - Digital and Analog Circuits and Systems*, McGraw-Hill, New York, 1979.
- [Nat87] S. Natarajan, *Theory and Design of Linear Active Networks*, Macmillan, New York, 1987.
- [Ngu90] N. M. Nguyen and R. G. Meyer, "Si IC-Compatible Inductors and LC Passive Filters," *IEEE J. Solid-State Circuits*, vol. SC-25, no. 4, pp. 1028-1031, August 1990.
- [Par84] M. Parisot, Y. Archambault, D. Pavlidis, and J. Magarshack, "Highly Accurate Design of Spiral Inductors for MMICs with Small Size and High Cut-Off Frequency Characteristics," *1984 IEEE MTT-S Digest*, pp. 106-110.
- [Par89] T. S. Parker and L. O. Chua, *Practical Numerical Algorithms for Chaotic Systems*, Chapter 1, Springer-Verlag, New York, 1989.
- [Ped89] D. O. Pederson, *Analog Integrated Circuits for Communication*, EECS-142 Class Notes, 5th Edition, University of California, Berkeley, 1989.
- [Pet83] W. Petersen, A. Gupta, and D. Decker, "A Monolithic GaAs DC to 2-GHz Feedback Amplifier," *IEEE Trans. on Electron Devices*, vol. ED-30, no. 1, pp. 27-29, Jan. 1983.
- [Pet88] E. Pettenpaul, H. Kapusta, A. Weisgerber, H. Mampe, J. Luginsland, and I. Wolff, "CAD Models of Lumped Elements on GaAs up to 18 GHz," *IEEE Trans. on Microwave Theory and Techniques*, vol. MTT-36, no. 2, pp. 294-304, Feb. 1988.
- [Pol34] B. van der Pol, "The Nonlinear Theory of Electric Oscillations," *Proc. IRE*, vol. 22, pp. 1051-1086, 1934.
- [Rob82] W. P. Robins, *Phase Noise in Signal Sources - Theory and Applications*, Peter Peregrinus Ltd., London, 1982.

- [Tam88] A. Tam, "Principles of Microstrip Design," *RF Design*, pp. 29-34, June 1988.
- [Unk82] M. A. Unkrich and R. G. Meyer, "Conditions for Start-Up in Crystal Oscillators," *IEEE J. Solid-State Circuits*, vol. SC-17, no. 1, pp. 87-90, Feb. 1982.
- [War65] R. M. Warner, Jr., and J. N. Fordemwalt, *Integrated Circuits*, McGraw-Hill, p.267, 1965.
- [Zie85] R. E. Ziemer and W. H. Tranter, *Principles of Communications - Systems, Modulation, and Noise*, Chapter 3, Houghton Mifflin, Dallas, 1985.